

ENHANCED LIGHT OUTPUT FROM LUMINESCENT OXIDE NANOPARTICLES:  
SYNTHESIS, CHARACTERIZATION AND SCINTILLATION APPLICATION

By

JIHUN CHOI

A DISSERTATION PRESENTED TO THE GRADUATE SCHOOL  
OF THE UNIVERSITY OF FLORIDA IN PARTIAL FULFILLMENT  
OF THE REQUIREMENTS FOR THE DEGREE OF  
DOCTOR OF PHILOSOPHY

UNIVERSITY OF FLORIDA

2011

© 2011 Jihun Choi

To my wife, my son and my parents

## ACKNOWLEDGMENTS

I would never have been able to finish my dissertation without the guidance of my committee members, help from our group members, and support from my family.

I would like to express my deepest gratitude to my advisor, Dr. Paul H. Holloway, for his excellent guidance, caring, patience, and providing me with an excellent atmosphere for research. His countless passion and endless effort to pursue knowledge always made me refreshed and motivated, and his logical attitude toward science has reinforced my perception about research. I also would like to thank my supervisory committee; Dr. Mark Davidson, Dr. Rolf Hummel, Dr. Jacob Jones and Dr. David Tanner for their advice and support.

I sincerely thank Ludie Harmon for her hospitality and support. I also would like to acknowledge members in our group for all their support and valuable discussion, particularly Jason Rowland, Evan Law, Marc Plaisant, Teng-Kuan Tseng and Kathryn O'Brien. In addition, I want to thank the staff of MAIC and PERC for their assistance, especially Kerry Siebein for her support with TEM analysis and Eric Lambers for his assistance with XPS analysis.

I would also like to thank my parents, parents-in-law and three sisters. Their belief and encouragement with their best wishes could make me endure and complete my work.

Finally, I am thoroughly grateful to my lovely wife, Naree Yoon. She has been always there cheering me up and standing by me through the good and bad times. I deeply thank my son, Nathan for motivating me to complete my long journey. You taught me about responsibility and patience. I love you all.

## TABLE OF CONTENTS

	<u>page</u>
ACKNOWLEDGMENTS.....	4
LIST OF TABLES.....	8
LIST OF FIGURES.....	9
ABSTRACT .....	14
CHAPTER	
1 INTRODUCTION .....	17
2 LITERATURE REVIEW .....	19
2.1 Fundamental of Colloidal Nanoparticles .....	19
2.1.1 Synthesis Process for Colloidal Nanoparticles .....	19
2.1.2 Shape Control of Colloidal Nanoparticles .....	24
2.1.2.1 Shapes of nanoparticles.....	24
2.1.2.2 Growth mechanism of shape-controlled nanoparticles.....	27
2.2 Inorganic Luminescent Materials .....	32
2.2.1 Fundamentals of Luminescent Materials .....	32
2.2.2 Application of Luminescent Materials .....	36
2.3 Scintillation Materials .....	39
2.3.1 Fundamentals of Scintillation Materials .....	40
2.3.2 Application of Scintillation Materials .....	44
2.4 Luminescent Nanoparticles.....	46
2.4.1 Fundamental and Application of Luminescent Nanoparticles .....	46
2.4.2 Surface Modification of Luminescent Nanoparticles.....	49
3 SHAPE CONTROLLED GADOLINIUM OXIDE DOPED WITH EUROPIUM COLLOIDAL NANOCRYSTALS GROWN BY HOT-SOLUTION METHOD .....	52
3.1 Introduction .....	52
3.2 Experimental .....	53
3.2.1 Materials.....	53
3.2.2 Gd <sub>2</sub> O <sub>3</sub> :Eu <sup>3+</sup> Nanocrystal Synthesis.....	53
3.2.3 Characterization .....	54
3.3 Results and Discussion.....	55
3.3.1 Shape Control of Gd <sub>2</sub> O <sub>3</sub> :Eu <sup>3+</sup> Nanocrystals.....	55
3.3.2 Crystal Structure of Gd <sub>2</sub> O <sub>3</sub> :Eu <sup>3+</sup> Nanoparticles.....	58
3.3.3 Photoluminescent Properties of Nanoparticles.....	59
3.3.4 X-ray Luminescence Properties of Nanoparticles.....	63
3.4 Conclusion.....	64

4	ENHANCED PHOTOLUMINESCENCE FROM GADOLINIUM OXIDE DOPED WITH EUROPIUM NANOCORES WITH YTTRIUM OXIDE THIN SHELL.....	65
4.1	Introduction .....	65
4.2	Experimental.....	66
4.2.1	Synthesis of $Gd_2O_3:Eu^{3+}$ Nanocores .....	66
4.2.2	Synthesis of $Y_2O_3$ in the Presence of $Gd_2O_3:Eu^{3+}$ Nanocores.....	66
4.2.3	Characterization of Nanoparticles .....	67
4.3	Results and Discussion.....	68
4.3.1	Crystal Structures and Morphologies of Core and Core/Shell Nanoparticles .....	68
4.3.2	Determination of Shell Thickness by XPS Analysis.....	72
4.3.3	Photoluminescence Properties of Core and Core/Shell Nanoparticles....	74
4.3.4	Luminescence Decay Times of Core and Core/Shell Nanoparticles .....	76
4.4	Conclusion .....	78
5	ENHANCED PHOTOLUMINESCENCE FROM EUROPIUM DOPED GADOLINIUM OXIDE BASED CORE/DUAL-SHELL NANOPARTICLES .....	79
5.1	Introduction .....	79
5.2	Experimental.....	80
5.2.1	Materials.....	80
5.2.2	Synthesis of Silica Cores.....	80
5.2.3	Synthesis of $Gd_2O_3:Eu^{3+}$ Shell on $SiO_2$ Cores.....	80
5.2.4	Synthesis of $Y_2O_3$ Outer Shell on $SiO_2/Gd_2O_3:Eu^{3+}$ Nanoparticles .....	81
5.2.5	Characterization of Nanoparticles .....	81
5.3	Results and Discussion.....	82
5.3.1	Morphology and Crystal Structure of Core/Shell Nanoparticles.....	82
5.3.2	Surface Analysis of Core/Shell Nanoparticles .....	84
5.3.3	Luminescence Properties of Core/Shell Nanoparticles.....	86
5.3.4	Thin Film Quantum Yield Measurement .....	88
5.3.5	Luminescent Decay Time of Core/Shell Nanoparticles.....	89
5.4	Conclusion.....	90
6	X-RAY AND PHOTO-LUMINESCENCE FROM GADOLINIUM SILICATE DOPED WITH CERIUM NANOPARTICLES SYNTHESIZED BY SOLUTION BASED METHODS.....	92
6.1	Introduction .....	92
6.2	Experimental.....	93
6.2.1	Hot Solution Synthesis .....	93
6.2.2	Sol-Gel Synthesis.....	94
6.2.2	Characterization .....	94
6.3	Results and Discussion.....	95
6.3.1	Thermogravimetric Analysis (TGA) of GSO Nanoparticles.....	95
6.3.2	Morphology and Structure of GSO Nanoparticles .....	96
6.3.3	Luminescent Properties of GSO Nanoparticles .....	99

6.3.4 X-ray Luminescence of GSO Nanoparticles .....	102
6.4 Conclusion .....	103
7 CONCLUSIONS .....	105
7.1 Shape Controlled Two Dimensional $Gd_2O_3:Eu^{3+}$ Colloidal Nanocrystals Grown by Hot-Solution Method.....	105
7.2 Enhanced Photoluminescence from $Gd_2O_3:Eu^{3+}$ Nanocores with $Y_2O_3$ Thin Shell.....	105
7.3 Enhanced Photoluminescence from Eu Doped $Gd_2O_3$ Based Core/Dual- Shell Nanoparticles.....	106
7.4 X-RAY and Photo-Luminescence from $Gd_2SiO_5:Ce^{3+}$ Nanoparticles Synthesized by Solution Based Methods.....	106
8 FUTURE WORK .....	108
LIST OF REFERENCES .....	109
BIOGRAPHICAL SKETCH.....	119

## LIST OF TABLES

<u>Table</u>		<u>page</u>
2-1	Crystal structures and morphologies of the as-obtained rare-earth oxides synthesized by thermolysis of $\text{Ln}(\text{BA})_3(\text{H}_2\text{O})_2$ ( $\text{Ln}=\text{La}-\text{Y}$ ) or $\text{Ce}(\text{BA})_4$ in oleic acid (OA)/oleylamine (OM) at 250–330°C for 20–60 min. ....	27
2-2	Applications of luminescent materials classified by different excitation sources. ....	37
2-3	Scintillator requirements in various applications. ....	44
3-1	Experimental parameters of clover, square and round $\text{Gd}_2\text{O}_3:\text{Eu}^{3+}$ nanoparticles (H1-H4). ....	57
3-2	The quantum yield and molar concentration of Eu ions for clover, square and round $\text{Gd}_2\text{O}_3:\text{Eu}^{3+}$ nanoparticles (H1-H4). ....	62
5-1	Quantum yield, radius, volume ratio and weight ratio of $\text{SiO}_2$ , $\text{SiO}_2/\text{Gd}_2\text{O}_3:\text{Eu}^{3+}$ core/single-shell and $\text{SiO}_2/\text{Gd}_2\text{O}_3:\text{Eu}^{3+}/\text{Y}_2\text{O}_3$ core/dual-shell nanoparticles with density of each material. ....	88

## LIST OF FIGURES

<u>Figure</u>	<u>page</u>
2-1 Transmission electron microscopic photographs of Fe <sub>3</sub> O <sub>4</sub> nanoparticles at different preparation temperatures at 303K and 323K.....	20
2-2 Representative TEM micrographs of as-synthesized anatase nanoparticles, obtained at 40 °C.....	21
2-3 Schulman's model of a reverse micelle colloidal particle, as published in 1943. ....	22
2-4 Transmission electron micrograph of CTAB-coated cerium oxide nanoparticles annealed at 200 °C and 500 °C for 2 h. ....	22
2-5 HRTEM images of Gd <sub>2</sub> O <sub>3</sub> :Eu <sup>3+</sup> nanoparticles synthesized from thermal decomposition of Gd(acac) <sub>3</sub> precursor using either HDD or TOPO with a Gd(acac) <sub>3</sub> /surfactant.....	23
2-6 Change in bandgap energy, ΔE <sub>g</sub> , versus d (thickness or diameter) or length/diameter ratio.....	24
2-7 Variation of the relative lattice parameter as the function of the diameters of Pd nanoparticles.....	25
2-8 HRTEM micrographs of CoFe <sub>2</sub> O <sub>4</sub> nanocrystals.....	25
2-9 CdSe nanorods with different sizes and aspect ratios in different concentrations of HPA /TOPO surfactants. ....	27
2-10 Homogeneous nucleation and the free energy change associated with homogeneous nucleation of a sphere of radius r.....	29
2-11 Lamer plot with illustration of nucleation and growth diagram. S=S <sub>c</sub> : critical saturation of monomer concentration to induce nucleation. S=1: equilibrium monomer concentration below which growth stops. ....	29
2-12 A schematic of the nucleation and growth process, in which silver continuously deposits onto the (100) facet to eventually result in a complete octahedron with (111) facet. ....	30
2-13 Monomer-concentration-dependent growth path of CdSe nanocrystal.....	31
2-14 Formation of rare-earth oxide nanopolyhedra, nanoplates, and nanodisks. ....	32

2-15	The excitation curve of $\text{CaYBO}_4:\text{Ce}^{3+}$ monitored at 435 nm and the emission curves of $\text{CaYBO}_4:\text{Ce}^{3+}$ excited at 199 nm (dotted line, marked at curve A) and 295 nm (thin solid line). .....	33
2-16	Emission transitions in a semiconductor. The band gap $E_g$ separates the valence band (VB) and the conduction band (CB). Excitation over the band gap creates electrons in CB and holes in VB.....	35
2-17	Absorption (solid lines) and photoluminescence (dotted lines) spectra of CdS nano-rod. ....	36
2-18	Color diagram of the CIE (CIE=Commission Internationale d'Eclairage) and CIE with Color Temperature Line. ....	37
2-19	Fundamental construction of the fluorescent lamp. ....	38
2-20	Scheme of relaxation of electronic excitations general scheme, and rare-earth containing scintillators. ....	42
2-21	Schematic diagram of a scintillation detector .....	43
2-22	Schematic diagram of positron emission tomography (PET) with the inset illustrating BGO detectors coupled with PMT and a PET scan image of a brain. ....	45
2-23	Pulse-height spectrum of a $^{137}\text{Cs}$ source measured with a $100\text{cm}^2$ area and 2mm depth with LSO crystal coupled with a Hamamatsu R878 PMT.....	46
2-24	Schematic illustration of the density of states in metal and semiconductor clusters. ....	47
2-25	Absorbance properties of II-VI semiconductor nanoparticles.....	48
2-26	Schematic of organic and inorganic passivation.....	49
2-27	The absorption spectra of CdSe/ZnSe nanocrystals during the shell growth. ....	50
2-28	Plot of PL intensity of the $^5\text{D}_0-^7\text{F}_2$ emission at 619 nm versus the $\text{YPO}_4/\text{YVO}_4:\text{Eu}^{3+}$ molar ratio.....	51
3-1	Flow chart of non-hydrolytic hot-solution synthesis procedure. ....	54
3-2	TEM images of $\text{Gd}_2\text{O}_3:\text{Eu}^{3+}$ nanoparticles synthesized with different experimental parameters.....	56
3-3	Modified LaMer plots with an additional axis of reaction temperature. S=Sc: Critical saturation of monomer concentration to induce nucleation. S=1: Equilibrium monomer concentration below which growth stops.....	57

3-4	XRD patterns of as-synthesized samples.....	58
3-5	PL and PLE spectra of $Gd_2O_3:Eu^{3+}$ nanoparticles. The PL spectra of excitation at 250 nm and the PLE spectra for the emission at 609 nm.....	59
3-6	Resolved PL spectra of square nanoparticles with reaction time of 40 min (H2), round nanoparticles with reaction time for 90 min (H3) and for 180 min (H4). .....	60
3-7	X-ray luminescence spectrum of as-prepared sphere-like $Gd_2O_3:Eu^{3+}$ nanocrystals .....	63
4-1	XRD patterns of calcined samples: $Gd_2O_3:Eu^{3+}$ nanocores; $Gd_2O_3:Eu^{3+}/Y_2O_3$ core/shell nanoparticles with the shell grown with a Y to Gd+Eu precursor ratio $R = 1:4$ and $1:1$ and pure $Y_2O_3$ nanoparticles.....	68
4-2	Resolved XRD peak of $Gd_2O_3:Eu^{3+}/Y_2O_3$ core/shell nanoparticles with shell grown with a Y to Gd+Eu precursor ratio $R = 1:1$ .....	69
4-3	TEM images of $Gd_2O_3:Eu^{3+}$ , $Y_2O_3$ and $Gd_2O_3:Eu^{3+}/Y_2O_3$ core/shell nanoparticles: $Gd_2O_3:Eu^{3+}$ core, $Gd_2O_3:Eu^{3+}/Y_2O_3$ ( $R=1:8$ ), $Gd_2O_3:Eu^{3+}/Y_2O_3$ ( $R=1:4$ ), $Gd_2O_3:Eu^{3+}/Y_2O_3$ ( $R=1:1$ ), High resolution of $Gd_2O_3:Eu^{3+}/Y_2O_3$ ( $R=1:1$ ), and $Y_2O_3$ .....	70
4-4	XPS peaks from $Gd_2O_3:Eu^{3+}$ and $Gd_2O_3:Eu^{3+}/Y_2O_3$ core/shell nanoparticles grown with different precursor molar ratios ( $R$ ) and normalized intensity of the Gd $3d_{5/2}$ peak versus $Y_2O_3$ shell thickness. ....	71
4-5	Idealized concentric spherical core/shell structure from which a maximum shell thickness for a given $R$ can be calculated. ....	72
4-6	PL and PLE spectra from $Gd_2O_3:Eu^{3+}$ and $Gd_2O_3:Eu^{3+}/Y_2O_3$ core/shell nanoparticles. The PLE spectra are for emission at 612 nm and the PL spectra are for excitation at 250 nm. The inset shows the uncorrected PL peak intensity versus the value of $R$ . ....	73
4-7	Integrated area of PL peak at 612 nm versus $R$ ; Solid squares are uncorrected data. Solid diamonds are uncorrected normalized data. Open circles are normalized and corrected for the fraction of non-luminescent $Y_2O_3$ based on the value of $R$ . ....	75
4-8	Luminescence decay data for the $Eu^{3+} \ ^5D_0 \rightarrow \ ^7F_2$ transition (612 nm peak). The data are well fit by the solid line which is a single exponential function with a time constant .....	77
5-1	TEM photomicrographs of dual-shell. ....	83

5-2	X-Ray diffraction spectra obtained from pure amorphous silica nanoparticles or calcined $\text{SiO}_2/\text{Gd}_2\text{O}_3:\text{Eu}^{3+}$ core/single-shell nanoparticles and calcined $\text{SiO}_2/\text{Gd}_2\text{O}_3:\text{Eu}^{3+}/\text{Y}_2\text{O}_3$ core/dual-shell nanoparticles.....	84
5-3	X-ray photoelectron peaks from the $\text{SiO}_2$ nanocores (solid line), from $\text{SiO}_2/\text{Gd}_2\text{O}_3:\text{Eu}^{3+}$ core/single-shell (dashed line) and $\text{SiO}_2/\text{Gd}_2\text{O}_3:\text{Eu}^{3+}/\text{Y}_2\text{O}_3$ core/dual-shell nanoparticles (dotted line). .....	85
5-4	The Si 2p XPS peaks from $\text{SiO}_2$ , $\text{SiO}_2/\text{Gd}_2\text{O}_3:\text{Eu}^{3+}$ core/single-shell nanoparticles and normalized intensity of the Si 2p peak versus $\text{Gd}_2\text{O}_3:\text{Eu}^{3+}$ shell thickness. ....	85
5-5	Photoluminescence (PL) and photoluminescence excitation (PLE) spectra from $\text{SiO}_2/\text{Gd}_2\text{O}_3:\text{Eu}^{3+}$ core/single-shell and $\text{SiO}_2/\text{Gd}_2\text{O}_3:\text{Eu}^{3+}/\text{Y}_2\text{O}_3$ core/dual-shell nanoparticles. The PLE spectra are for emission at 612 nm and the PL spectra are for excitation at 250 nm. ....	86
5-6	Model of a spherical core/concentric dual-shell structure from which the weight of nanoparticles necessary for a constant volume of luminescent $\text{Gd}_2\text{O}_3:\text{Eu}^{3+}$ can be determined.....	87
5-7	Schematic diagram of thin film quantum yield (QY) measurement.....	88
5-8	Luminescence decay data for the $\text{Eu}^{3+} \ ^5\text{D}_0 - \ ^7\text{F}_2$ transition (612 nm peak). The data fit very well a single exponential decay (solid line) with a time constant $\tau$ . ....	89
6-1	Flow chart of two-pot hot-solution growth of GSO nanoparticles.....	94
6-2	Thermogravimetric analysis (TGA) data for HSG $\text{Gd}_2\text{SiO}_5:\text{Ce}^{3+}$ 0.5% nanoparticles. Heating rate is $10 \text{ }^\circ\text{Cmin}^{-1}$ . ....	96
6-3	XRD patterns from $\text{Gd}_2\text{SiO}_5:\text{Ce}^{3+}$ nanoparticles compared to the JCDPS pattern for monoclinic $\text{Gd}_2\text{SiO}_5$ (JCPDS # : 40-0282) : $\text{GSO}:\text{Ce}^{3+}$ nanoparticles after calcination at $600 \text{ }^\circ\text{C}$ and $1000 \text{ }^\circ\text{C}$ for 2hr in air. ....	97
6-4	TEM images of $\text{Gd}_2\text{SiO}_5:\text{Ce}^{3+}$ nanoparticles prepared by the sol-gel (SG) method and the hot-solution (HSG) method. ....	98
6-5	PL spectra and intensity for various Ce concentrations showing quenching for $\text{Gd}_2\text{SiO}_5:\text{Ce}^{3+}$ nanoparticles synthesized by the hot-solution method (excitation wavelength = 344 nm). ....	99
6-6	PL and PLE spectra from $\text{Gd}_2\text{SiO}_5:\text{Ce}^{3+}$ nanoparticles calcined at $600 \text{ }^\circ\text{C}$ (dashed line) and $1000 \text{ }^\circ\text{C}$ (solid line).....	100
6-7	Configuration coordinate model energy levels for $\text{Ce}^{3+}$ ions in a $\text{Gd}_2\text{SiO}_5$ host. ....	101

6-8	X-ray luminescence spectrum of calcined $\text{Gd}_2\text{SiO}_5:\text{Ce}^{3+}$ nanoparticles. ....	102
6-9	Differential pulse height spectrum of calcined $\text{GSO}:\text{Ce}^{3+}$ nanoparticles by an $^{241}\text{Am}$ source showing a broad scintillation response centered at approximately channel 300.....	103
8-1	$\text{SiO}_2/\text{Gd}_2\text{O}_3:\text{Eu}^{3+}/\text{Y}_2\text{O}_3/\text{SiO}_2$ core/multi-shell nanoparticles.....	108

Abstract of Dissertation Presented to the Graduate School  
of the University of Florida in Partial Fulfillment of the  
Requirements for the Degree of Doctor of Philosophy

ENHANCED LIGHT OUTPUT FROM LUMINESCENT OXIDE NANOPARTICLES:  
SYNTHESIS, CHARACTERIZATION AND SCINTILLATION APPLICATION

By

Jihun Choi

August 2011

Chair: Paul. H. Holloway  
Cochair: Mark R. Davidson  
Major: Materials Science and Engineering

Scintillator materials have been grown in the past as single crystal phase which generally lead to high cost and small size of radiation detector crystals. In this work, highly efficient scintillator nanoparticles have been synthesized using non-hydrolytic hot-solution growth, sol-gel, and aqueous precipitation methods.

$\text{Gd}_2\text{O}_3:\text{Eu}^{3+}$  nanoparticles with sizes and shapes of 20 nm clovers, 10 nm squares and 15 nm rounds were prepared by a non-hydrolytic high temperature (320 °C) solution growth method. Synthesis parameters such as reaction procedure, time and temperature were varied to investigate their effects on nanocrystal shape and luminescent properties. The variation of nanoparticle shapes was explained by nucleation and growth of oxide nanocrystals. The photoluminescence properties and quantum yields of  $\text{Gd}_2\text{O}_3:\text{Eu}^{3+}$  nanoparticles could be controlled by the synthesis parameters. Round  $\text{Gd}_2\text{O}_3:\text{Eu}^{3+}$  nanoparticles exhibited the highest quantum yield of 67%, whereas clover and square  $\text{Gd}_2\text{O}_3:\text{Eu}^{3+}$  nanoparticles showed lower quantum

yields of 24% and 48%, respectively. The luminescent properties were discussed in terms of doping concentration, host environment and dopant location.

Nanoparticles of  $\text{Gd}_2\text{O}_3:\text{Eu}^{3+}$  ~20 nm in diameter were synthesized at ~180° C using a facile high boiling-point alcohol (polyol) method. The  $\text{Gd}_2\text{O}_3$  nanoparticles, doped with 5 mol% Eu, were crystalline cubic phase and exhibited intense  $^5\text{D}_0$ - $^7\text{F}_2$  photoluminescence (PL) from  $\text{Eu}^{3+}$  after calcination at 600 °C for 2h in air.

Photoluminescence excitation (PLE) data showed that while a small fraction of the emission resulted from direct excitation of  $\text{Eu}^{3+}$ , most of the excitation resulted from adsorption in the Oxygen to Europium charge-transfer band between 225 and 275 nm. Transmission electron microscopy (TEM) images showed that the  $\text{Gd}_2\text{O}_3:\text{Eu}^{3+}$  cores were slightly agglomerated, but the thin  $\text{Y}_2\text{O}_3$  shell could not be detected by TEM. X-ray photoelectron spectroscopy (XPS) was used to detect the thin  $\text{Y}_2\text{O}_3$  shell around the  $\text{Gd}_2\text{O}_3:\text{Eu}^{3+}$  core. Drop-cast thin films of the  $\text{Gd}_2\text{O}_3:\text{Eu}^{3+}/\text{Y}_2\text{O}_3$  core/shell nanoparticles exhibited PL intensities up to 40% larger than from bare core  $\text{Gd}_2\text{O}_3:\text{Eu}^{3+}$  nanoparticles. Increased PL was attributed to reduced non-radiative recombination based on longer luminescence decay times.

Spherical  $\text{SiO}_2$  cores have been coated with oxide dual-shells of  $\text{Gd}_2\text{O}_3:\text{Eu}^{3+}$  and  $\text{Y}_2\text{O}_3$  by a solution precipitation method. Based on transmission electron microscopy (TEM) data, luminescent  $\text{Gd}_2\text{O}_3:\text{Eu}^{3+}$  shells with ~4.5 nm thickness were successfully coated on mono-dispersed  $\text{SiO}_2$  nanocores ~210 ± 15 nm in radius. A continuous  $\text{Y}_2\text{O}_3$  shell ~45 nm thick was then grown on the  $\text{SiO}_2/\text{Gd}_2\text{O}_3:\text{Eu}^{3+}$  nanoparticles. The  $\text{SiO}_2/\text{Gd}_2\text{O}_3:\text{Eu}^{3+}$  core/shell nanoparticles exhibited  $^5\text{D}_0$ - $^7\text{F}_2$  photoluminescence (PL) from  $\text{Eu}^{3+}$  transitions after calcination at 600°C for 2h in air. Photoluminescence

excitation (PLE) data showed that most of the excitation resulted from absorption in the oxygen to europium charge-transfer band between 225 and 275 nm. Drop-cast thin films of core/dual-shell samples exhibited quantum yields (QYs) up to 2 times larger than that of core/single-shell nanoparticles, which was attributed to reduced non-radiative recombination, consistent with longer luminescence decay lifetimes.

Nanophosphor  $\text{Gd}_2\text{SiO}_5:\text{Ce}^{3+}$  (GSO) with sizes between 2 nm - 5 nm was synthesized by sol-gel and hot-solution methods. X-Ray luminescence, photoluminescence (PL) and structural properties of  $\text{GSO}:\text{Ce}^{3+}$  nanoparticles were compared for the two different synthesis methods. PL and X-ray luminescence were both from the  $\text{Ce}^{3+}$  5d-4f transitions at 390~430 °C. The Ce dopant concentration was varied between 0.1% - 10% and concentration quenching was observed at 0.5% under UV excitation. Hot-solution synthesized GSO doped with  $\leq 0.5\%$  Ce exhibited PL after calcination at either 600 °C or 1000 °C for 2 h in air, while  $\text{GSO}:\text{Ce}^{3+}$  nanoparticles prepared by the sol-gel method required calcination at 1000 °C to observe PL.

## CHAPTER 1 INTRODUCTION

“Nano” is one of the most frequently cited words in recent science and engineering fields. Micro and nano fabrication is a representative approach of “top-down” application of the nano-world, which has been led by the Si based electronic devices. The typical example of “bottom-up” technology in the nano-world is a synthesis of nanoparticles, often used as nanocrystals and nanoclusters. Nanoparticles mean nanometer scale particles that are neither small molecules nor bulk solids. In the nanometer scale regime, the physical and chemical properties of materials become unique and novel compared to their bulk counterpart. Among various characteristics of nanoparticles, luminescent properties will be the main focus of my dissertation.

The aim of the work described in this dissertation is to synthesize highly luminescent oxide nanoparticles for scintillation (i.e. luminescence due to energetic particle radiation). To achieve this goal, the following approach was used

1. Synthesize cores and/or core/shell luminescent oxide nanoparticles using solution based synthesis methods.
2. Characterize the structure, morphology, surface, photoluminescence and X-ray luminescence of the oxide nanoparticles.
3. Evaluate the mechanisms to enhance the light output from luminescent oxide nanoparticles.

In the dissertation, Chapter 2 reviews the fundamentals of nanoparticles, their various synthesis methods and applications in different fields. The fundamentals of luminescent materials and several approaches to achieve enhanced luminescence are also reviewed. In Chapter 3, the preparation of shape-controlled gadolinium oxide

doped with europium nanoparticles with a non-hydrolytic synthesis is discussed. The mechanism of nucleation and growth of oxide nanoparticles were also reviewed. In Chapter 4, the synthesis and characterization of gadolinium oxide nanocores doped with europium/yttrium oxide core/shell hetero structures is discussed. Luminescent cores could be passivated by a non-luminescent shell with a facile polyol synthesis method so that enhanced photoluminescence was achieved. In Chapter 5, silica core/dual-shell structures are created and characterized. Silica cores have several advantages such as uniformly spherical shape, ease of synthesis and low cost. Luminescent shell with europium doped gadolinium oxide was grown on silica nanocores. In addition, core/single-shell structures could be coated by yttrium oxide outer shell to passivate non-radiative defects by solution precipitation method. The passivation of surface defects was postulated based on a longer luminescent decay lifetime. Chapter 6 describes the synthesis and characterization of gadolinium silicate (GSO) nanoparticles doped with cerium ions. Single crystals of GSO are used in a scintillation detector. GSO nanoparticles were synthesized by both hot-solution and sol-gel method and their properties were compared. Finally, Conclusions and Future Work are summarized in Chapter 7 and 8.

## CHAPTER 2 LITERATURE REVIEW

### **2.1 Fundamental of Colloidal Nanoparticles**

The development of small size materials is of interests for chemical and material research. The electronic industry with semiconductor devices is a good example of the approach of novel materials, where the size of devices has steadily decreased to the nanometer dimension for the reduction of power consumption and increased computing speed. The counterpart of a micro-fabrication is synthesis of nanoparticles. The synthesis and application of nanoparticles have been intensively studied to understand fundamental phenomena and scientific properties. Nanoparticles exhibit novel properties and functions due to their small size, typically under 100 nm.

#### **2.1.1 Synthesis Process for Colloidal Nanoparticles**

Nanoparticles can be synthesized using at least two different general methods, i.e. “top-down” and “bottom-up” approaches. A top-down method uses physical methods such as milling and micro-fabrication, while a bottom-up method utilizes liquid phase colloidal chemistry. In our study, the bottom-up methods will be used to synthesize nanoparticles due to their advantages in controlling size and shape. Several ‘bottom-up’ synthesis methods will be introduced.

Many of the earliest synthesis of nanoparticles were synthesized by the precipitation method from aqueous solutions followed by thermal decomposition of precursors. For example, Cu, Ag, Pt, Ni, Co and Au nanoparticles were achieved by the precipitation method [1-5]. The precipitation of metals from aqueous or non-aqueous solutions typically requires the reduction of metal cations. Oxide nanoparticles also could be synthesized by the precipitation method. The precipitation of oxide

nanoparticles, from both aqueous and non-aqueous solutions can be broken into two categories, i.e. those that produce modified precursors which must undergo further processing such as calcinations, and those that produce oxide nanoparticles directly. Figure 2-1 shows  $\text{Fe}_3\text{O}_4$  nanoparticles synthesized by a precipitation method at different reaction temperatures [6]. Ferric chloride ( $\text{FeCl}_3$ ) and ferrous chloride ( $\text{FeCl}_2$ ) were used as iron precursors and ammonia was used as a precipitating agent. Without further heat treatment,  $\text{Fe}_3\text{O}_4$  nanoparticles could be synthesized [6].

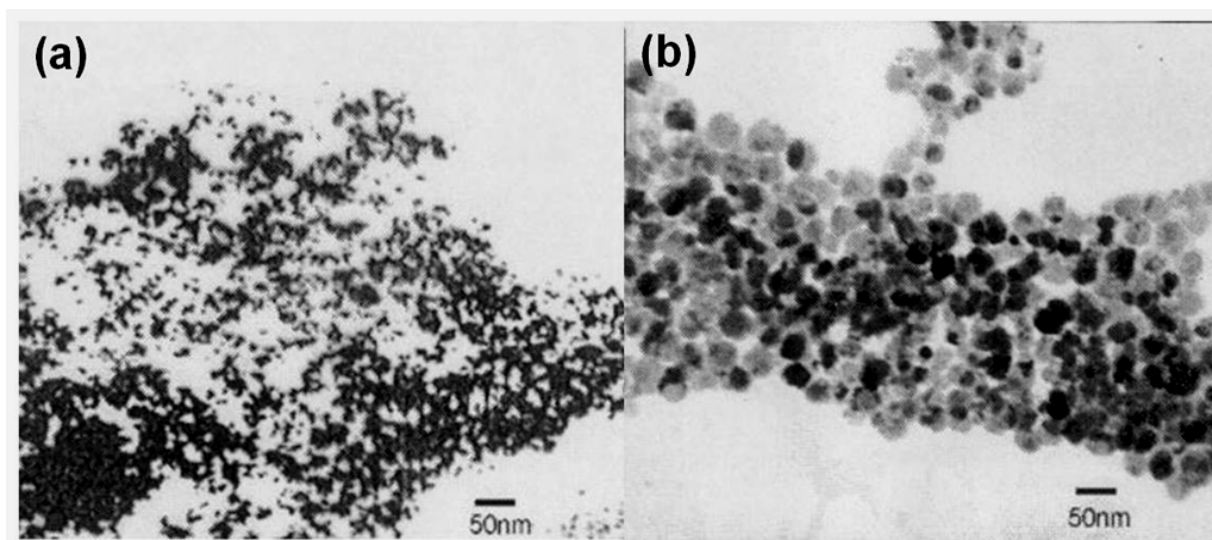


Figure 2-1. Transmission electron microscopic photographs of  $\text{Fe}_3\text{O}_4$  nanoparticles at different preparation temperatures at 303K and 323K.

Typically, sol-gel synthesis refers to the hydrolysis and condensation of alkali-oxide based precursors. In a typical sol-gel synthesis for nanoparticles, the following steps are frequently used [7].

- (1) Formation of stable solutions of precursors (the sol).
- (2) Gelation from the formation of oxide or  $-\text{OH}$  linked network (the gel).
- (3) Drying of the gel, when volatile liquids are removed from the gel network.
- (4) Calcination, stabilizing the gel against rehydration.

It is reported that oxide nanoparticles have been synthesized by a sol-gel method. Titania nanoparticles were easily prepared by controlled hydrolysis and condensation of  $Ti(O^iPr)_4$  (titanium isopropoxide) in an alcohol solution acidified by HCl after drying [8, 9]. A modified sol-gel method proposed by Neiderberger et al. produced nanocrystalline particles without a calcination. The particle size was controlled in the range of 4-8 nm by various temperatures and reactant concentrations, as shown in Figure 2-2 [10].

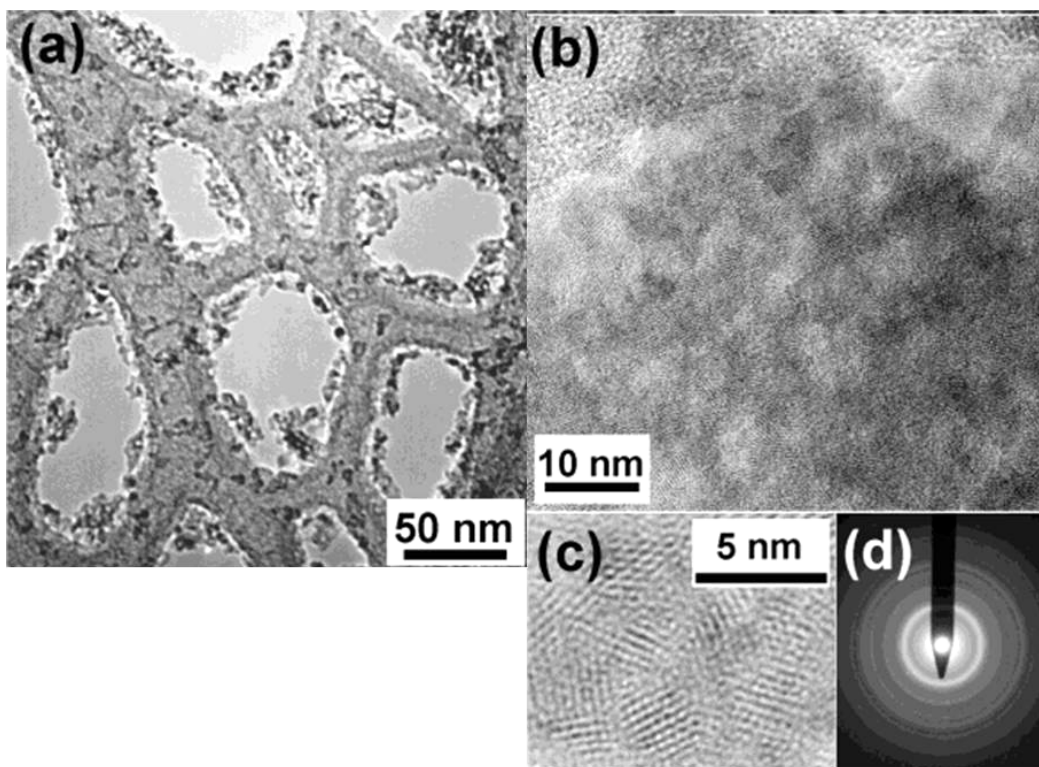


Figure 2-2. Representative TEM micrographs of as-synthesized anatase nanoparticles, obtained at 40 °C.

Hoar and Schulman reported that combinations of water, oil, surfactant, and an alcohol or amine-based co-surfactant produced clear and homogeneous solutions which is called as “microemulsions” [11]. A model of a microemulsion colloidal particle is shown in Figure 2-3, where the surfactant forms spherical aggregates through ion-dipole interactions with the polar co-surfactant. The co-surfactant acts as an

electronegative spacer that minimizes repulsions between the positively charged surfactant heads [12].

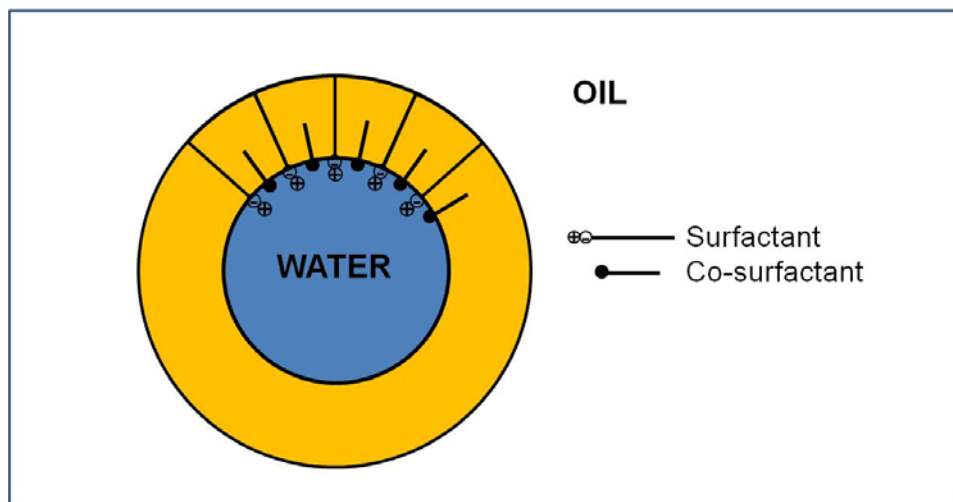


Figure 2-3. Schulman's model of a reverse micelle colloidal particle, as published in 1943 [12].

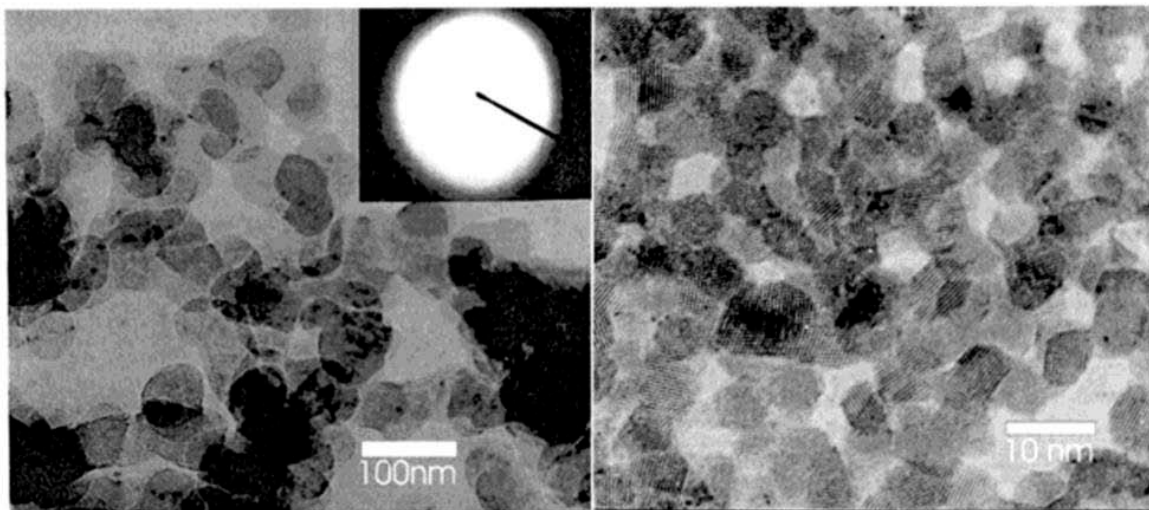


Figure 2-4. Transmission electron micrograph of CTAB-coated cerium oxide nanoparticles annealed at 200 °C and 500 °C for 2 h.

Various oxide nanoparticles, such as  $\text{Al}_2\text{O}_3$ ,  $\text{TiO}_2$  and  $\text{CeO}_2$ , have been synthesized by this microemulsion method [13-16]. Figure 2-4 shows  $\text{CeO}_2$  synthesized

by a micro-emulsion method, in which cetyltrimethylammonium bromide (CTAB) was used as a surfactant.

Most of synthesis methods with aqueous solutions have disadvantages of relatively poor crystallinity and/or polydispersity in their size and shape, in which the pH value of the mixture should be adjusted in both synthesis and washing steps [17, 18].

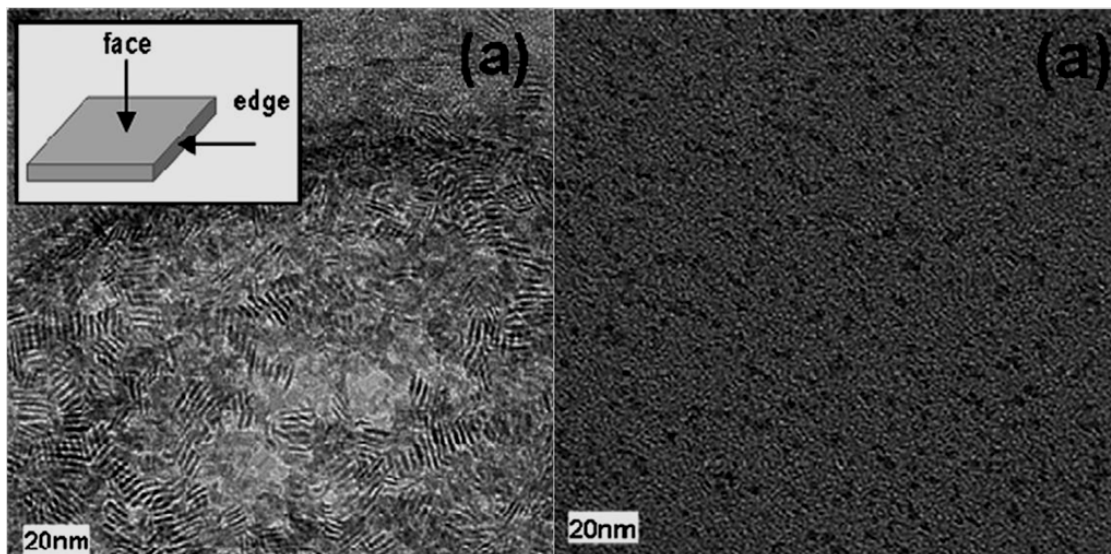


Figure 2-5. HRTEM images of  $Gd_2O_3:Eu^{3+}$  nanoparticles synthesized from thermal decomposition of  $Gd(acac)_3$  precursor using either HDD or TOPO with a  $Gd(acac)_3$ /surfactant.

On the contrary, non-aqueous high temperature thermal reaction methods with organic surfactants can reduce those problems. Nanoparticles synthesized by a non-aqueous colloidal route often exhibit crystallinity and mono-dispersity [19-23]. Furthermore, it gives controllable shapes of nanoparticles through easier controls of growth parameters by changing variables such as the types of surfactants, precursor concentrations and reaction temperatures. It was reported that CdSe quantum dots were prepared by using dimethyl cadmium ( $Me_2Cd$ ) and trioctyl phosphine selenium (TOP-Se) as precursors [24]. S. Seo et. al. used non-aqueous high temperature thermal reaction to synthesize shape-controlled  $Gd_2O_3:Eu^{3+}$  nanoparticles, as shown in Figure

2-5, where the dimensions of nano-plates was an edge length and a thickness of 5 nm and 1 nm, respectively [25].

## 2.1.2 Shape Control of Colloidal Nanoparticles

### 2.1.2.1 Shapes of nanoparticles

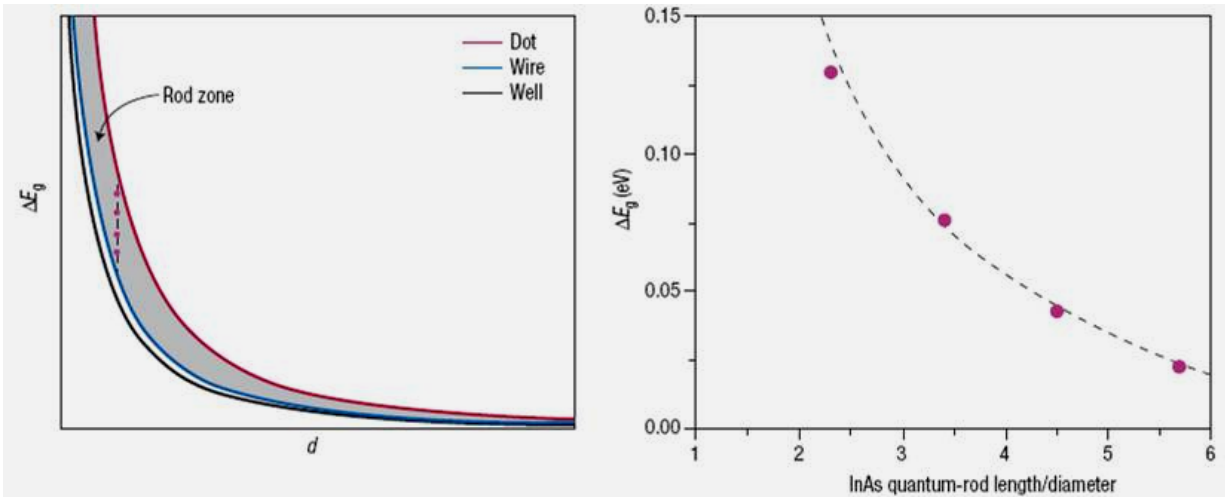


Figure 2-6. Change in bandgap energy,  $\Delta E_g$ , versus  $d$  (thickness or diameter) or length/diameter ratio [26].

It is well known that quantum effects become increasingly important as the size of structures is reduced, but the influence of shape on quantum confinement has been less studied. Buhro and Colvin proposed that shape matters as much as size for nanoparticles [27]. They cited experimental work by Kan et al. which showed that the electronic structure and optical properties of rod-like semiconductor nanocrystals depended sensitively on the ratio of their length and diameter, as illustrated in Figure 2-6 [26]. W.H. Qi and M.P. Wang [28] modeled the effects of shape and size on the lattice parameters of a metallic nanoparticle formed from an ideal bulk crystal. In order to predict shape effects on lattice parameters, they introduced a shape factor. Their data show that the lattice parameter strongly depends on nanoparticle size and shape, as illustrated by Figure 2-7.

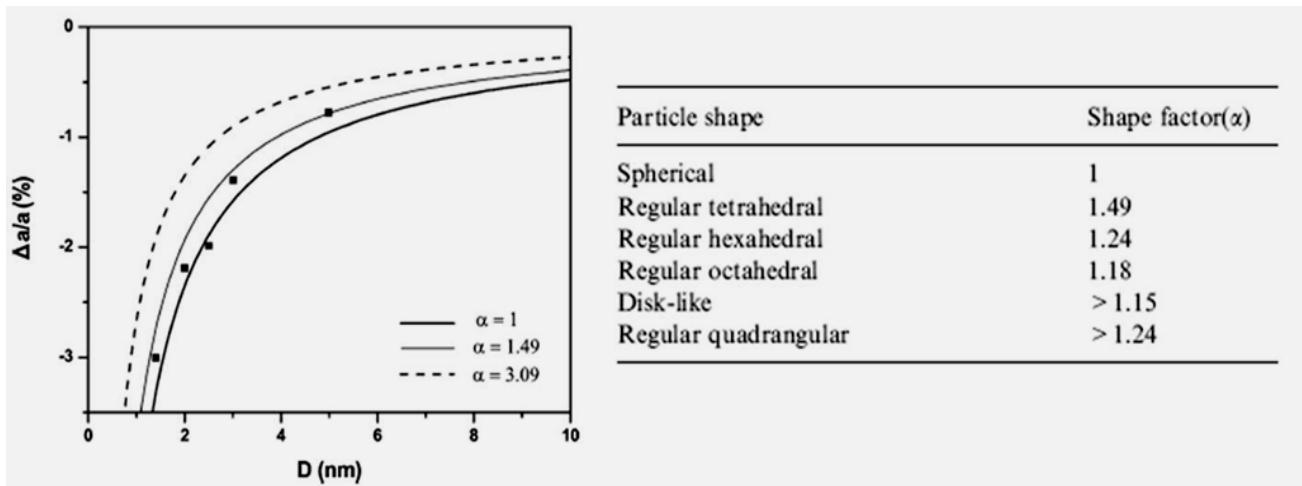


Figure 2-7. Variation of the relative lattice parameter as the function of the diameters of Pd nanoparticles [28].

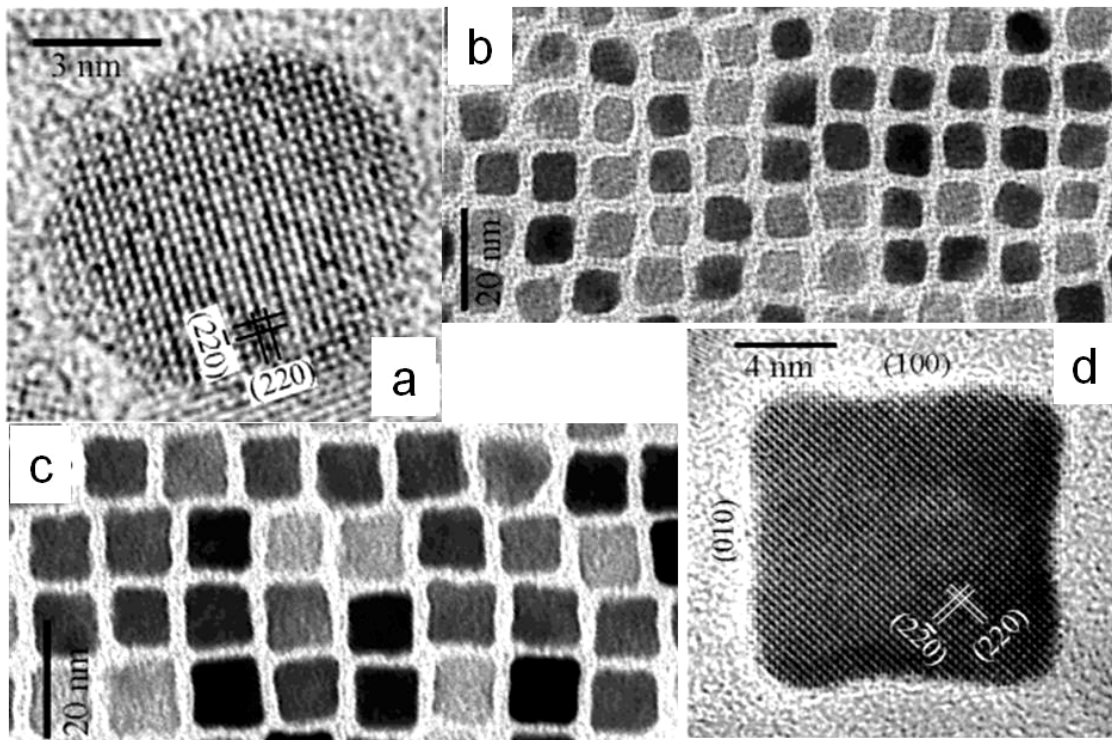


Figure 2-8. HRTEM micrographs of  $\text{CoFe}_2\text{O}_4$  nanocrystals.

Nanoparticles of spheres, cubes and polyhedrons can be classified as zero-dimensional (0 D) structures. Song and Zhang synthesized shape-controlled 0-D nano-

spheres and cubes of  $\text{CoFe}_2\text{O}_4$  [29]. By varying the temperature and heating rate, the shape of  $\text{CoFe}_2\text{O}_4$  nanoparticles could be controlled, as shown in Figure 2-8.

Other shapes of nanoparticles have been reported such as nano-rods, nano-cylinders and nano-disks. Rods, cylinders and wires are one-dimensional (1-D) nanoparticles. Many studies on the synthesis of 1-D nanoparticles have been reported [30-32]. 1-D nanoparticles exhibit novel optical and magnetic properties due to their anisotropic shapes. Nano-rods based on semiconductor materials have been investigated for the application as energy harvesting and light emitting devices. In 2006, Ramanathan et. al. demonstrated electric-field mediated tunable photoluminescence from ZnO nanorods, with potential applications as novel sources of near-ultraviolet radiation [33].

Non-hydrolytic synthesis can be used to produce high quality nano-rods. With increasing hexylphosphonic acid (HPA), CdSe nano-rods with the different aspect ratios (the ratio of the diameter/length of the nanorod) could be synthesized, where 1-D rod shaped nanoparticles results from the preferred growth along the [001] direction of wurtzite CdSe (Figure 2-9) [34].

Discs and plates of polygons are classified as two-dimensional (2-D) nanoparticles. When a specific axis is inhibited during the synthesis, 2-D nanoparticles can be formed. Various 2-D structured nanoparticles were prepared by R. Si et. al, in which a family of rare-earth oxide nanoparticles were synthesized by thermolysis [35]. Due to the selective adsorption of the capping ligands on certain cubic facets during growth, nanoparticles with different morphologies, such as nanopolyhedra, nanoplates, and

nanodisks were created, which exhibit an ability to self-assemble into large-area nanoarrays, as summarized in Table 2-1.

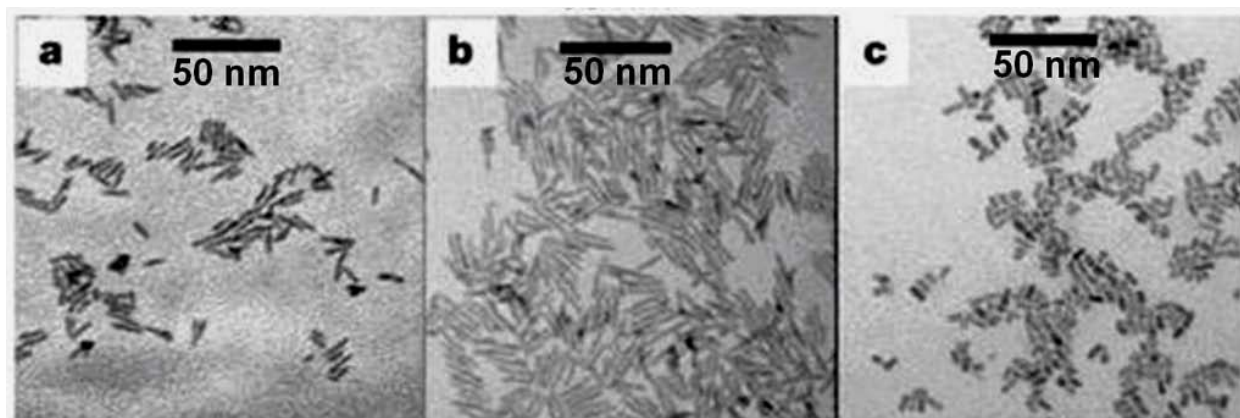


Figure 2-9. CdSe nanorods with different sizes and aspect ratios in different concentrations of HPA /TOPO surfactants.

Table 2-1. Crystal structures and morphologies of the as-obtained rare-earth oxides synthesized by thermolysis of  $\text{Ln}(\text{BA})_3(\text{H}_2\text{O})_2$  ( $\text{Ln}=\text{La}-\text{Y}$ ) or  $\text{Ce}(\text{BA})_4$  in oleic acid (OA)/oleylamine (OM) at 250–330°C for 20–60 min.

	OA/OM	T (°C)	t (min)	Structure	Morphology
$\text{La}_2\text{O}_3$	1:7	330	60	1a3	7 nm nanoplate
$\text{CeO}_2$	0	250	20	Fm3m	2.6 nm nanopolyhedron
$\text{Pr}_2\text{O}_3$	3:5	310	60	1a3	20 nm nanoplate
$\text{Nd}_2\text{O}_3$	3:5	310	60	1a3	11 nm nanoplate
$\text{Sm}_2\text{O}_3$	3:5	310	60	1a3	11 nm nanoplate
$\text{Eu}_2\text{O}_3$	3:5	310	60	1a3	26 nm nanodisk
					12 nm nanoplate
$\text{Gd}_2\text{O}_3$	3:5	310	60	1a3	32 nm nanodisk
					30 nm nanodisk
$\text{Tb}_2\text{O}_3$	3:5	310	60	1a3	34 nm nanodisk
$\text{Er}_2\text{O}_3$	3:5	310	60	1a3	43 nm nanodisk
$\text{Y}_2\text{O}_3$	3:5	310	60	1a3	65 nm nanodisk

### 2.1.2.2 Growth mechanism of shape-controlled nanoparticles

The precipitation of nanoparticles has often been discussed in numerous books and review articles [36-38]. Nucleation is a key step in the precipitation process which

can be explained by thermodynamics. Assuming that some of atoms of the liquid cluster together to form a small sphere of solid, the free energy of the systems can be express by [39]:

$$G_1 = (V_S + V_L)G_V^L \quad (2-1)$$

$$G_2 = V_S G_V^S + V_L G_V^L + A_{SL} \gamma_{SL} \quad (2-2)$$

Where  $G_1$  and  $G_2$  are free energy of two systems,  $V_S$  is the volume of the solid sphere,  $V_L$  the volume of liquid,  $A_{SL}$  is the solid/liquid interfacial area,  $G_V^S$  and  $G_V^L$  are the free energies per unit volume of solid and liquid respectively, and  $\gamma_{SL}$  the solid/liquid interfacial free energy. The change of free energy ( $\Delta G_r$ ) from  $G_1$  to  $G_2$ , with a sphere of radius  $r$ , is given by Equation 2-3 as

$$\Delta G_r = -\frac{4}{3}\pi r^3 \Delta G_V + 4\pi r^2 \gamma_{SL} \quad (2-3)$$

It can be seen from Figure 2-10 that for a given undercooling, cooling a material below the transformation temperature without obtaining the transformation, there is a certain radius,  $r^*$ , which is associated with a maximum excess free energy. When  $r > r^*$ , the free energy of the system decreases if the solid either grows or shrinks. The critical radius of the solid nuclei can be expressed by:

$$r^* = \frac{2\gamma_{SL}}{\Delta G_V} = \frac{2\gamma_{SL} T_m}{\Delta H_S} \frac{1}{\Delta T} \quad (2-4)$$

where  $H$  is the enthalpy of fusion and  $\Delta T$  is the degree of undercooling.

The initial stage of the growth of nuclei can be explained by heterogeneous nucleation limited by either diffusion or reaction rates. For diffusion-limited growth, concentration gradients and temperature control the growth rate. Ostwald ripening is a secondary growth process in which smaller particles are consumed by larger particles [40, 41]. The

size, morphology and properties of nanoparticles are dramatically affected by the Ostwald ripening.

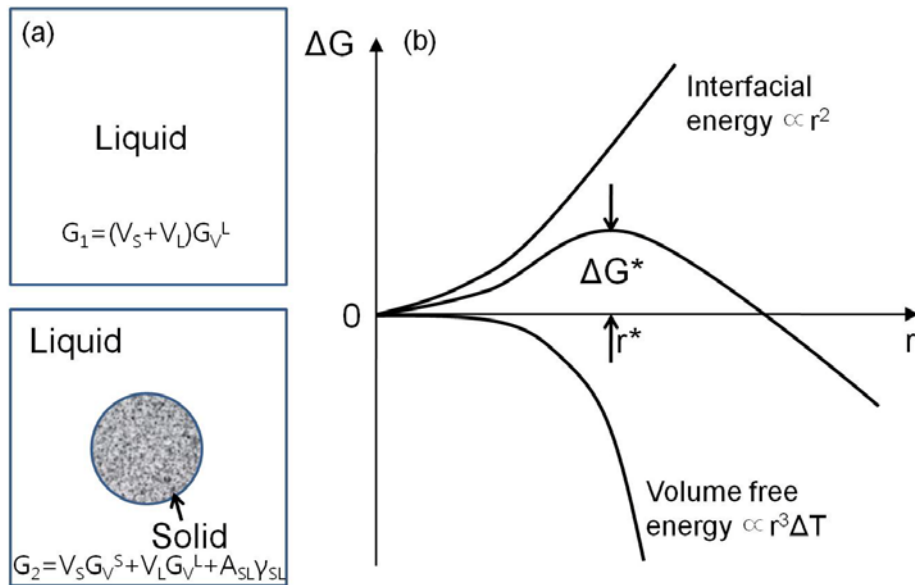


Figure 2-10. Homogeneous nucleation and the free energy change associated with homogeneous nucleation of a sphere of radius  $r$ .

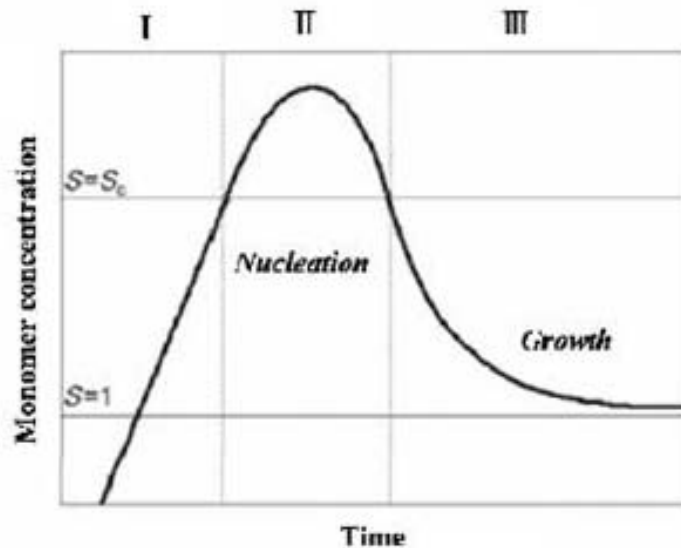


Figure 2-11. Lamer plot with illustration of nucleation and growth diagram.  $S = S_c$ : critical saturation of monomer concentration to induce nucleation.  $S = 1$ : equilibrium monomer concentration below which growth stops.

A Lamer plot is used to describe the formation of clusters and colloids in homogeneous and supersaturated solutions[42, 43]. As illustrated in Figure 2-11, in the

first stage, the concentration of monomer (precursor) is increased with reaction time. When the monomer (precursor) reaches a sufficiently high concentration, nucleation can occur (stage 2). The growth of nuclei causes the monomer (precursor) concentration to fall, stopping nucleation. Until the monomer (precursor) concentration falls to the  $S=1$  level, the nanoparticles continue to grow (stage 3) [43].

The most frequently reported model for the mechanism of shape control is the Wulff facets argument or Gibbs-Curie-Wulff theorem, which states that the shape of nanoparticles is determined by the specific surface energy of each face of the nanocrystal [44]. However, many other reports revealed that the theories based on thermodynamics cannot explain most of the cases.

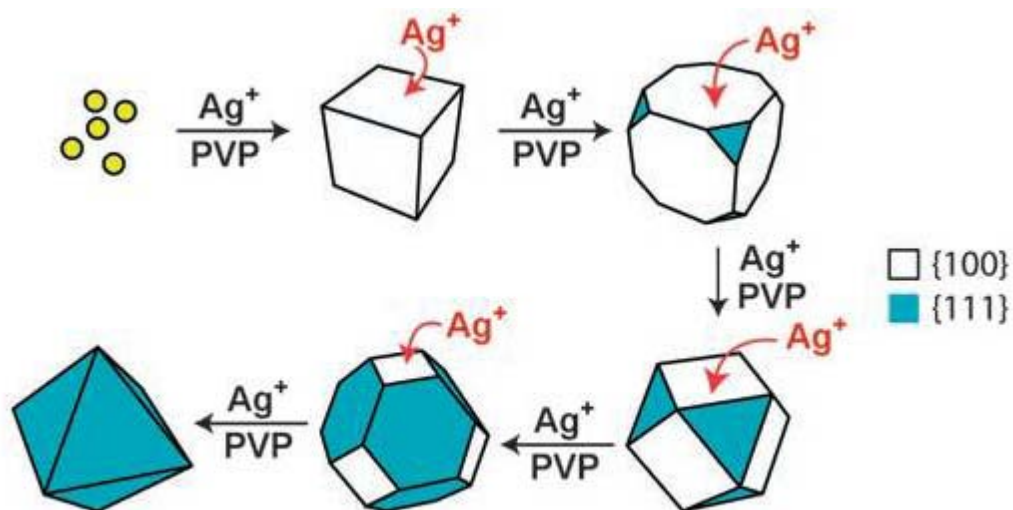


Figure 2-12. A schematic of the nucleation and growth process, in which silver continuously deposits onto the (100) facet to eventually result in a complete octahedron with (111) facet.

Tao et al reported on shape-controlled Ag nanocrystals synthesized using the polyol method and controlling reaction kinetics [45]. Fast nucleation and fast growth produced nanowires whereas fast nucleation and slow growth formed polyhedral nanocrystals. Shape evolution of Ag nanocrystals was also investigated by extending

the polyol reaction for a given time period. As shown in Figure 2-12, the cubic Ag has evolved to octahedrons to form completely (111)-bound symmetry which is a low surface energy facet [45].

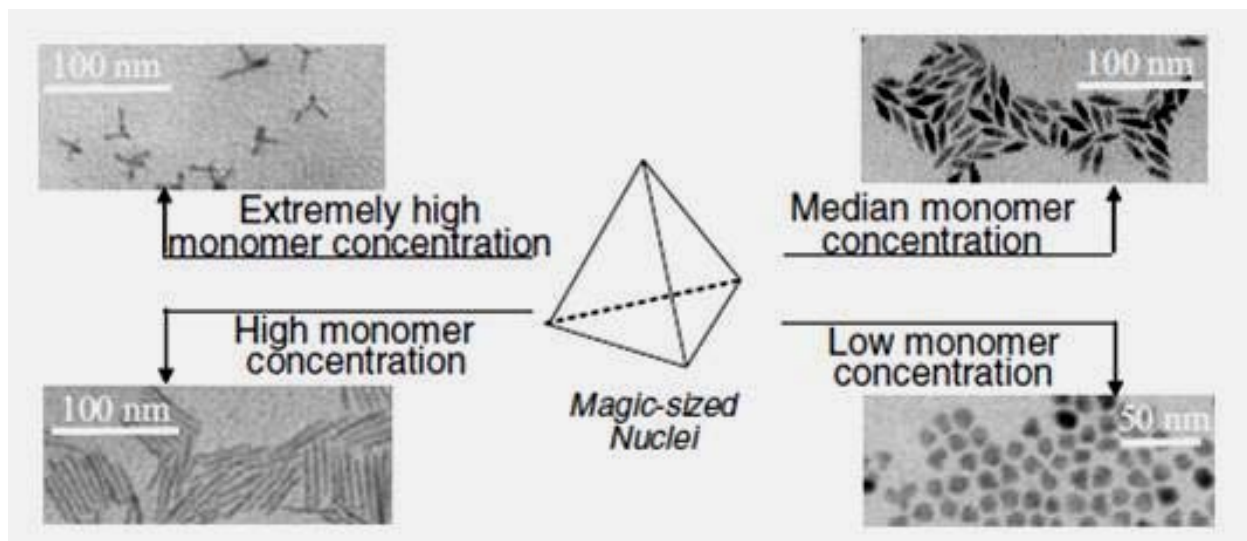


Figure 2-13. Monomer-concentration-dependent growth path of CdSe nanocrystal.

The anisotropic growth of CdSe nanoparticles was studied by X. Peng [46] by modulating the reaction kinetics varied with the monomer(precursor) concentrations . The concentration of monomers (precursors) after the nucleation process is a critical factor in the control of the nanoparticles shape. For a high monomer concentration, the solution could supply sufficient monomers to the nuclei to grow arms on the (111) faces of the zinc blende structure of the tetrahedral nuclei, which results in tetrapods. A moderately high monomer (precursor) concentration results in the growth of a single arm to produce the one-dimensional nanorods or nanowires. Medium and low monomer (precursor) concentrations produce oval and spherical nanoparticles, respectively, due to the low chemical potentials. Figure 2-13 illustrates the correlation between shape and monomer (precursor) concentrations for CdSe nanoparticles.

Surfactants also play a huge role in shape control of nanoparticles. Rui Si et. al reported the effect of surfactants on the shape of  $\text{CeO}_2$  and  $\text{Ln}_2\text{O}_3$  ( $\text{Ln}=\text{La}-\text{Y}$ ) nanoparticles [35]. Their experiments showed that  $\text{CeO}_2$  nuclei grew in a three-dimensional mode to generate nano-polyhedral shapes enclosed by both (111) and (200) facets with oleylamine, since oleylamine is characterized by its non-selective adsorption on faces of nanocrystals. On the contrary, the growth with oleic acid is anisotropic. The denser faces such as (111) plane of FCC structures are selectively capped by oleic acid, which means that the nuclei grow in a two-dimensional mode to produce nano-plates with confined (001) planes or nanodisks with restricted (111) planes, as shown in Figure 2-14.

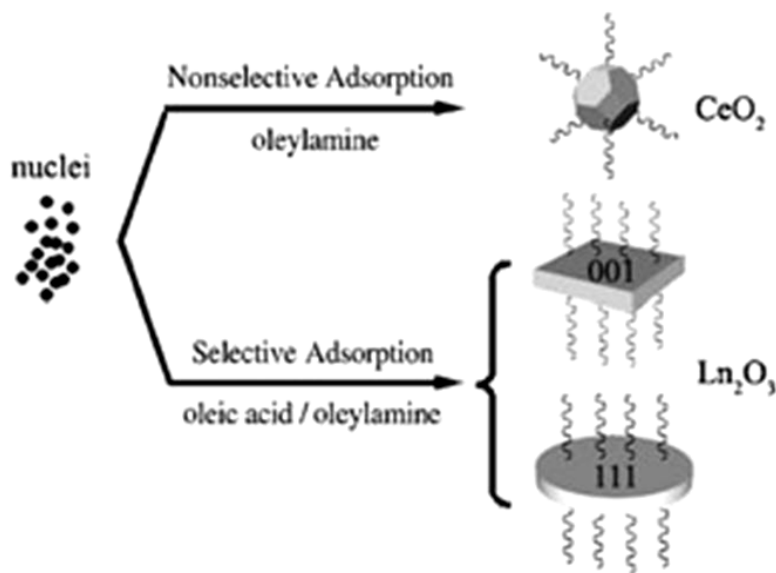


Figure 2-14. Formation of rare-earth oxide nanopolyhedra, nanoplates, and nanodisks.

## 2.2 Inorganic Luminescent Materials

### 2.2.1 Fundamentals of Luminescent Materials

The definition of luminescent materials is a solid which converts certain types of energy into electromagnetic radiation. Luminescent materials can be excited by

electromagnetic waves, electron beams, voltage, X-rays,  $\gamma$ -rays,  $\beta$  particles, neutrons, and so on. The important physical processes which play a role in luminescent material can be described by [47]:

1. Absorption of energy (excitation) which may occur in the luminescent center (activator) itself, in another ion (the sensitizer), or in the host lattice.
2. Energy transfer to luminescent centers.
3. Emission from the activator.
4. Non-radiative return to the ground state, which decrease the luminescent efficiency.

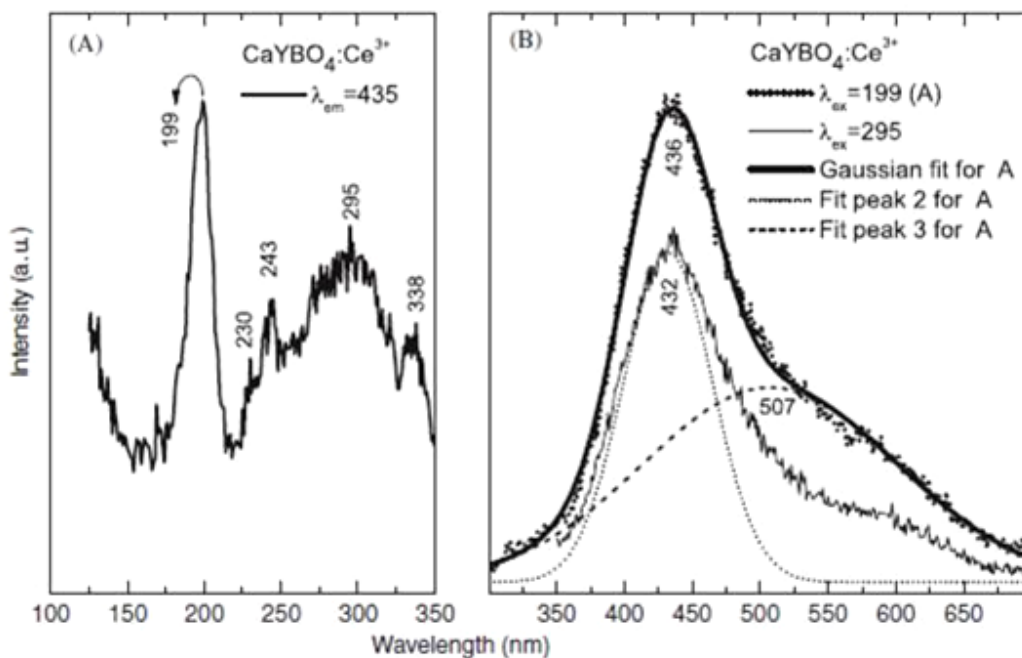


Figure 2-15. The excitation curve of  $\text{CaYBO}_4:\text{Ce}^{3+}$  monitored at 435 nm and the emission curves of  $\text{CaYBO}_4:\text{Ce}^{3+}$  excited at 199 nm (dotted line, marked at curve A) and 295 nm (thin solid line).

A luminescent material only emits light after absorption of the excitation energy. The absorption will occur at activators, sensitizers and by the host lattice, as noted above. The rare-earth ions are commonly used as activators in luminescent materials.

They are characterized by an incompletely filled 4f shell. For example,  $\text{Eu}^{3+}$ ,  $\text{Yb}^{3+}$ ,  $\text{Er}^{3+}$  and  $\text{Nb}^{3+}$  ions show charge-transfer absorption bands and  $\text{Ce}^{3+}$ ,  $\text{Pr}^{3+}$ ,  $\text{Tb}^{3+}$  show 4f  $\rightarrow$  5d absorption bands in the ultraviolet [47]. A typical photoluminescence excitation (PLE) spectrum from  $\text{Ce}^{3+}$  doped  $\text{CaYBO}_4$  is shown in Figure 2-15 [48]. The absorption of energy does not necessarily take place at the activator, but may also occur in the host lattice. There are two different classes of optical absorption transitions. One results in free electrons and holes and another does not make free charge carriers [47].  $\text{ZnS}$  is an example of the former class. It is a compound semiconductor. Optical absorption occurs for energies larger than the width of the band gap ( $E_g$ ) and it creates electrons in the conduction band and holes in the valence band. However, not every host lattice makes free charge carriers by optical excitation. For example, in  $\text{CaWO}_4$ , energy is absorbed in the  $\text{WO}_4^{2-}$  complex. In the excited state of the tungsten group, the hole and the electron form an exciton.

Once luminescent materials absorb enough energy to make excited carriers or excitons (electron-hole pair), light is emitted by relaxation of excited carriers to lower energy state, and ultimately to the ground state. In terms of the emission from activators, rare-earth ions could be used for a typical example. The emission of  $\text{Eu}^{3+}$  ions consists usually of peaks with a small FWHM because they show parallel parabolas ( $\Delta R = 0$ ) in a configurational coordinate diagram [47]. The line emissions corresponds to transitions from the excited  $^5\text{D}_0$  to the  $^7\text{F}_J$  ( $J = 0, 1, 2, 3, 4, 5, 6$ ) levels of the  $4f_6$  configuration [49]. The transition  $^5\text{D}_0 \rightarrow ^7\text{F}_{2,4}$  of  $\text{Eu}^{3+}$  is a forbidden electric-dipole transition (parity selection rule), whereas the  $^5\text{D}_0 \rightarrow ^7\text{F}_{1,3}$  of  $\text{Eu}^{3+}$  is an allowed magnetic-dipole transition [47].

However, this selection rule can be relaxed for  $\text{Eu}^{3+}$  in a host lattice lacking inversion symmetry, such as  $\text{Gd}_2\text{O}_3$ ,  $\text{Y}_2\text{O}_3$  and  $\text{LaPO}_4$  [50-52].

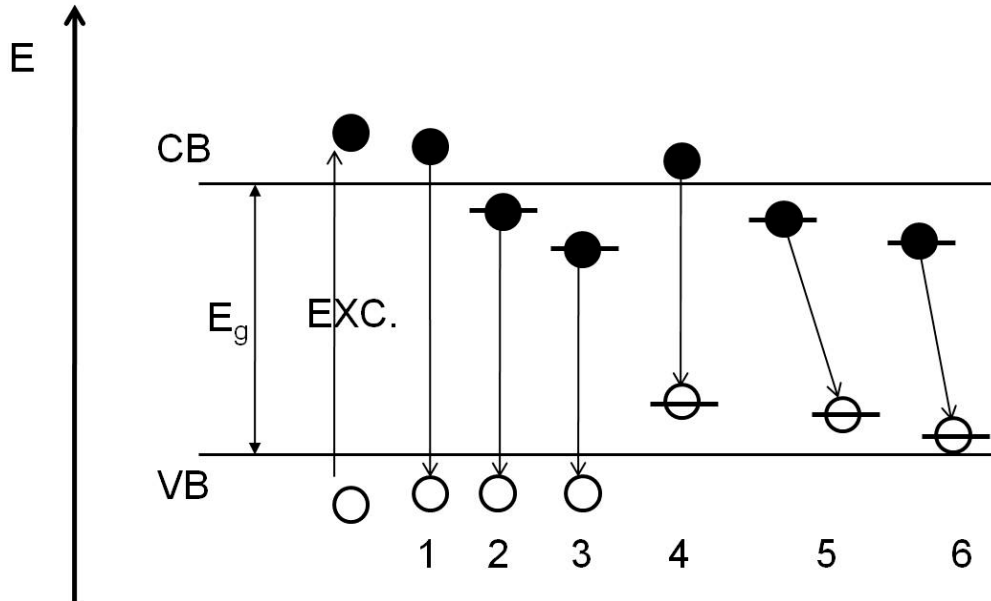


Figure 2-16. Emission transitions in a semiconductor. The band gap  $E_g$  separates the valence band (VB) and the conduction band (CB). Excitation over the band gap creates electrons in CB and holes in VB.

In semiconductors, there are several paths to explain a radiative process. As illustrated in Figure 2-16, emission from a semiconductor can be achieved by [47]:

- (1) recombination of free electrons and holes
- (2) a free hole recombines with an electron trapped in a shallow trap level
- (3) the same with a deep electron-trapping level
- (4) a free electron recombines with a trapped hole
- (5) doner-acceptor pair emission
- (vi) electron-hole recombination at a donor-acceptor complex  
(e.g. at coupled defects such as vacancy and substitution of atoms)

Emission due to recombination of free electrons and holes is exceptional. Usually recombination occurs close to or at defects in the crystal lattice so that the emitted

wavelength should be increased (lower energy). This energy shift is called the Stokes shift and is shown for a CdS nanorods in Figure 2-17 [53].

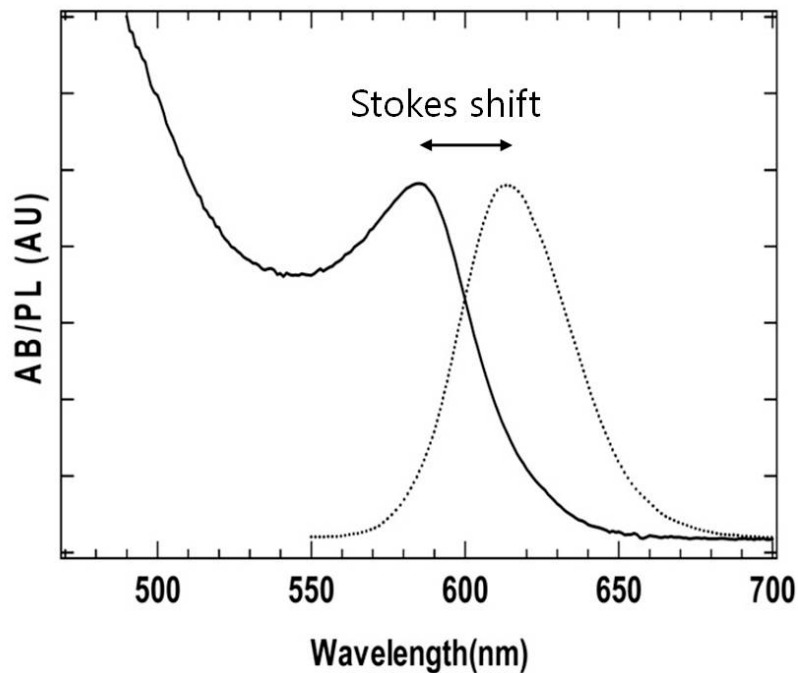


Figure 2-17. Absorption (solid lines) and photoluminescence (dotted lines) spectra of CdS nano-rod.

### 2.2.2 Application of Luminescent Materials

The application of luminescent materials can be classified by the excitation sources for the luminescent materials as shown in Table 2-2 [54]. Luminescent materials can be found in a broad range of everyday applications such as cathode ray tubes (CRTs), projection televisions, fluorescent lamps, X-ray detectors, solid state lighting, sensors, and displays. Generally, research and development on luminescent materials has resulted in synthesis and testing of thousands of phosphors [54]. However, only about 50 materials exhibit properties that are suitable for appropriate technological applications in terms of efficiency, emission color, decay time, physical stability, availability of raw materials, environmental aspects, cost, reproducibility and ease of materials preparation [55-57].

Table 2-2. Applications of luminescent materials classified by different excitation sources.

Excitation	Excitation energy	Application
Electron beam	10-30 kV	CRT TV, Field Emission Display
UV ray	200 – 400 nm	Fluorescent lamps, plasma display, neon sign
UV-Vis-IR	>400 nm	Luminous paint, pigments
High energy radiation		Scintillators, radiographic imaging devices
Electric field		Inorganic EL, organic EL

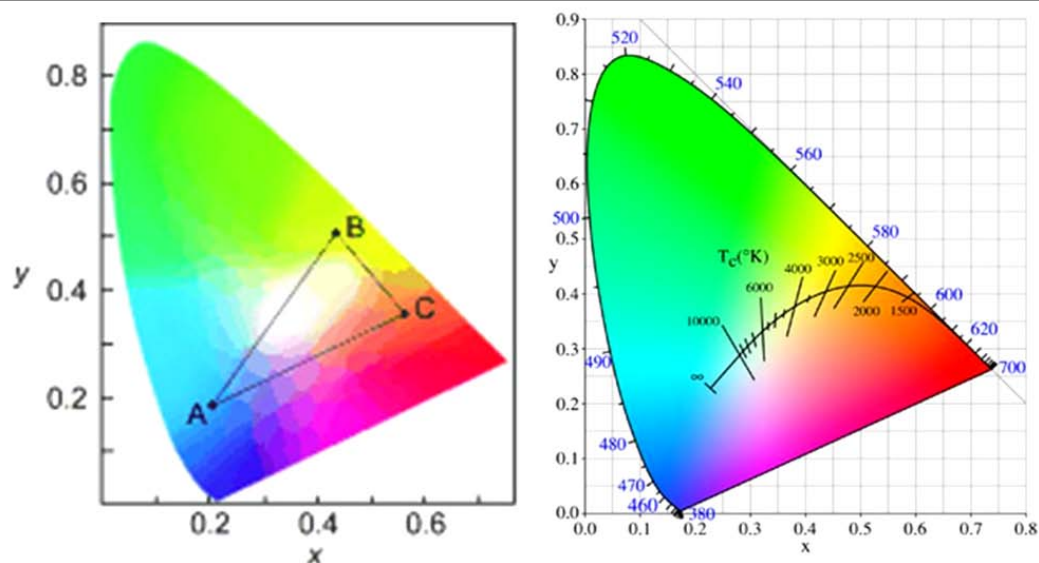


Figure 2-18. Color diagram of the CIE (CIE=Commission Internationale d'Eclairage) and CIE with Color Temperature Line.

Recently, an important application of luminescent material is to create white light emitting diodes (LEDs). White light can be generated by combining the output from blue, green and red-emitting diodes to yield white light. There are three different technical approaches to realize inorganic white LEDs [58]. The first successful device combined a blue LED covered with a classical yellow phosphor, such as yttrium aluminum garnet  $Y_3Al_5O_{12}$  doped with  $Ce^{3+}$  (YAG:Ce<sup>3+</sup>) [59]. These LEDs have been widely used as simple long-life white-light sources in traffic lights, cycle lamps, car headlights, outdoor

lighting or flashlights. The white light looks 'cold' due to its high color temperature (CCT=>5000K). More specific applications like indoor lighting require warm-white light and an excellent color rendering. The white light should contain red wavelength regions and thus exhibit a lower color temperature. These targets are achieved by a combination of a blue (Ga,In)N LED with two phosphors emitting red and green light [60].

In the third approach suitable phosphors for (Ga,Al)N UV LEDs are developed. These are covered with three different phosphors, which emit red, green, and blue. The advantage of these white LEDs is that they enable variation of three broad-band emitters, giving access to a larger color area in the CIE diagram (Figure 2-18) and better color rendering [61].

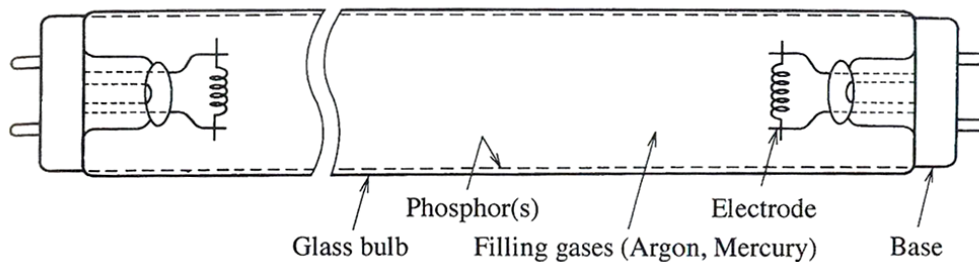


Figure 2-19. Fundamental construction of the fluorescent lamp.

A fluorescent lamp is a classic application of luminescent materials. The fluorescent lamp or fluorescent tube is a gas-discharge lamp that uses electricity to excite mercury vapors. The main emission from a mercury discharge can be tuned from 185 to 254 to 365 nm when the mercury gas pressure is increased. In fluorescent lamps, a combination of phosphors emitting at the appropriate colors are coated on the inside of the discharge tube, as shown in Figure 2-19. Selection of the appropriate luminescent

materials enables special application of fluorescent lamps such as security marking, sun-tanning, photocopying, display backlight and advertising billboards [62].

### **2.3 Scintillation Materials**

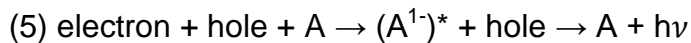
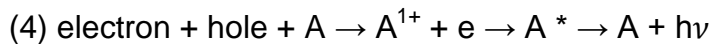
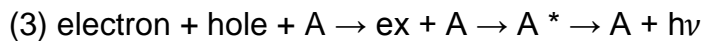
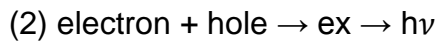
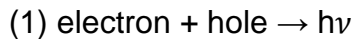
An important application of luminescent nanoparticles is a scintillator. Scintillators are substances that absorb high energy electromagnetic or charged particle radiation then, in response, emit photons at a desirable wavelength, releasing the previously absorbed energy. Scintillators are used in several physics research and military applications to detect electromagnetic waves or particles. Scintillators are usually made of bulk single crystalline materials, which are very expensive and hard to make. Key factors for good scintillator materials are [63].

- ◆ High atomic number and density (Improve photo-absorption)
- ◆ Short decay time (Improve time resolution)
- ◆ High efficiency of emitting UV or visible light (Large light output)
- ◆ Low afterglow
- ◆ Low cost - Bulk is very expensive

Scintillator materials are characterized by high stopping power, which makes them well-suited for detecting high-energy radiation so that high atomic number materials have to be used. Shorter decay time results in higher count rates and time resolution. Afterglow is the phenomenon that luminescence can still be observed a long time after the end of the excitation pulse. A long time here is defined as a time much longer ( $\geq 5X$ ) than the decay time of the luminescence. So, for the improvement of detection, low afterglow is a necessary behavior of good scintillator materials.

### 2.3.1 Fundamentals of Scintillation Materials

The mechanisms of excitation of the luminescent centers (activators) in a scintillator are strongly influenced by the surrounding medium. The coupling between the lattice and activators is essential in the way the energy is transferred between them. Electrons and holes created by absorption of high energy radiation have several possible pathways for the scintillation process [64]:



where A means activator ions and A\* represents their excited states.

The simplest scintillation process (1) is the result of the direct radiative recombination of free electrons in the conduction band with holes in the valence band. In most cases, the recombination takes place when the energy of electrons and holes decreases because they form bonding states called excitons (ex) with energy smaller than the bandgap. The excited carriers can also be bound in the lattice, for example, in the vicinity of a specific structural defect (2). They are called auto-localized excitons and their radius depends on the electrostatic field in the configuration. Luminescence from free or bound excitons has been observed so far only in simple oxides [65].

Sometimes, in the presence of impurity centers or activator ions (A), the exciton luminescence is efficiently quenched, causing a sensitization of the luminescence of the

activating ions A. In this case, the excitation of radiative centers results from an energy transfer from excited matrix states. The process competing to the formation of excitons is the direct capture of free thermalized carriers, electrons (4) or holes (5) by activating ions (A) with the subsequent formation of their excited state ( $A^*$ ). The cross section for electron or hole capture depends on the nature of the activator ion and on the structure of the local electrostatic field in its vicinity. Finally, the direct excitation of activated centers by ionizing radiation (6) provides a crucial contribution to the scintillation in the case of self-activated or heavy doped scintillators.  $CeF_3$  shows a typical example of the direct excitation.

After excitation from high energy particles or high energy electromagnetic waves, relaxation of electronic excitations involves complex mechanisms. A description of multiplication and thermalization processes has been proposed by different authors using various models[66-68]. Vasil'ev proposed a schematic model that uses simple schemes of relaxation of electronic excitations deduced from simulation and which account qualitatively for the energy distribution and space correlation of excitations. Figure 2-20 shows two different schemes of relaxation, one is the general case and another is that of rare-earth containing scintillators. As shown in Figure 2-20 (a), the first stage starts with the production of primary excitations by interaction of ionizing particles with the material. For extremely high energy particles, the excitations are essentially deep holes and hot electrons which are created in inner-core bands and in the conduction band, respectively.

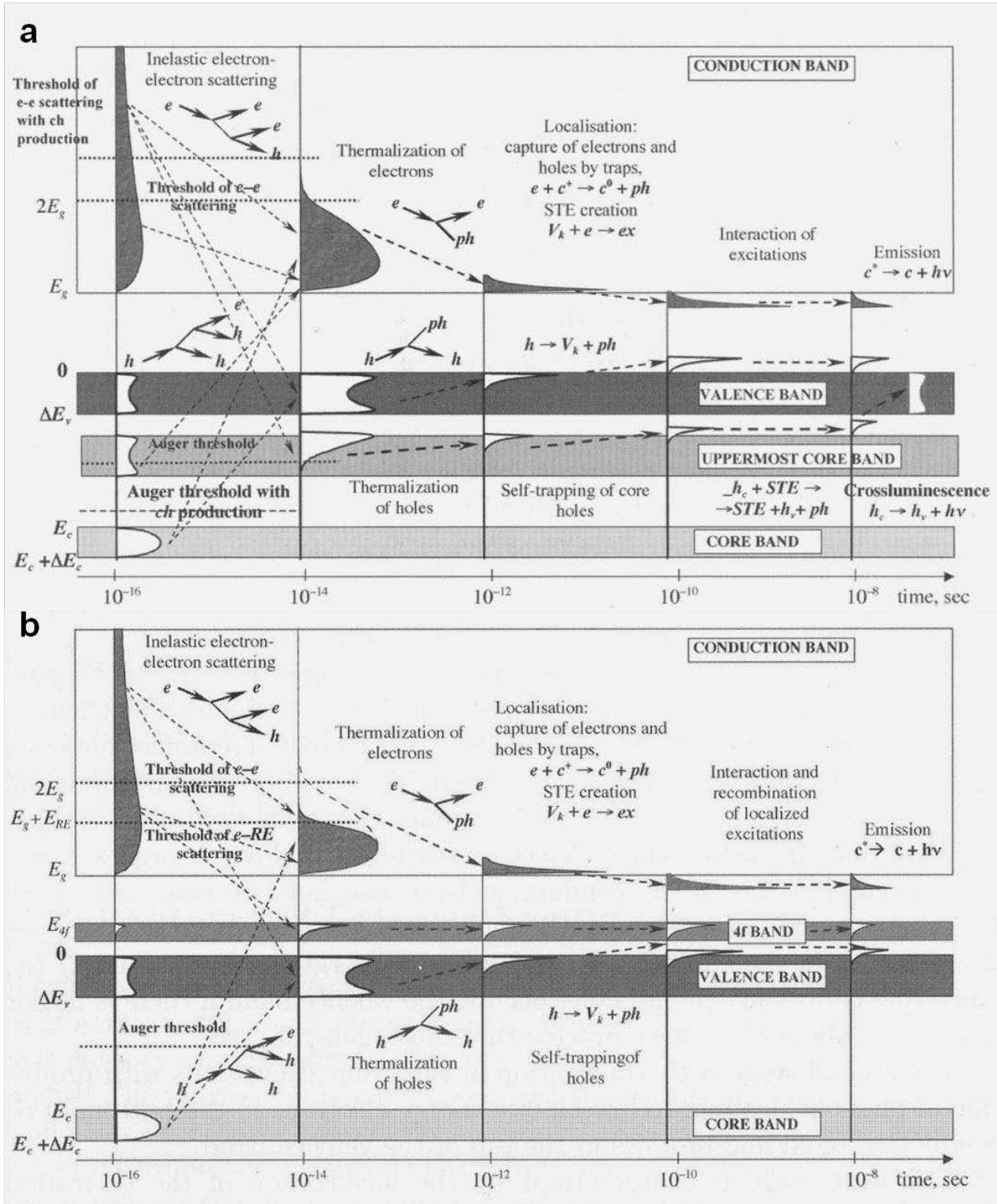


Figure 2-20. Scheme of relaxation of electronic excitations general scheme, and rare-earth containing scintillators.

In a very short time ( $\sim 10^{-15}$  s), a large number of secondary electronic excitations are produced through inelastic electron-electron scattering and Auger processes with creation of electrons in the conduction band and holes in shallow core and valence bands. At the end of this stage, the multiplication of excitations stops. The second state is thermalization of electronic excitations with production of phonons, leading to low kinetic energy electrons in the bottom of the conduction band and of holes in the top of the valence band. The third stage is characterized by the localization of the excitations through their interaction with stable defects and impurities of the material. The two last steps are related with migration of relaxed excitations and radiative and/or non-radiative recombination. Rare-earth doped scintillators exhibit a more complicated mechanism. Since the doping level is located between the forbidden band-gap, they have additional pathway of excitation and would be expected to have a high light yield (Figure 2-20 (b)).

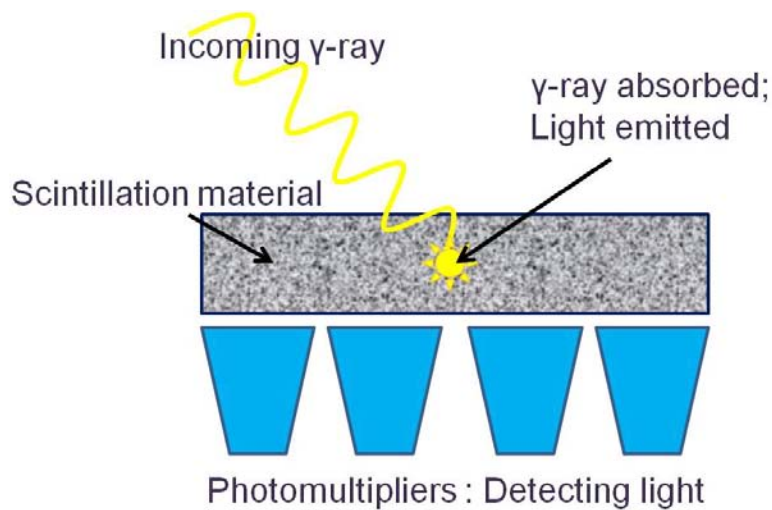


Figure 2-21. Schematic diagram of a scintillation detector

Figure 2-21 helps the reader to understand the process of a scintillation detector. Briefly summarizing, as soon as an incoming radiation is absorbed by a scintillation

material, the ray will excite the scintillation material, then detectable light will be emitted and detected by photo-multipliers.

### 2.3.2 Application of Scintillation Materials

Van Eijk et al. have summarized the most important requirements for a number of applications of scintillating materials as presented in Table 2.3 including the following characteristics: relative light yield  $L_R$ , decay time  $\tau$ , density, atomic number  $Z$ , emission spectrum ( $\lambda_r$ ), ruggedness (Rug.) and radiation hardness (Rad H) [69].

Table 2-3. Scintillator requirements in various applications.

Application	LR (ph/MeV)	$\tau$ (ns)	Density (g/cm <sup>3</sup> )	Z	$\lambda_r$ (nm)	Rug.	Rad H (Mrad)
HEP	>200	<<20	High	High	>450	+	>10
IEP	High	Varies	High	High	>300	+/-	+/-
Nuclear physics	High	Varies	High	High	>300	-	-
Astrophysics	High	Less imp.	High	High/low	>450	+	-
PET	High	<1	High	High	>300	-	-
Gamma cameras	High	Less imp.	High	High	>300	+/-	-
Positron lifetime	High	<1	High	High	>180	-	-
Synch. Rad. Det.	High	10-100	High	High	>300	-	-
Industrial appl.	High	Varies	High	High	>300	+	-
Neutrons	High	10-100	Low	Li,B,Gd	>300	-	-
X-ray CT	High	No afterglow	>4	>50	>450	-	+
X-ray imaging	High	Less imp.	High	High	>450	+/-	+

Calorimeters are typical examples of high energy physics (HEP) applications of scintillator materials. The purpose of calorimeters is the measurement of energy of particles. For HEP, an ideal calorimeter would require a fast, dense and radiatively hard scintillator with a reasonably low light output. In terms of high density to reduce the total volume, low melting point and easy and cheap production method, lead-based compounds, particularly  $PbWO_4$ , can be promising scintillators for HEP [70].

Positron emission tomography (PET) is widely used in medical radiology. Scintillators for PET applications should meet the following requirements: (1) high density, (2) light output > 5~10 % of that of NaI:Tl and (3) decay time <3~5 ns.

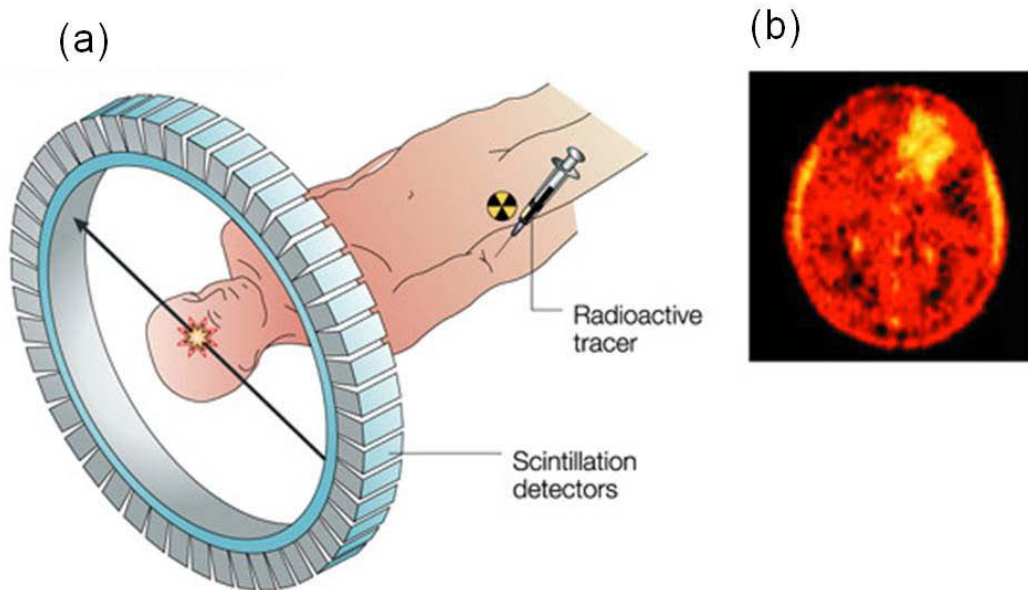


Figure 2-22. Schematic diagram of positron emission tomography (PET) with the inset illustrating BGO detectors coupled with PMT and a PET scan image of a brain.

A  $\text{Bi}_4\text{Ge}_3\text{O}_{12}$  (BGO) crystal has properties that best meet these requirements. In general, PET systems consist of many rings with a number of scintillation detectors, as illustrated in Figure 2-22 (a) so that a 3D image of processes in the body can be reconstructed, as shown in Figure 2-22 (b) [71-73]. Inorganic scintillators are often used in gamma spectroscopy. Figure 2-23 shows a typical pulse height spectrum of 662 keV gamma rays originated from a  $^{137}\text{Cs}$  source by using the  $\text{Lu}_2\text{SiO}_5:\text{Ce}$  (LSO) scintillator crystal [74]. The dominant peak at the right side is the full energy peak containing events in which the total 662 keV energy was absorbed in the crystal. In the low energy regime, the Ba K peak of X-ray emission at 32 keV is observed as a result of  $^{137}\text{Cs}$  decay.

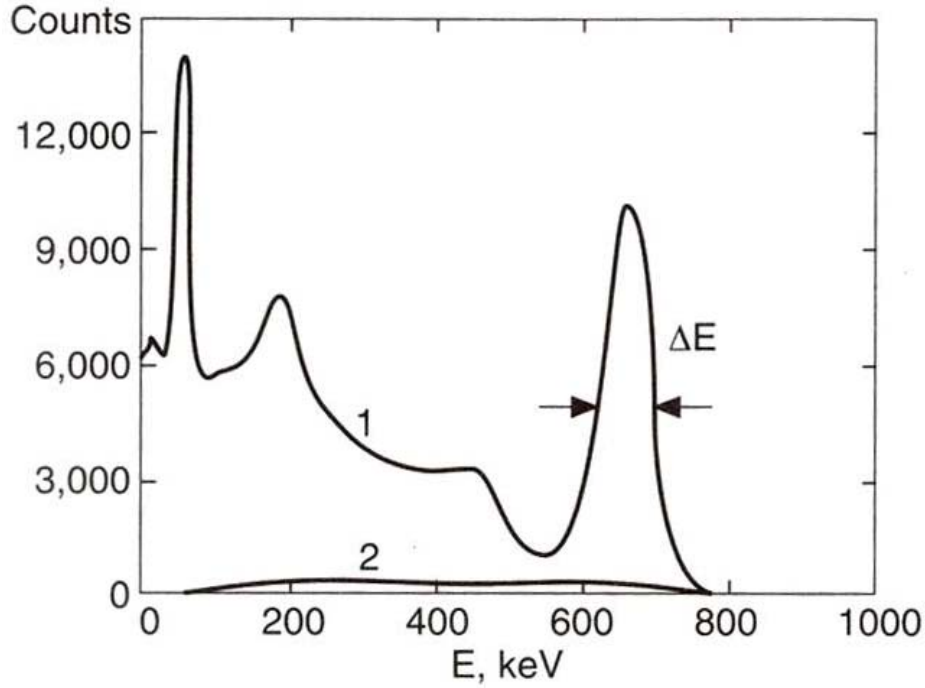


Figure 2-23. Pulse-height spectrum of a  $^{137}\text{Cs}$  source measured with a  $100\text{cm}^2$  area and 2mm depth with LSO crystal coupled with a Hamamatsu R878 PMT.

## 2.4 Luminescent Nanoparticles

Low dimensional systems reviewed in this section are zero-dimensional (0-D) systems, one-dimensional systems (1-D) and two-dimensional systems (2-D).

### 2.4.1 Fundamental and Application of Luminescent Nanoparticles

One of the most remarkable characteristics of luminescent nanoparticles with low dimensions is their physical and optical modification through different distributions of energy levels and densities of states. The origin of different quantum states is the spatial confinement of electrons and holes inside the nanoparticles. The density of states of each low dimensional nanostructure can be describe by [75]:

$$\rho_{2D}(E) = \frac{\mu}{\pi\hbar^2} \sum_n \theta(E - E_n - E_g) \quad (2-5)$$

$$\rho_{1D}(E) = \frac{(2\mu)^{1/2}}{\pi\hbar} \sum_{m,n} \frac{1}{(E - E_m - E_n - E_g)^{1/2}} \quad (2-6)$$

$$\rho_{0D}(E) = 2 \sum_n \delta(E - E_l - E_m - E_n - E_g) \quad (2-7)$$

where,  $\theta$  is a step function and  $\delta$  is a delta function and the  $E_{\text{sub}}$  refer to the three directions of spatial confinement. Figure 2-24 describes the density of states for three low dimensional systems using a particle-in-a-box model [75, 76].

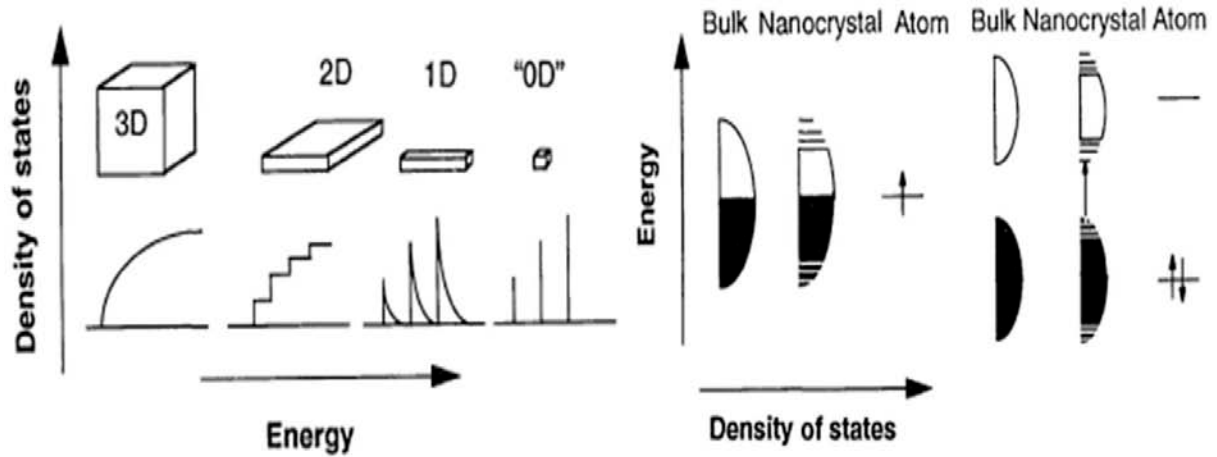


Figure 2-24. Schematic illustration of the density of states in metal and semiconductor clusters.

Luminescent nanoparticles can be divided by two different categories, undoped and doped nanoparticles. Semiconductor nanoparticles are representative for undoped nanoparticles. II-VI (CdSe, CdTe, CdS and ZnSe) and III-V (InP, InAs) nanoparticles have been synthesized and studied due to their tunable emission in the visible range [77-81]. Among these semiconductor nanoparticles, CdSe nanocrystals are the most widely studied due to their tunable emission wavelength in the visible range. In 1993, Bawaendi et al developed a unique synthesis of CdS, CdSe and CdTe nanoparticles using the high temperature organometallic procedure (TOPO technique), which resulted in high quality nanoparticles with a narrow size distribution and high quantum yield. Figure 2-25 (a) shows the absorbance spectra of 20~30 Å diameter CdS, CdSe and CdTe nanocrystals. All the samples show the effect of quantum confinement, where the

absorbance edges are shifted to shorter wavelength than those of bulk band gaps with 512, 716 and 827 nm, respectively. The evolution of absorbance spectra can be shown in Figure 2-25 (b) with size tuned CdSe nanoparticles.

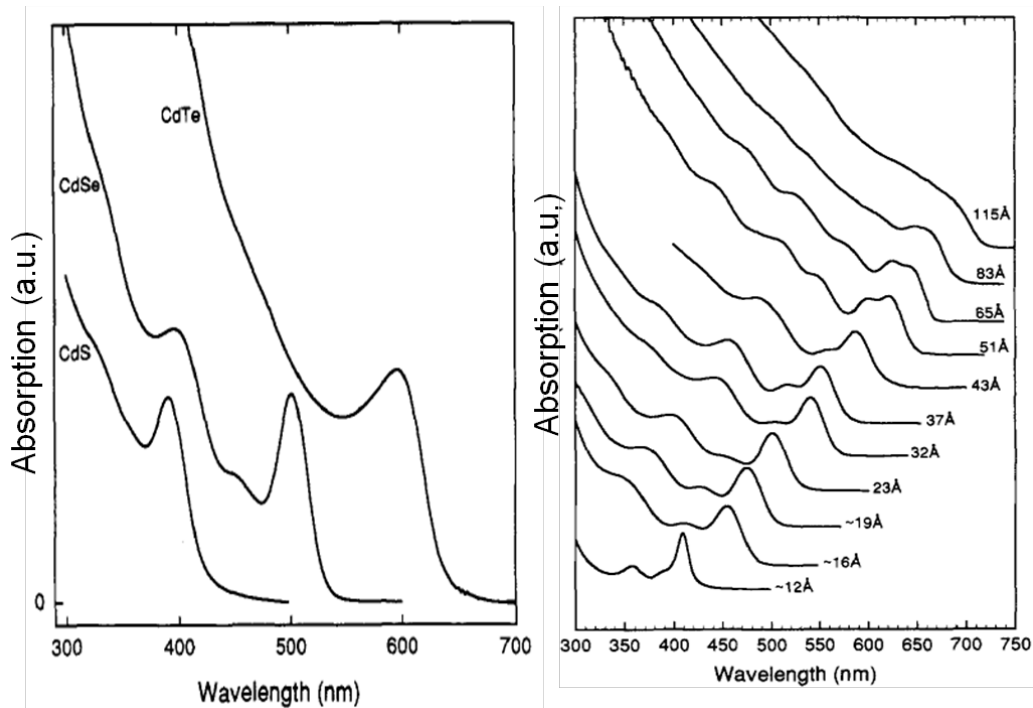


Figure 2-25. Absorbance properties of II-VI semiconductor nanoparticles.

Luminescence caused by intentionally incorporated impurities (activators) is classified as extrinsic luminescence in contrast to intrinsic (band edge) luminescence. When a dopant with quantum states remote from the valence and conduction band edges are added to the semiconductor host, another radiative mechanism is involved. This mechanism results in localized luminescence, not band edge recombinations, since the luminescence excitation and emission processes are confined in a localized luminescence center. These localized transitions are classified as allowed (intershell) or forbidden (intrashell) based on the parity selection rule [82]. Some of examples for allowed transitions include  $s \leftrightarrow p$  and  $f \leftrightarrow d$  transition, while forbidden transitions include  $d \leftrightarrow d$  and  $f \leftrightarrow f$  transitions. ZnS nanoparticles doped with Mn, Tb and Eu have

been reported for the reduction of luminescent decay time [83, 84]. Rare-earth ions doped oxide nanoparticles also have been widely studied. For example,  $\text{Eu}^{3+}$  or  $\text{Nd}^{3+}$  doped  $\text{Gd}_2\text{O}_3$  nanoparticles have been used for cathodoluminescence and laser applications [85, 86].

#### 2.4.2 Surface Modification of Luminescent Nanoparticles

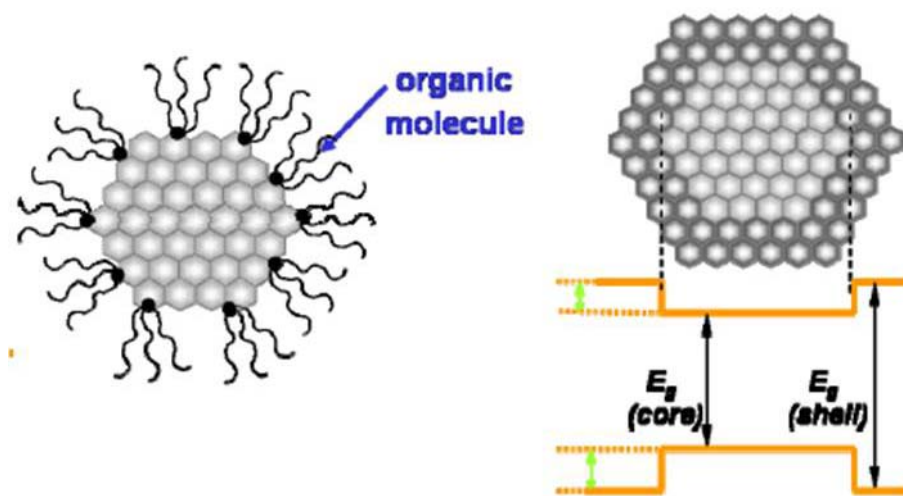


Figure 2-26. Schematic of organic and inorganic passivation.

The electronic and optical properties of all inorganic crystals depend on the three dimensional periodicity of the potential wells that exist in the materials. The discontinuity of periodicity at the surface layer will cause changes to these properties. The lack of atoms on one side of the crystal leads to dangling chemical bonds that generate structural modification such as reconstruction and relaxation [87]. To achieve stable photoluminescence with a higher efficiency, passivation of the surface is crucial and it has been successfully obtained by capping layers on the nanocores, as shown in Figure 2-26 [88].

Coating nanoparticles with higher band gap inorganic materials has been shown to enhance photoluminescent quantum yields by passivating surface non-radiative recombination paths [19, 89-91]. In addition, these core/shell heterostructures are more robust than those passivated organically. Moreover, wider band gap of the surface materials results in the confinement of charge carriers inside the core material.

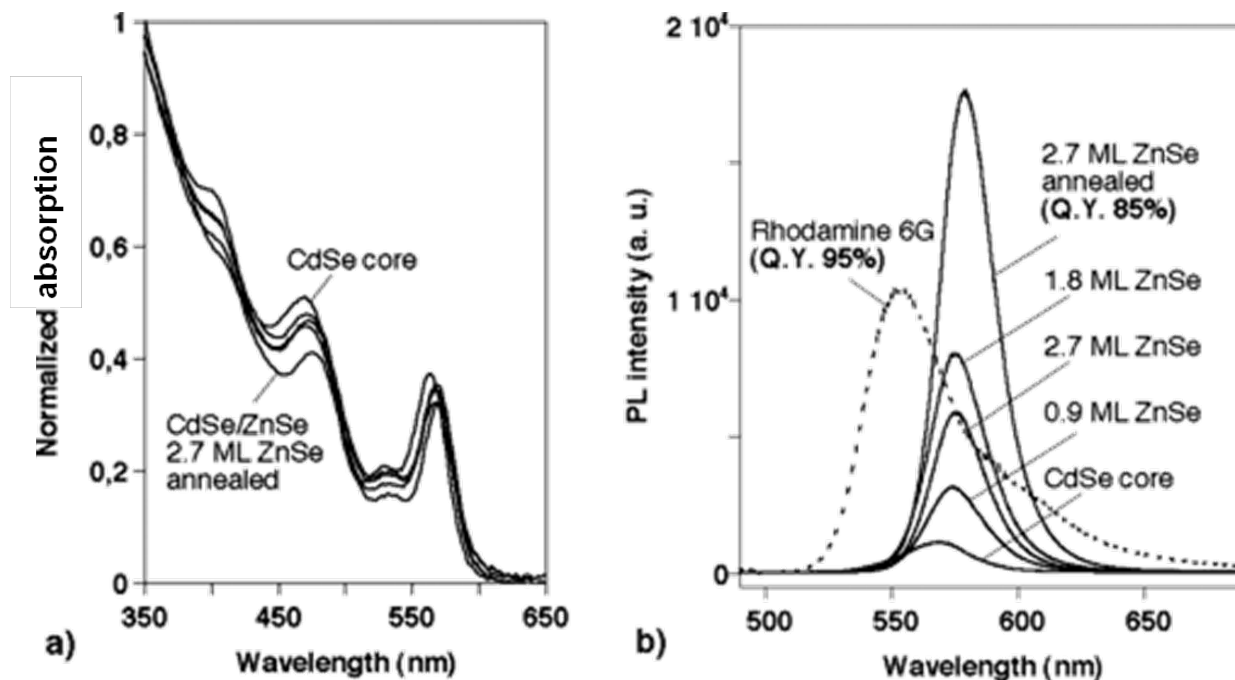


Figure 2-27. The absorption spectra of CdSe/ZnSe nanocrystals during the shell growth.

Some important examples of the core/shell structured nanoparticles include CdSe nanoparticles coated by ZnSe, ZnS or CdS [19, 89, 90, 92, 93]. P. Reiss, et al reported that highly luminescent CdSe/ZnSe core/shell nanoparticles were synthesized [94]. As the shell thickness is getting thicker, the absorption spectrum of CdSe/ZnSe has shifted to the lower energy, which is the result of partial leakage of the excitons into the shell (Figure 2-27(a)). The evolution of the luminescence quantum yield of CdSe/ZnSe core/shell nanoparticles was described in Figure 2-27(b). The luminescent quantum yield of CdSe/ZnSe first rose because of the passivation of the surface defects of

nanocores, then decreased as a result of larger density of structural defects created in the thick shells.

While the surface modification of semiconductor nanocrystals plays a significant role, enhanced photoluminescence has been reported from rare-earth ion doped oxide nanoparticles. For example, some heterostructures based on  $\text{YVO}_4:\text{Eu}^{3+}$  phosphor such as  $\text{YVO}_4:\text{Eu}^{3+}/\text{YBO}_3:\text{Eu}^{3+}$ ,  $\text{Y}_2\text{O}_3:\text{Eu}^{3+}/\text{SiO}_2/\text{YVO}_4:\text{Eu}^{3+}$ ,  $\text{SiO}_2/\text{YVO}_4:\text{Eu}^{3+}$ ,  $\text{Y}(\text{OH})_3-\text{Eu}^{3+}/\text{YVO}_4-\text{Eu}^{3+}$  composite, and  $\text{YV}_{(0.7)}\text{P}_{(0.3)}\text{O}_4:\text{Eu}^{3+},\text{Bi}^{3+}/\text{SiO}_2$  have been proposed [95-99]. Figure 2-28 shows the enhancement of photoluminescence versus shell thickness for  $\text{YVO}_4:\text{Eu}^{3+}/\text{YPO}_4$  heterostructures [100].

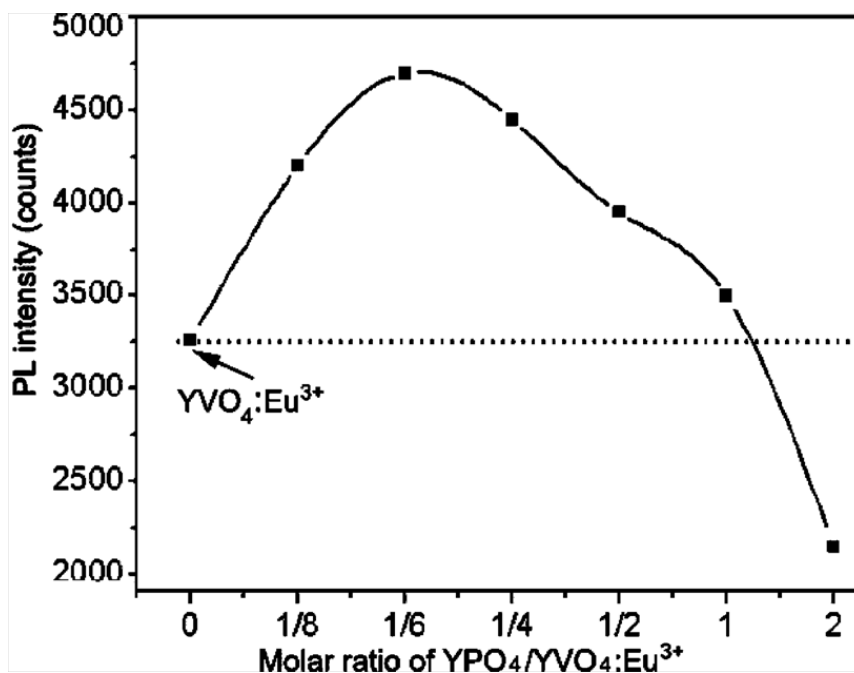


Figure 2-28. Plot of PL intensity of the  $^5\text{D}_0-^7\text{F}_2$  emission at 619 nm versus the  $\text{YPO}_4/\text{YVO}_4:\text{Eu}^{3+}$  molar ratio.

CHAPTER 3  
SHAPE CONTROLLED GADOLINIUM OXIDE DOPED WITH EUROPIUM COLLOIDAL  
NANOCRYSTALS GROWN BY HOT-SOLUTION METHOD

**3.1 Introduction**

Rare-earth doped luminescent nanocrystals are being intensively studied due to their potential applications in displays, lightings and biologic diagnostics [101, 102]. It is well established that the optical, electrical and chemical properties of nanoparticles depend strongly on their shape, morphology and crystal structure [103-105]. Zero- and one-dimensional (1D) nanostructures, such as quantum dots, nano-rods, nano-wires and nano-tubes, have been widely studied [106, 107]. Specific organic surfactants, which can modulate the growth kinetics, have been employed to grow anisotropic luminescent nanostructures using non-hydrolytic procedures with and without templates [108-110]. For example, rare earth doped zero and one dimensional (0D and 1D) structures such as  $\text{LaPO}_4: \text{RE}$  (RE=  $\text{Eu}^{3+}$ ,  $\text{Tb}^{3+}$ ) nanowires,  $\text{Y}_2\text{O}_3: \text{RE}$  nanotubes and  $\text{Gd}_2\text{O}_3: \text{Eu}^{3+}$  nanoplates have been reported [25, 111-114]. Colloidal growth in non-hydrolytic liquid media can give reproducible shapes and sizes of nanoparticles. This synthesis route results in nanoparticles (NPs) with sizes tuned over the 1–10 nm range. These NPs can be dispersed in organic media for numerous potential applications [115, 116].

Rare-earth doped gadolinium oxide ( $\text{Gd}_2\text{O}_3$ ) generally exhibit photoluminescence (PL) with high quantum yields. For example,  $\text{Eu}^{3+}$  doped gadolinium oxide exhibits red luminescence due to the electric dipole  $^5\text{D}_0-^7\text{F}_2$  transitions on the trivalent europium ion ( $\text{Eu}^{3+}$ ,  $4f^6$ ) [47].  $\text{Gd}_2\text{O}_3: \text{Eu}^{3+}$  nanocrystals produced by non-hydrolytic thermal reactions in the presence of organic surfactants exhibit intense luminescence, and is crystalline and mono-dispersed. Furthermore, this synthetic route allows control of the shape of

nanoparticles through the use of processing parameters such as precursor types, precursor concentration, surfactant, solvent and reaction temperature and time [16]. In this chapter, the luminescent properties of  $\text{Gd}_2\text{O}_3:\text{Eu}^{3+}$  will be reported and discussed with respect to the crystal structure, shapes of nanoparticles and the  $\text{Eu}^{3+}$  dopant location in the  $\text{Gd}_2\text{O}_3$  host.

## 3.2 Experimental

### 3.2.1 Materials

The following precursor compounds and solvents were purchased from Aldrich Chemical Co. : Gd(III) acetylacetonate hydrate, Eu(III) acetate hydrate, oleic acid (90% , tech.), Eu(III) acetate hydrate (90% , tech.), oleic acid (90%, tech.), oleyamine (70%), benzyl ether (99%) and 1,2-hexadecanediol (HDD, 97%). All chemicals were used without further purification. Absolute ethanol, benzyl ether and hexane were analytical grade and used as received.

### 3.2.2 $\text{Gd}_2\text{O}_3:\text{Eu}^{3+}$ Nanocrystal Synthesis

In a one-pot hot-solution synthesis method for the growth of  $\text{Gd}_2\text{O}_3:\text{Eu}^{3+}$  nanocrystals, Gd-acetylacetonate (3 mmol) and Eu-acetate (0.6 mmol) were mixed and dehydrated at 120 °C for 6 hours, followed by addition of oleic acid (9 mmol), oleylamine (9 mmol), benzyl ether (15 mmol) and hexadecanediol (3mmol). The precursor solution was transferred and vigorously stirred under UHP  $\text{N}_2$  gas ambient in a three-neck flask surrounded by a heating mantle. The mixture was held at 120 °C for 30 min, resulting in a transparent yellowish solution. In some cases, samples were preheated to 200 °C for 30 min to change the shape of the nanocrystals. After preheating, the temperature was increased to 290~320 °C with a heating rate of 5~25 °C/min, and the steady-state condition was maintained for 30 to 180 min. The color of the mixture changed to deep

brown after 40 min. Aliquots of the solution were extracted at selected intervals to determine the time dependence of growth. After the desired growth times, samples were cooled and dispersed in ethanol. Dispersed NPs were washed and centrifuged several (at least three) time in order to purify the nanoparticles and remove residual surfactants and precursors. Washed  $\text{Gd}_2\text{O}_3:\text{Eu}^{3+}$  nanocrystals were easily re-dispersed in non-polar solvents such as hexane and/or toluene.

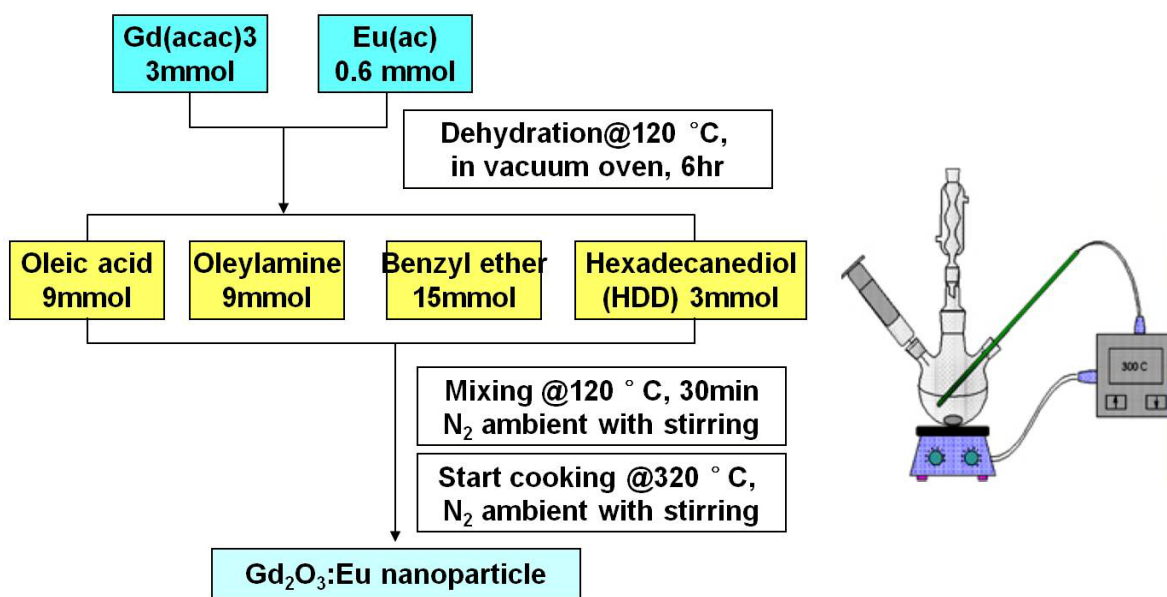


Figure 3-1. Flow chart of non-hydrolytic hot-solution synthesis procedure.

### 3.2.3 Characterization

The crystal structure of as-grown and calcined nanoparticles were characterized by X-ray diffraction (XRD) with a Philips APS 3720 diffractometer using  $\text{Cu K}\alpha$  radiation ( $\lambda=1.54178 \text{ \AA}$ ). The XRD patterns were collected from dried powder samples with a  $0.02^\circ$  step scan mode over a  $2\theta$  range of  $20\sim 70^\circ$ . The morphology and size were determined with a JEOL 2010F high resolution transmission electron microscope (HR-TEM) operated at an accelerating voltage of 200 kV. The TEM samples were prepared

by drop-casting NPs dispersed in hexane onto a carbon coated holey copper grids, followed by drying at room temperature. Photoluminescence (PL) and photoluminescence excitation (PLE) spectra were measured at room temperature using a JASCO FP-6500/6600 research grade fluorescence spectrometer with a 150 W Xenon lamp. The quantum yields were determined by comparing the integrated emission from colloidal NP solutions with those from an ethanol-Rhodamine 6G solution growth the same optical density and excited at the same wavelength of 280 nm. The concentrations of  $\text{Eu}^{3+}$  dopant in as-prepared  $\text{Gd}_2\text{O}_3:\text{Eu}^{3+}$  nanoparticles were measured using an inductively coupled plasma (ICP) spectrometer (Perkin-Elmer Plasma 3200). X-ray luminescence was measured with a 40 kV Bullet<sup>TM</sup> X-ray tube combined with a Ocean Optics USB-2000 miniature fiber optic spectrometer. The distance from the x-ray target to the sample was ~3 cm and the x-ray tube was operated at 100  $\mu\text{A}$ . For each measurement, a crucible with 57  $\text{mm}^2$  area and 2 mm thickness was filled with nanopowder such that each sample had the same area exposed to the x-rays.

### **3.3 Results and Discussion**

#### **3.3.1 Shape Control of $\text{Gd}_2\text{O}_3:\text{Eu}^{3+}$ Nanocrystals**

Three distinct shapes, clover, plate and round, of nanoparticles were observed for the present precursors and one-pot hot-solution method. Typical NPs are shown in the high resolution TEM images of Figure 3-2. The preheat and, reaction times and temperatures, and observed shapes are summarized in Table 1. Figure 3-2(a) shows ~20 nm clover  $\text{Gd}_2\text{O}_3:\text{Eu}^{3+}$  nanoparticles, with each nanoparticle being composed of several petals that self-assembles into the clover NPs, which were grown with a preheating step. Square and round nanoparticles with characteristic dimensions of 10-15 nm are shown in Figure 3-2 (b-d).

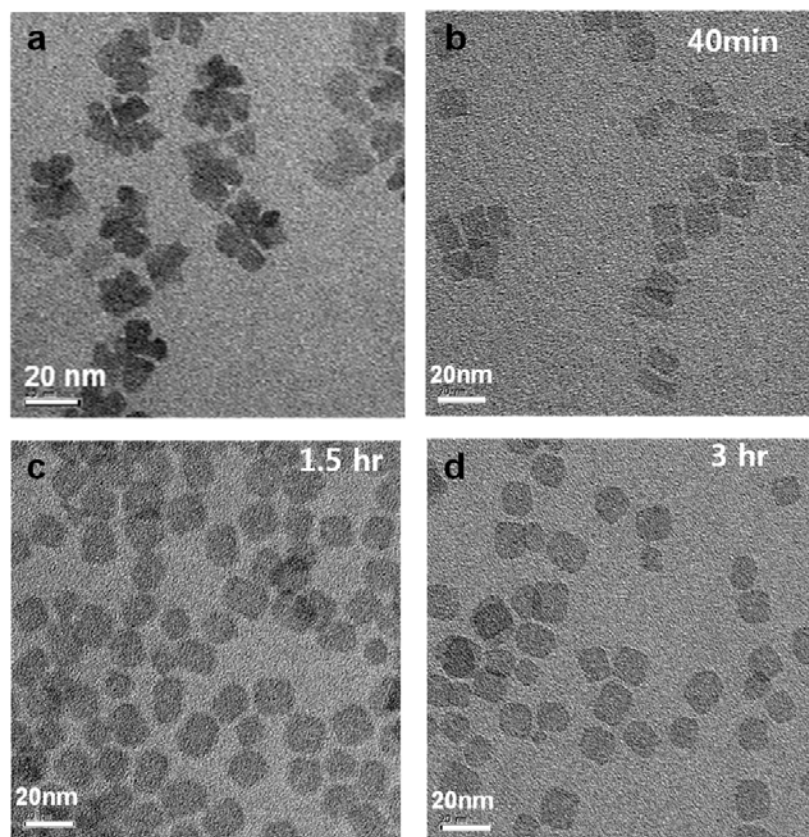


Figure 3-2. TEM images of  $\text{Gd}_2\text{O}_3:\text{Eu}^{3+}$  nanoparticles synthesized with different experimental parameters.

The shape of the nanoparticles was a function of the pre-heat condition, synthesis temperature and reaction time, as shown in Table 1. Clover nanoparticles (sample H1) were produced using pre-heating at 200 °C for 30 min, followed by a 90 minute synthesis at 290 °C, as mentioned before. For synthesis at 320°C without the preheat step, platelet (H2) and round (H3 and H4) nanoparticles were produced. The particle shape can be explained by a LaMer plot which depicts the nanocrystal nucleation and growth versus time [42]. A proposed LaMer plot for  $\text{Gd}_2\text{O}_3:\text{Eu}^{3+}$  nucleation and growth by the hot-solution method is shown in Figure 3-3, and precursor concentration (solid black line) and temperature (solid blue line) are shown versus time.

Table 3-1. Experimental parameters of clover, square and round  $\text{Gd}_2\text{O}_3:\text{Eu}^{3+}$  nanoparticles (H1-H4).

Sample number	Shape	Preheat condition	Synthesis temperature	Reaction time
H1	Clover	200 °C, 30 min	290	90 min
H2	Platelet	No	320	40 min
H3	Round	No	320	90 min
H4	Round	No	320	180 min

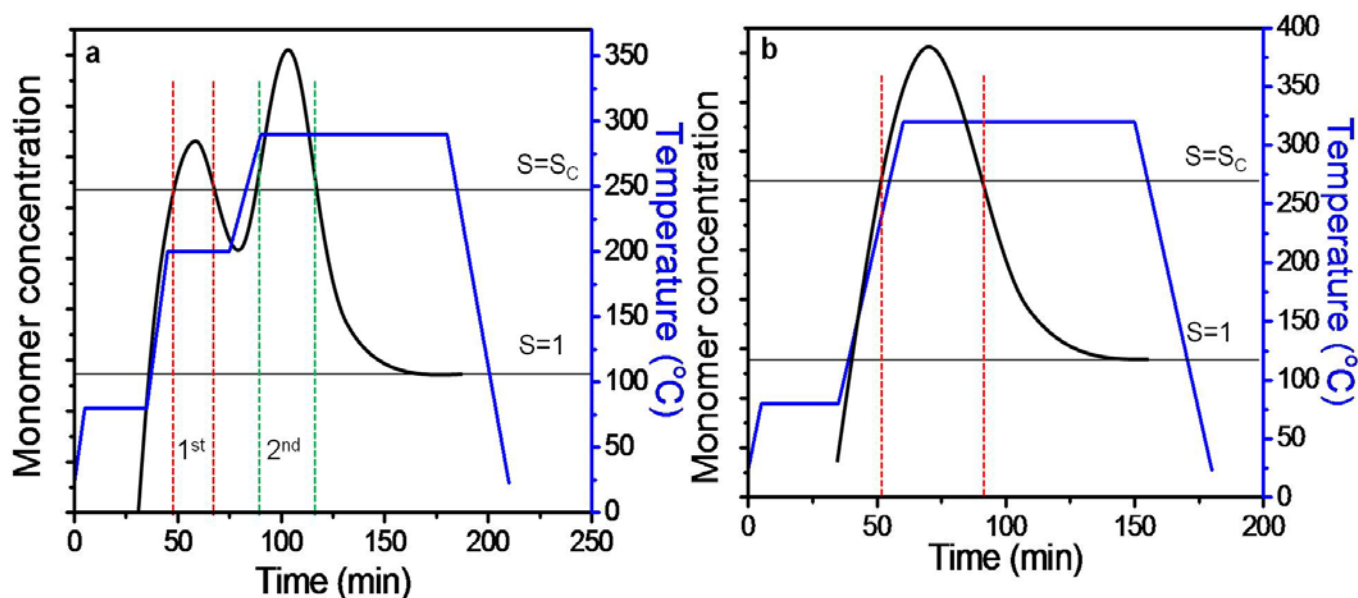


Figure 3-3. Modified LaMer plots with an additional axis of reaction temperature.  $S=S_c$ : Critical saturation of monomer concentration to induce nucleation.  $S=1$ : Equilibrium monomer concentration below which growth stops.

After the solution is mixed at 80 °C for 40 minutes, a pre-heat at 200 °C for 30 min results in the first nucleation stage, as shown in Figure 3-3 (a). Continued reaction at the higher temperature of 290 °C produces secondary nucleation of the clover petals and subsequent growth. The final size is larger due to Oswald ripening effects. To produce platelet and round nanoparticles, the temperature was increased directly from the mixing temperature of 80 °C to the reaction temperature of 320 °C without a preheat step (Figure 3-3b). This procedure would result in a high density of nuclei with simultaneous decrease in monomer concentration to stop nucleation and minimize

growth. While growth was slow, it was sufficient to change the shape of the nanoparticles from platelet to round with increasing reaction, which can be explained by surface tension effects [117]. High growth temperature (320 °C) of  $Gd_2O_3:Eu^{3+}$  nanoparticles allows the morphology to change from initial square shape to round pseudo-sphere nanoparticles which will minimize their surface tension.

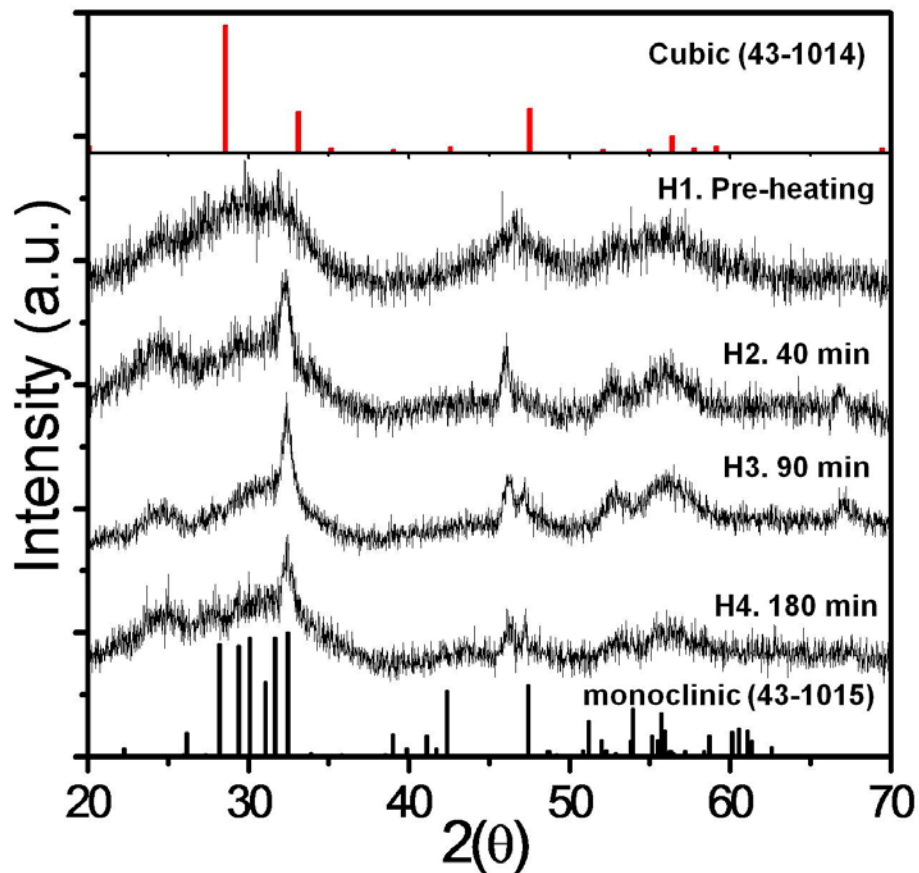


Figure 3-4. XRD patterns of as-synthesized samples.

### 3.3.2 Crystal Structure of $Gd_2O_3:Eu^{3+}$ Nanoparticles

The XRD spectrum from a clover sample (H1) shows very broad peaks which match those from cubic  $Gd_2O_3$  (JCPDS #43-1014) (Figure 3-4). The broad peaks indicate small grain size, presumably due to the size of each petal of the  $Gd_2O_3:Eu^{3+}$  nanoparticles. The XRD spectra of platelet (H2) and for round (H3 and 4) samples

consisted of much sharper peaks, but they indicate the presence of both a monoclinic (JCPDS #43-1015) and a cubic  $Gd_2O_3$  phase. A phase transformation from cubic to monoclinic  $Gd_2O_3$  has been reported at temperatures above 1300–1400 °C, with the stable high temperature phase being monoclinic [118]. Apparently the monoclinic phase is stabilized in nanometer particles, as suggested by the strength of the main monoclinic XRD peak ( $2\theta \approx 32.47^\circ$ ) versus that from cubic  $Gd_2O_3$  ( $2\theta \approx 27^\circ$ ). The data suggest all three samples, H2 to H4, have mixed crystal structures, which is consistent with earlier reports of mixed structures for rare-earth oxide nanoparticles [25, 119]. In addition, interestingly, it is possible to detect a small shift of XRD peaks for low angle  $2\theta$  and a peak separation at  $2\theta = 47^\circ$  for H2, H3 and H4 samples. It seems to be a change of microstructures for increasing reaction time.

### 3.3.3 Photoluminescent Properties of Nanoparticles

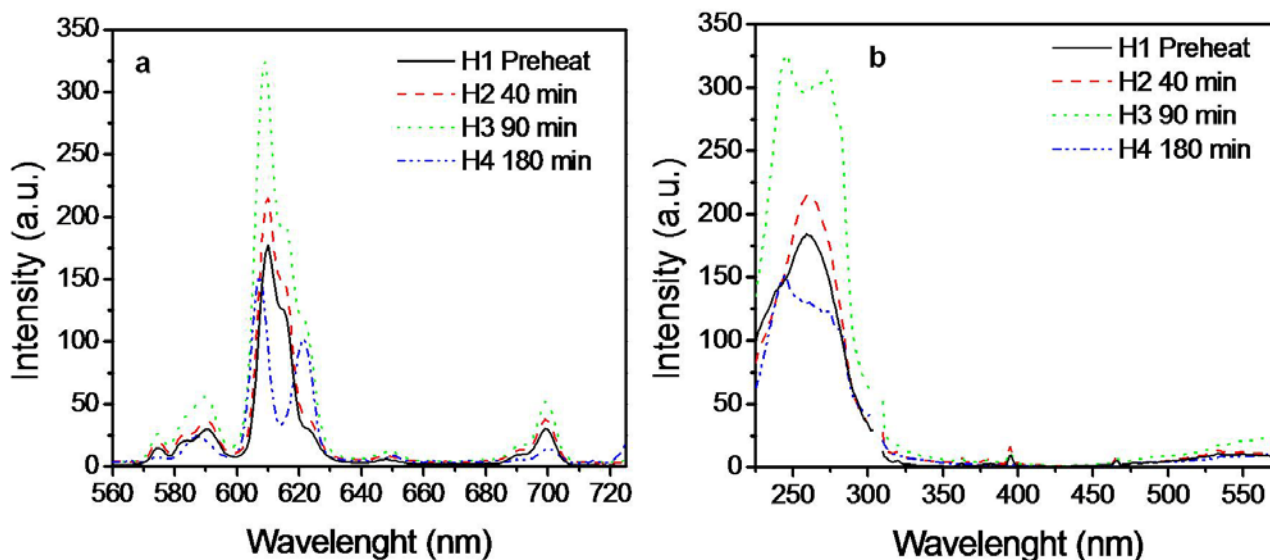


Figure 3-5. PL and PLE spectra of  $Gd_2O_3:Eu^{3+}$  nanoparticles. The PL spectra of excitation at 250 nm and the PLE spectra for the emission at 609 nm.

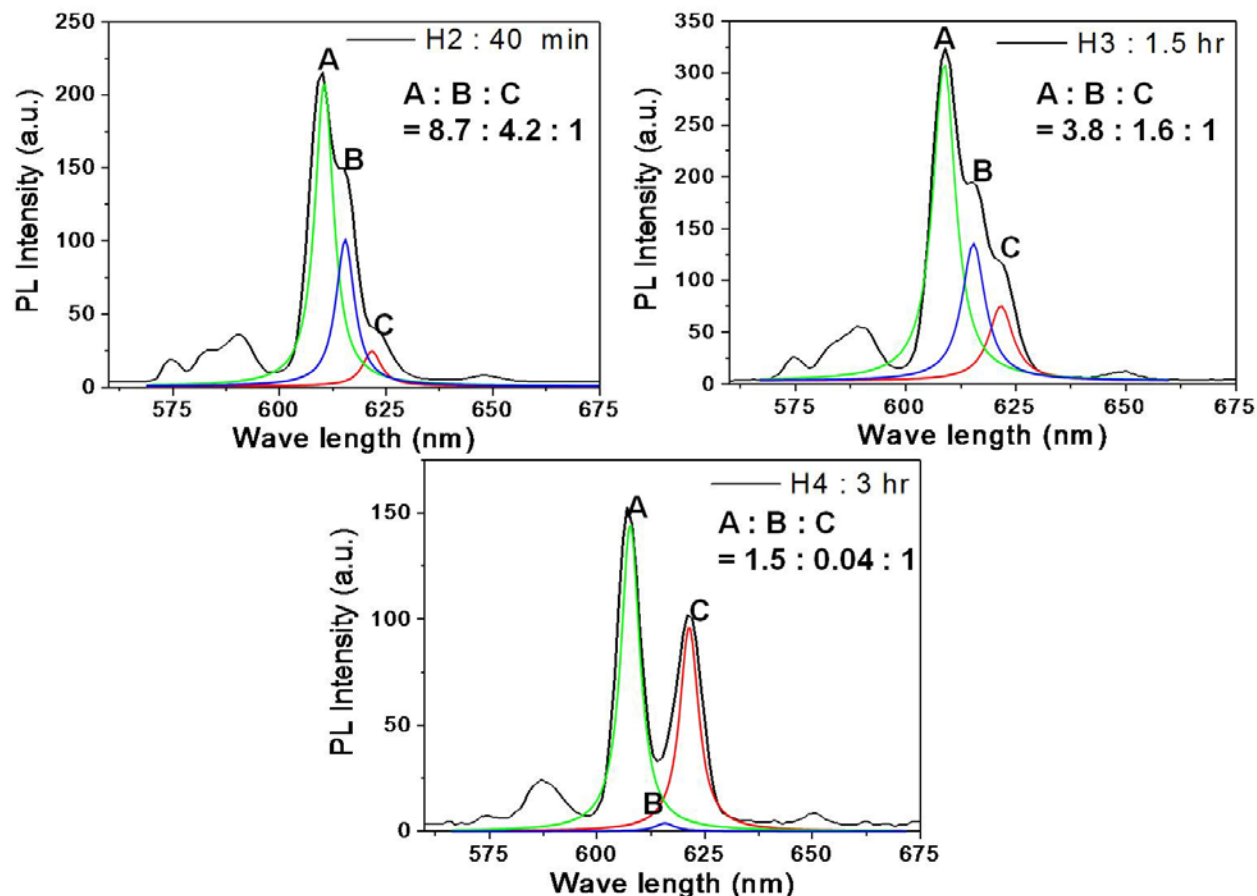


Figure 3-6. Resolved PL spectra of square nanoparticles with reaction time of 40 min (H2), round nanoparticles with reaction time for 90 min (H3) and for 180 min (H4).

Photoluminescence emission (PL) and photoluminescence excitation (PLE) spectra of  $\text{Gd}_2\text{O}_3:\text{Eu}^{3+}$  nanoparticles are shown in Figure 3-5. The PLE spectra for the emission at 609 nm from  $\text{Gd}_2\text{O}_3:\text{Eu}^{3+}$  nanoparticles with different shapes are composed of a broad excitation band extended from 225 ~ 300 nm, which is considered to be both host and charge-transfer band (CTB) excitation .

The broad excitation peak can be divided into three different regions, consisting of the cubic host's absorption (~244 nm), the charge-transfer band (CTB) excitation of Eu-O (~260 nm), and  $\text{Gd}^{3+}$  ion direct absorption (~275 nm). A charge transfer between Eu and O results from an electron transferring from the 2p orbital of  $\text{O}^{2-}$  to the 4f orbital of

$\text{Eu}^{3+}$ . The strength of the charge transfer is related to the covalency of the  $\text{O}^{2-} - \text{Eu}^{3+}$  bond and the coordination of the  $\text{Eu}^{3+}$  and  $\text{Gd}^{3+}$  ions [120]. The small, sharp peaks between 360 and 530 nm and Figure 3-5b are from direct excitation of the f–f shell transitions on  $\text{Eu}^{3+}$  ions [121]. As discussed above, PL excitation spectra of  $\text{Gd}_2\text{O}_3:\text{Eu}^{3+}$  nanoparticles have three different components, such as host absorption, CTB and  $\text{Gd}^{3+}$  direct absorption, so that it is possible to decompose the broad PL excitation peak from 225 to 300 nm into three Lorentzian curves. Their different ratio show that H3 and H4 exhibit higher host and  $\text{Gd}^{3+}$  absorption whereas H1 and H2 has a dominant CTB excitation [122, 123].

Growth at low temperature for short reaction times presumably result in more defected crystalline and low host and  $\text{Gd}^{3+}$  absorption. The PL emission spectra from  $\text{Gd}_2\text{O}_3:\text{Eu}^{3+}$  nanoparticles with various shapes is dominated by the  ${}^5\text{D}_0\text{-}{}^7\text{F}_2$  transition at 609 nm with minor peaks from  ${}^5\text{D}_0\text{-}{}^7\text{F}_J$  ( $J = 0, 1, 3$  and  $4$ ) transitions, which is a characteristic of the  $\text{Gd}_2\text{O}_3$  host lattice [47]. It was previously reported that several split levels give rise to several PL peaks between 600 and 630 nm in monoclinic  $\text{Gd}_2\text{O}_3:\text{Eu}^{3+}$ , while the  ${}^5\text{D}_0\text{-}{}^7\text{F}_2$  peak at 610 nm is dominant from cubic  $\text{Gd}_2\text{O}_3$  [124, 125]. As shown in Figure 3-6, the PL spectra between 600-625 nm from  $\text{Gd}_2\text{O}_3:\text{Eu}^{3+}$  nanoparticles without pre-heating (H2, H3 and H4) can be resolved into three different peaks (A, B and C, centered at 610, 615 and 621 nm), where A is from the cubic phase (610 nm), and B and C are from the monoclinic phase (615 and 621 nm). The ratio of the three peak intensities normalized to the intensity of peak C is shown in Figure 3-6. The photoluminescence properties is dependent on the structure of host material [47]. Generally, cubic  $\text{Gd}_2\text{O}_3:\text{Eu}^{3+}$  exhibits brighter luminescence than does monoclinic

Gd<sub>2</sub>O<sub>3</sub> [50]. However, in nanoparticles regime, it is not easy to correlate the shape of PL spectra with crystal structures due to complicated and similar structures of nanoparticles based on XRD spectra, as described above. In other words, the crystallinity cannot be the only factor to determine the luminescent efficiency for nanoparticles.

Table 3-2. The quantum yield and molar concentration of Eu ions for clover, square and round Gd<sub>2</sub>O<sub>3</sub>:Eu<sup>3+</sup> nanoparticles (H1-H4).

Sample number	H1	H2	H3	H4
Shape	Clover	Platelet	Round	Round
Original Eu molar concentration (%)	16.7	16.7	16.7	16.7
ICP measured concentration (%)	15.0	15.2	15.1	15.2
Quantum Yield (%)	24	48	67	9

The quantum yields (QY) and Eu<sup>3+</sup> doping concentrations (molar %) from H1-H4 nanoparticles are reported in Table 3-2. Even though the concentration of Eu<sup>3+</sup> dopant was constant, the quantum yield varied by more than a factor of seven between H1 to H4, with H4 having the lowest and H3 having the highest quantum yield. Possible reasons for the different QYs from Gd<sub>2</sub>O<sub>3</sub>:Eu<sup>3+</sup> nanoparticles include changes in the dopant concentration and/or location, and differences in the host environment and dopant location. Sometimes the real doping concentration is different from the precursor concentration. However, the inductively coupled plasma (ICP) data show that the Eu doping concentration in Gd<sub>2</sub>O<sub>3</sub>:Eu<sup>3+</sup> nanoparticles is constant within experimental error and is independent of particle shape. XRD data suggest that the lower QY of H1 (QY = 24%) as compared to H2 and H3 (QY = 48 and 67%, respectively) may be explained by defective crystalline of H1 due to its small size and low reaction temperature. However the difference in QYs of H2, H3 and H4 cannot be so easily explained. A similar variation of QY has been reported for ZnGa<sub>2</sub>O<sub>4</sub>:Eu, where a low quantum yield resulted

from migration of Eu ions to the surface of nanoparticles. In our work, nanoparticles have high doping concentration with over 15 %. Assuming that Eu activators can diffuse out and accumulate in the surface region, the local environment of  $\text{Gd}_2\text{O}_3:\text{Eu}^{3+}$  nanoparticles will be changed due to different atomic size between Eu and Gd, which will be discussed below.

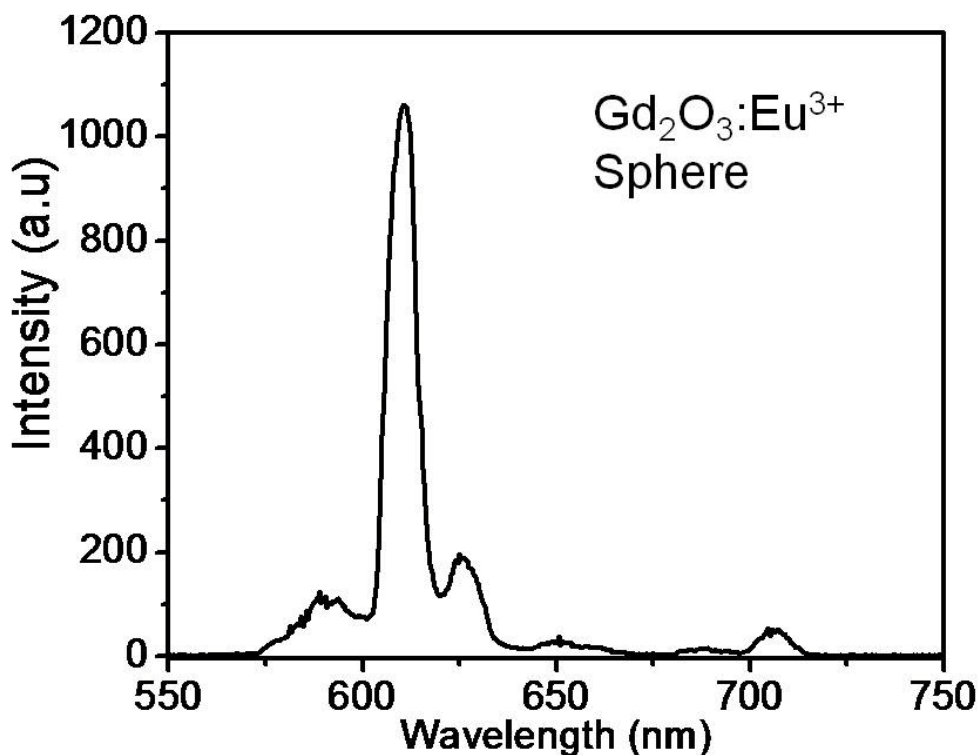


Figure 3-7. X-ray luminescence spectrum of as-prepared sphere-like  $\text{Gd}_2\text{O}_3:\text{Eu}^{3+}$  nanocrystals

### 3.3.4 X-ray Luminescence Properties of Nanoparticles

Figure 3-7 shows the X-ray luminescence (XL) spectrum of as-synthesized spherical  $\text{Gd}_2\text{O}_3:\text{Eu}^{3+}$  nanoparticles (H3) irradiated by 40 kV X-ray. The spectrum shows a dominating peak at 612 nm from the  $^5\text{D}_0 \rightarrow ^7\text{F}_2$  transition which is similar to the photoluminescence spectrum shown in Figure 3-5(a). Several X-ray and radio-luminescence materials have been already developed, such as NaI, but may have

undesirable properties, such as poor high temperature drift effects. In this study, X-ray luminescence was observed from  $\text{Gd}_2\text{O}_3:\text{Eu}^{3+}$  nanoparticles synthesized by non-hydrolytic hot-solution synthesis method, consistent with its potential application as scintillation detectors.

### 3.4 Conclusion

$\text{Eu}^{3+}$  doped  $\text{Gd}_2\text{O}_3$  nanoparticles were synthesized by a hot-solution method. The shape of  $\text{Gd}_2\text{O}_3:\text{Eu}^{3+}$  nanoparticles that were preheated and then reacted  $290^\circ\text{C}$  was “clover”. Without the preheat step and for reaction at  $320^\circ\text{C}$ , short times produced platelet nanoparticles, but became more circular at longer reaction times. Potential mechanisms leading to various shapes of  $\text{Gd}_2\text{O}_3:\text{Eu}^{3+}$  nanoparticles were discussed. By controlling reaction parameters, the quantum yield of  $\text{Gd}_2\text{O}_3:\text{Eu}^{3+}$  nanoparticles also varied from 9 % to 67 %. Clover and plate  $\text{Gd}_2\text{O}_3:\text{Eu}^{3+}$  nanoparticles exhibited relatively low quantum yield, 24% and 48%, respectively, because of the defective crystalline. Round  $\text{Gd}_2\text{O}_3:\text{Eu}^{3+}$  nanoparticles with 1.5 hrs reaction time showed the highest quantum yield of 67 %, which results from the combination of two factors, a host environment and a dopant location. For  $\text{Eu}^{3+}$  doped nanoparticles with a prolonged reaction time with 3 hrs, the quantum yield decreased to 9% presumably due to the migration of dopant ions and subsequent segregation to the nanoparticle surface region.

## CHAPTER 4 ENHANCED PHOTOLUMINESCENCE FROM GADOLINIUM OXIDE DOPED WITH EUROPIUM NANOCORES WITH YTTRIUM OXIDE THIN SHELL

### 4.1 Introduction

Oxide and sulphide nanophosphors are popular research topics due to their unique physical properties. The size, shape, structure and composition of nanoparticles can be controlled so that their optical, electrical or mechanical properties can be tuned to desired values [76, 126]. For example, oxide nanophosphors, such as  $Y_2O_3$ ,  $GdVO_4$  and  $Gd_2O_3$  doped with rare earth ions have been studied for plasma display panels (PDPs), cathode ray tubes (CRTs) and field emission displays (FEDs) [127-129]. Europium doped  $Gd_2O_3$  exhibits red luminescence from the electric dipole  $^5D_0-^7F_2$  transitions on the trivalent europium ions ( $Eu^{3+} 4f^6$ ) [47].  $Gd_2O_3:Eu^{3+}$  nanoparticles synthesized by hydrothermal or nonhydrolytic thermal reactions with organic surfactants exhibit excellent crystallinity and good photoluminescence (PL) efficiency (QY = ~50%) [25]. Moreover, the rate of growth and the shape of nanoparticles can be controlled by the type and concentration of precursors and organic surfactants [25, 130]. However, it is well known that states at the surface of phosphor powders can lead to non-radiative relaxation and low luminescent efficiencies [87], especially for nanophosphors with a large surface to volume ratio. Capping of the nanoparticles core with the proper shell materials could passivate surface defects and eliminate the non-radiative pathways [131]. This strategy has been successfully used in core/shell nanoparticles such as CdSe/ZnS and CdS/ZnS, as well as oxide nanoparticles like  $SiO_2/Gd_2O_3:Eu^{3+}$  [132-134].

The precipitation of nanoparticles in a high boiling-point alcohol, generally called the polyol synthesis method, has been used to produce various materials including elemental metals and oxides [135, 136]. Recently, Wang, et al reported the synthesis of

CeF<sub>3</sub> core/shell nanoparticles using the polyol method [137]. In this study, the polyol method was used to synthesize Gd<sub>2</sub>O<sub>3</sub>:Eu<sup>3+</sup> cores followed by nucleation and growth of Y<sub>2</sub>O<sub>3</sub>. It will be shown that only a fraction of the Y<sub>2</sub>O<sub>3</sub> grew as a shell on the Gd<sub>2</sub>O<sub>3</sub>:Eu<sup>3+</sup> cores, but the shell did increase the PL intensity. The consequences of growth of yttria both as a shell and as a separate phase on the properties of the nanophosphor were investigated.

## 4.2 Experimental

The following precursor compounds and solvents were purchased from Aldrich Chemical Co. : Gd(III) nitrate hydrate (99.9%), Eu(III) nitrate hexahydrate (99.9%), Y(III) nitrate (99.9%), and ethylene glycol (99%). All chemicals were analytical grade and were used without further purification.

### 4.2.1 Synthesis of Gd<sub>2</sub>O<sub>3</sub>:Eu<sup>3+</sup> Nanocores

The doping concentration of Eu<sup>3+</sup> in the Gd<sub>2</sub>O<sub>3</sub> host was 5 mol% based on precursor concentrations. For synthesis, 1.9mmol of Gd(NO<sub>3</sub>)<sub>3</sub>·6H<sub>2</sub>O and 0.1 mmol Eu(NO<sub>3</sub>)<sub>3</sub>·6H<sub>2</sub>O were dissolved in 25ml of ethylene glycol (EG) in a stirred round-bottomed flask at 100 °C. The clear solution was then heated to 180 °C for 1hr with vigorous stirring. The resulting suspension was cooled to room temperature, diluted with ethanol and the nanoparticles separated by centrifugation at 7000 rpm. To remove unreacted precursor and EG, the nanoparticles were redispersed in ethanol and centrifuged at least three times. The nanoparticles were calcined at 600 °C for 2 h in air.

### 4.2.2 Synthesis of Y<sub>2</sub>O<sub>3</sub> in the Presence of Gd<sub>2</sub>O<sub>3</sub>:Eu<sup>3+</sup> Nanocores

Growth of Gd<sub>1.9</sub>O<sub>3</sub>:Eu<sub>0.1</sub><sup>3+</sup>/Y<sub>2</sub>O<sub>3</sub> core/shell nanoparticles was attempted with a two-step process. First, Gd<sub>2</sub>O<sub>3</sub>:Eu<sup>3+</sup> core nanoparticles were prepared using the procedure described above, then washed with ethanol at least three times. The quantity of Y<sub>2</sub>O<sub>3</sub>,

and therefore the shell thicknesses, was varied in the second step by changing the precursor molar ratio, R, of  $Y(NO_3)_3 \cdot 6H_2O$  to  $(Gd+Eu)(NO_3)_3 \cdot 6H_2O$  from R=1:16 to 1:8, 1:4 and 1:1. As an example, for R = 1:1,  $Gd_2O_3:Eu^{3+}$  nanocores were obtained from 2mmol of  $(Gd+Eu)(NO_3)_3 \cdot 6H_2O$  in a first step, then 2 mmol of  $Y(NO_3)_3 \cdot 6H_2O$  were added to 25 mL of EG at 100 °C and  $Y_2O_3$  was grown in a second step. This solution was heated to 180 °C for 2h with vigorous stirring, cooled to room temperature, washed and centrifuged as discussed above.

#### 4.2.3 Characterization of Nanoparticles

The crystal structure of as-grown and calcined nanoparticles were characterized by X-ray diffraction (XRD) with a Philips APS 3720 diffractometer using Cu K $\alpha$  radiation ( $\lambda=1.54178 \text{ \AA}$ ). The XRD patterns were collected from dried powder samples with a 0.02° step scan mode over a  $2\theta$  range of 20~70°. Morphology and size of nanoparticles were obtained by using a JEOL 2010F high resolution transmission electron microscope (HR-TEM) operated at an accelerating voltage of 200 kV. Specimens for the TEM were prepared by drop-casting particles dispersed in ethanol onto holey carbon-coated copper grids.

X-ray photoelectron spectroscopy (XPS) was used to analyze the nanoparticle's shell thickness with a Perkin-Elmer PHI 5100 ESCA system and Al K $\alpha$  X-rays ( $E=1.486\text{keV}$ ). All the XPS peaks were referenced to the C1s peak at 284.6 eV. To make XPS samples, the same weight of nanoparticles were dispersed in ethanol and 50 $\mu\text{l}$  of solution was drop-cast onto 1 $\text{cm}^2$  Si wafers. Photoluminescence (PL) and photoluminescence excitation (PLE) spectra and luminescent relaxation lifetimes were measured at room temperature using a JASCO FP-6500/6600 research grade fluorescence spectrometer with a 150 W Xenon lamp using films on quartz slides drop

cast from a mixture of 20 mg of nanoparticles in 500  $\mu\text{L}$  of a 4 % solution of poly(methyl methacrylate) (PMMA) dispersed in chlorobenzene. The drop cast films were dried in laboratory air at 80  $^{\circ}\text{C}$  for 12 h.

### 4.3 Results and Discussion

#### 4.3.1 Crystal Structures and Morphologies of Core and Core/Shell Nanoparticles

As-grown nanoparticles were amorphous, but XRD spectra in Figure 4-1 for (a)  $\text{Gd}_2\text{O}_3:\text{Eu}^{3+}$ , (b, c)  $\text{Gd}_2\text{O}_3:\text{Eu}^{3+}/\text{Y}_2\text{O}_3$  core/shell ( $R=1:4$  and  $1:1$ , respectively), and (d)  $\text{Y}_2\text{O}_3$  calcined nanoparticles show crystalline peaks that match with (e) JCPDS data for cubic  $\text{Gd}_2\text{O}_3$  (Card 43-1014) or cubic  $\text{Y}_2\text{O}_3$  (Card 43-1036).

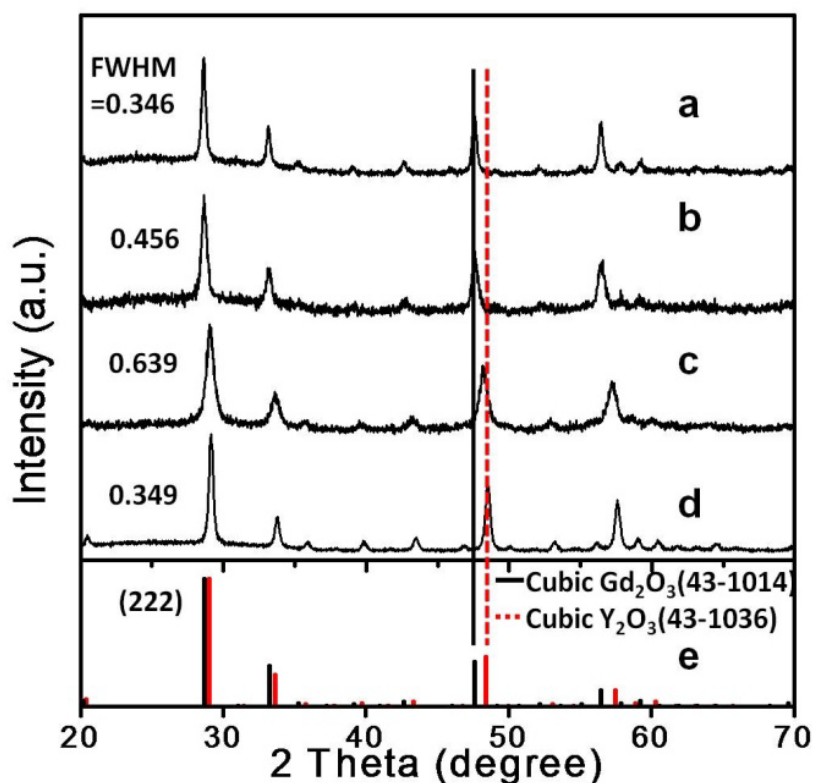


Figure 4-1. XRD patterns of calcined samples:  $\text{Gd}_2\text{O}_3:\text{Eu}^{3+}$  nanocores;  $\text{Gd}_2\text{O}_3:\text{Eu}^{3+}/\text{Y}_2\text{O}_3$  core/shell nanoparticles with the shell grown with a Y to Gd+Eu precursor ratio  $R = 1:4$  and  $1:1$  and pure  $\text{Y}_2\text{O}_3$  nanoparticles.

Since the cubic phases of  $\text{Gd}_2\text{O}_3$  and  $\text{Y}_2\text{O}_3$  differ only by the lattice parameter (0.106 nm for  $\text{Y}_2\text{O}_3$  versus 0.108 nm for  $\text{Gd}_2\text{O}_3$ ), it is difficult to verify by XRD the presence of small amounts of  $\text{Y}_2\text{O}_3$  when  $\text{Gd}_2\text{O}_3$  is also present, and vice versa. For example, for  $\text{Gd}_2\text{O}_3:\text{Eu}^{3+}$  and  $\text{Y}_2\text{O}_3$  nanoparticles grown with a R of 1:1 (Figure 4-1c), the diffraction peaks are shifted to a  $2\theta$  larger than for pure  $\text{Gd}_2\text{O}_3$  and smaller than for pure  $\text{Y}_2\text{O}_3$ , presumably due to overlapping peaks from the presence of both oxides.

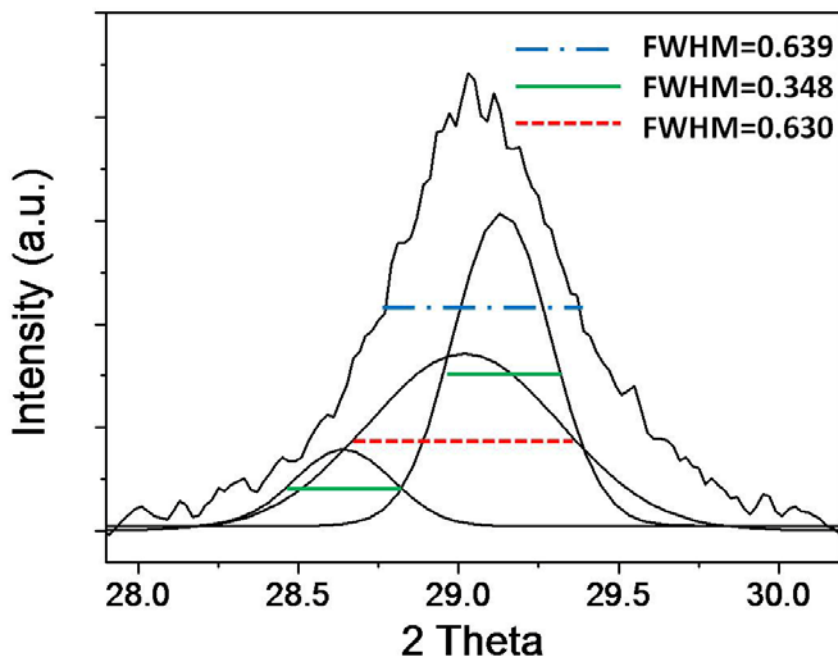


Figure 4-2. Resolved XRD peak of  $\text{Gd}_2\text{O}_3:\text{Eu}^{3+}/\text{Y}_2\text{O}_3$  core/shell nanoparticles with shell grown with a Y to Gd+Eu precursor ratio R =1:1

The broad XRD peak at  $\sim 29.0^\circ$  from the R=1:1 sample was resolved into three different peaks in Figure 4-2. The sharp peaks at  $2\theta$ 's of  $\sim 28.6^\circ$  and  $\sim 29.2^\circ$  correspond to  $\text{Gd}_2\text{O}_3$  cores and phase-separated  $\text{Y}_2\text{O}_3$ . The broad peak at  $\sim 29.0^\circ$  is assigned to  $\text{Y}_2\text{O}_3$  in the shell with a shifted  $2\theta$  due to strain from epitaxy. Cao, et al reported that the diffraction peaks shift to higher  $2\theta$  angles because of the strain from epitaxial growth of an InP shell on an InAs core [138]. In the present case where the shell of  $\text{Y}_2\text{O}_3$  is very thin (see below), the shift in the diffraction peak is consistent with the presence of

nanoparticles of both  $\text{Gd}_2\text{O}_3:\text{Eu}^{3+}/\text{Y}_2\text{O}_3$  core/shell and undoped  $\text{Y}_2\text{O}_3$  nanoparticles for  $R = 1:1$ . Using the Scherrer equation, broadening of the (222) peak indicated an average diameter of 18~20 nm for the  $\text{Gd}_2\text{O}_3:\text{Eu}^{3+}$  and  $\text{Y}_2\text{O}_3$  nanoparticles, consistent with TEM data (see below). As mentioned before, the presence of a mixture of core shell and undoped yttria nanoparticles is consistent with the fact that the diffraction peak full width half maximum (FWHM) was larger for nanoparticles grown with  $R=1:4$  or  $1:1$  as compared to  $R=1:16$ , even though TEM data showed that the average nanoparticle size was constant to within experimental error.

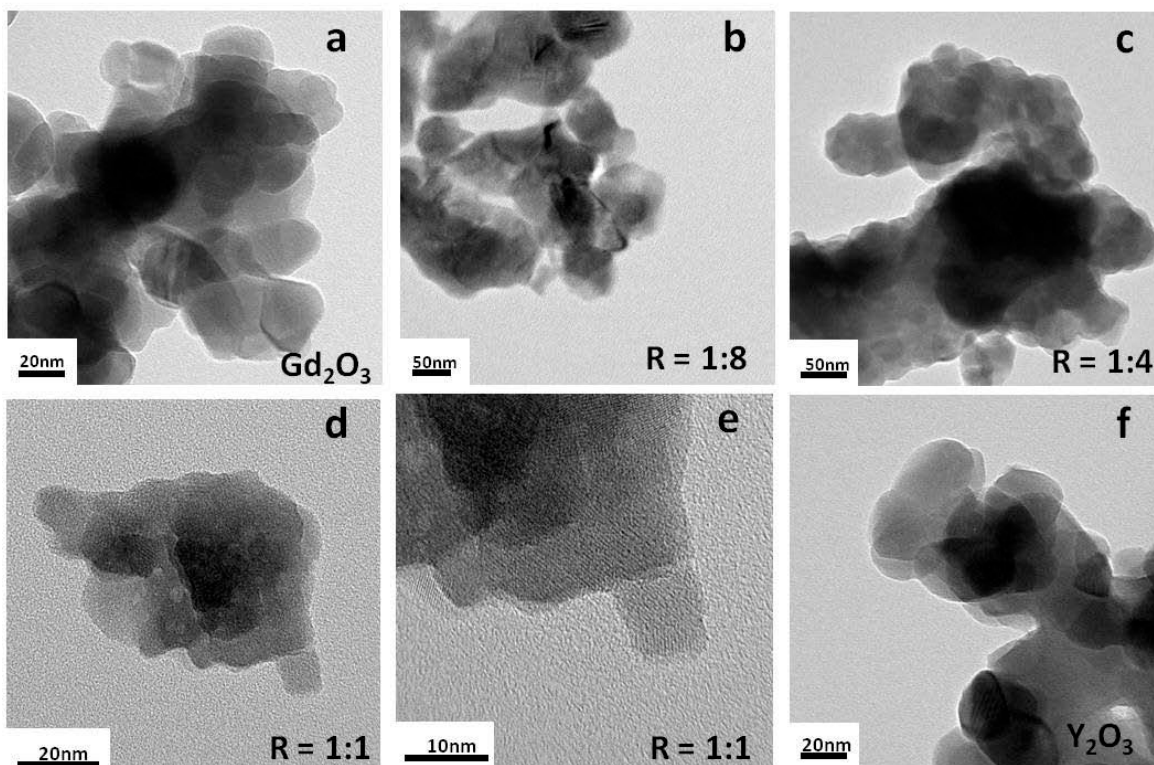


Figure 4-3. TEM images of  $\text{Gd}_2\text{O}_3:\text{Eu}^{3+}, \text{Y}_2\text{O}_3$  and  $\text{Gd}_2\text{O}_3:\text{Eu}^{3+}/\text{Y}_2\text{O}_3$  core/shell nanoparticles:  $\text{Gd}_2\text{O}_3:\text{Eu}^{3+}$  core,  $\text{Gd}_2\text{O}_3:\text{Eu}^{3+}/\text{Y}_2\text{O}_3$  ( $R=1:8$ ),  $\text{Gd}_2\text{O}_3:\text{Eu}^{3+}/\text{Y}_2\text{O}_3$  ( $R=1:4$ ),  $\text{Gd}_2\text{O}_3:\text{Eu}^{3+}/\text{Y}_2\text{O}_3$  ( $R=1:1$ ), High resolution of  $\text{Gd}_2\text{O}_3:\text{Eu}^{3+}/\text{Y}_2\text{O}_3$  ( $R=1:1$ ), and  $\text{Y}_2\text{O}_3$ .

Figure 4-3 shows HR-TEM images of calcined (a) pure  $\text{Gd}_2\text{O}_3$ , (b, c, d and e)  $\text{Gd}_2\text{O}_3:\text{Eu}^{3+}$  and  $\text{Y}_2\text{O}_3$  mixtures grown with  $R = 1:8, 1:4, 1:1$  and  $1:1$ , respectively (note

the different magnification markers), and (f) pure  $Y_2O_3$  nanoparticles. These images show that the particles are slightly agglomerated after calcination. The morphologies of  $Gd_2O_3:Eu^{3+}$  and  $Y_2O_3$  nanoparticles are quite similar, and the average size of all nanoparticles is constant at  $\sim 21 \pm 2$  nm, which is in reasonable agreement with the 18–20 nm size from XRD reported above. With higher magnification, it is possible to see lattice fringes (Figure 4-3e) which indicate good crystallinity after calcining, again consistent with XRD data. In TEM images, contrast is dependent upon the electron scattering power of the material which increases with the average atomic number,  $Z$  [19]. In principle, it should be possible to distinguish between the low  $Z$  (lighter)  $Y_2O_3$  shell and the high  $Z$  (darker)  $Gd_2O_3:Eu^{3+}$  core in Figure 4-3b-e. There are regions in the images that are consistent with the presence of a shell, but agglomeration and overlapping particles make it impossible to establish that the shell is present and to determine the shell thickness and uniformity.

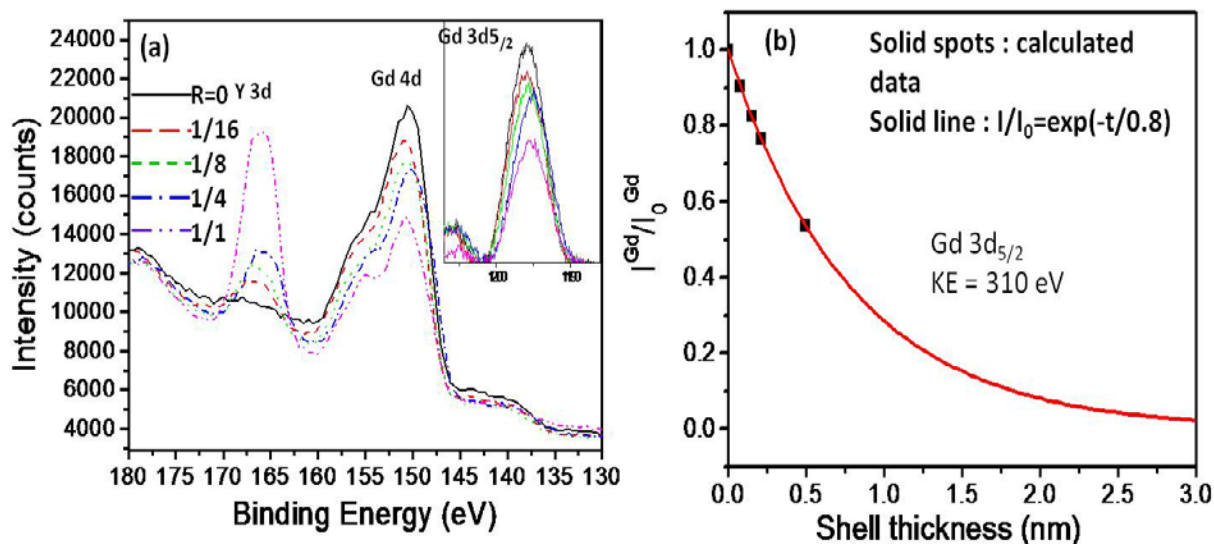


Figure 4-4. XPS peaks from  $Gd_2O_3:Eu^{3+}$  and  $Gd_2O_3:Eu^{3+}/Y_2O_3$  core/shell nanoparticles grown with different precursor molar ratios ( $R$ ) and normalized intensity of the Gd 3d<sub>5/2</sub> peak versus  $Y_2O_3$  shell thickness.

### 4.3.2 Determination of Shell Thickness by XPS Analysis

X-ray Photoelectron Spectroscopy (XPS) analysis can be used to show that  $\text{Y}_2\text{O}_3$  was present both as a coprecipitated phase and as a shell. Growth of a  $\text{Y}_2\text{O}_3$  shell on a  $\text{Gd}_2\text{O}_3:\text{Eu}^{3+}$  core is indicated by an exponential attenuation of the intensity of the gadolinium core photoelectron peaks. The exponential decrease of the gadolinium peak intensities should be complemented by an exponential increase of the intensities of the yttrium photoelectron peaks if  $\text{Y}_2\text{O}_3$  only grows as a shell on the  $\text{Gd}_2\text{O}_3:\text{Eu}^{3+}$  core. If instead,  $\text{Y}_2\text{O}_3$  is present as a co-precipitate with  $\text{Gd}_2\text{O}_3:\text{Eu}^{3+}$  core particles, the increase in the yttrium XPS peak should increase linearly.

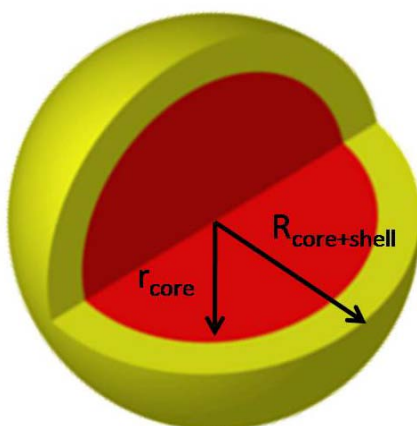


Figure 4-5. Idealized concentric spherical core/shell structure from which a maximum shell thickness for a given R can be calculated.

XPS spectra in Figure 4-4 (a) show that as the Y:Gd precursor ratio was increased, the Gd  $3d_{5/2}$  (binding energy-BE  $\sim 1175$  eV, kinetic energy-KE  $\sim 310$  eV) and Gd 4d peaks (BE  $\sim 152$  eV, KE  $\sim 1334$  eV) decreased while the Y 3d peak (BE  $\sim 167$  eV, KE  $\sim 1319$  eV) increased. The normalized attenuated intensities of the Gd  $3d_{5/2}$  peak fit an exponential function (solid line in Figure 4-4 (b)), proving that a  $\text{Y}_2\text{O}_3$  shell was formed on the  $\text{Gd}_2\text{O}_3:\text{Eu}^{3+}$  core [139]. Since the attenuation of the Gd XPS peak is exponential with thickness, the thickness determined from Figure 4-4b is the 'minimum' thickness of

the shell determined by assuming an attenuation distance of 0.8 nm for the 310eV photoelectron in  $Y_2O_3$  [140]. The shell thickness increased with increasing R to a value of  $\sim 0.6$  nm with an R = 1:1. While a thickness of 0.6 nm is small relative to the unit cell of yttria, the lattice parameters and crystal structures of the two oxides are very similar suggesting that epitaxial growth is probable and therefore this small shell thickness is reasonable.

As pointed out above, an exponential increase in the Y 4d XPS peak would be expected if the  $Y_2O_3$  were all present only in a shell. Instead the increase of the Y 4d was linear with the precursor ratio, consistent with  $Y_2O_3$  being present both as a co-precipitate and as a shell.

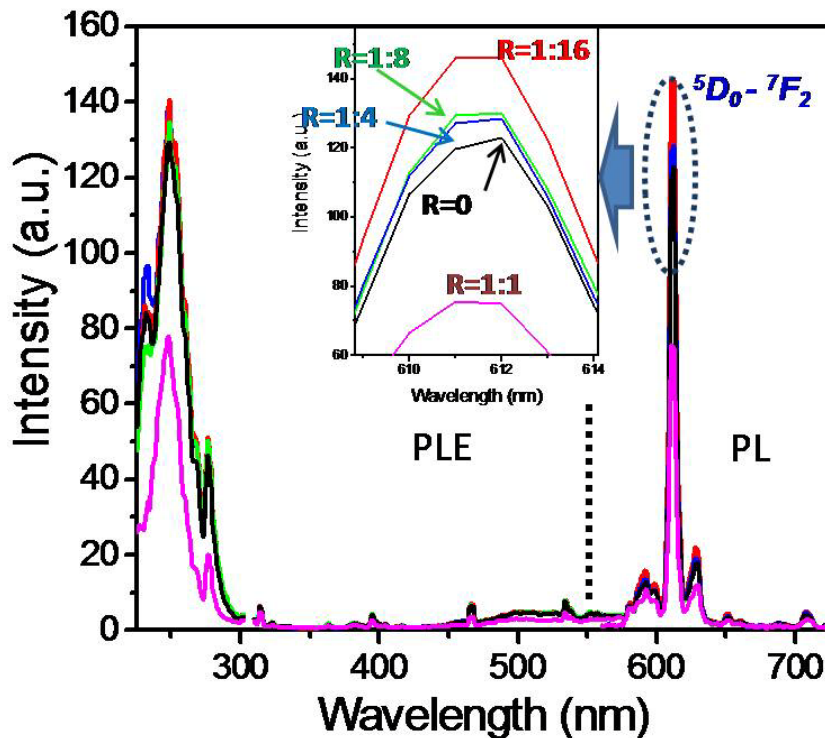


Figure 4-6. PL and PLE spectra from  $Gd_2O_3:Eu^{3+}$  and  $Gd_2O_3:Eu^{3+}/Y_2O_3$  core/shell nanoparticles. The PLE spectra are for emission at 612 nm and the PL spectra are for excitation at 250 nm. The inset shows the uncorrected PL peak intensity versus the value of R.

The presence of both nanoparticles and shell  $Y_2O_3$  is consistent with the observation by TEM that the average particle size was constant and  $\sim 21$  nm. A fraction of the  $Y_2O_3$ , must be present as nanoparticles based on the following argument. Assuming that the shape of the core/shell nanoparticles is spherical and concentric (Figure 4-5), and that the Gd and Y precursors react completely to produce only a core and a shell, respectively, the  $Y_2O_3$  shell would be  $\sim 2.3$  nm thick for 21 nm diameter cores and  $R = 1:1$ . This predicted shell thickness is four times larger than that measured by XPS, leading to the conclusion that some of the  $Y_2O_3$  exists as a separate phase, consistent with the XRD peak shift in Figure 4-1c and Figure 4-2.

#### **4.3.3 Photoluminescence Properties of Core and Core/Shell Nanoparticles**

Figure 4-6 (a) shows PL and PLE spectra from the bare  $Gd_2O_3:Eu^{3+}$  and  $Gd_2O_3:Eu^{3+}/Y_2O_3$  (core/shell) nanoparticles. PL emission and excitation spectra were measured from thin films drop-cast as described above, and were very reproducible as indicated by error bars in Figure 4-7. The PL spectra were dominated by the  ${}^5D_0-{}^7F_2$  transition of  $Eu^{3+}$  at 612 nm, while the PLE spectra were composed of a broad (FWHM  $\approx 30$  nm) peak centered at  $\sim 250$  nm and sharp peaks between 360 and 530 nm. The broad peak near 250 nm is from the oxygen to europium charge transfer band (CTB) and the sharp peaks between 360 and 530 nm are from europium direct excitation. The same characteristic PLE features have been reported for  $Eu^{3+}$ -doped nanoparticles prepared by combustion, precipitation and the polyol method using chloride precursors [141-143]. All core/shell nanoparticles, except for the  $R = 1:1$  sample, exhibited stronger PL emission than did bare  $Gd_2O_3:Eu^{3+}$  nanoparticles. The PL intensity was measured from a constant weight (volume) of nanoparticles, therefore it should have been lower at

all R values because a significant fraction of the sample was non-luminescent  $Y_2O_3$  (due to the absence of  $Eu^{3+}$  dopants).

Without another effect such as surface passivation, weaker PL intensities would be expected independent of whether the undoped  $Y_2O_3$  was in a shell or in separate nanoparticles. The XRD data could also be consistent with forming a solid solution of  $Gd_xY_{2-x}O_3:Eu^{3+}$  during calcining, but the temperature is too low for alloying. Furthermore, Li, et al report lower PL from such a solution [144], which they attributed to less efficient charge transfer between oxygen and yttrium versus oxygen to gadolinium.

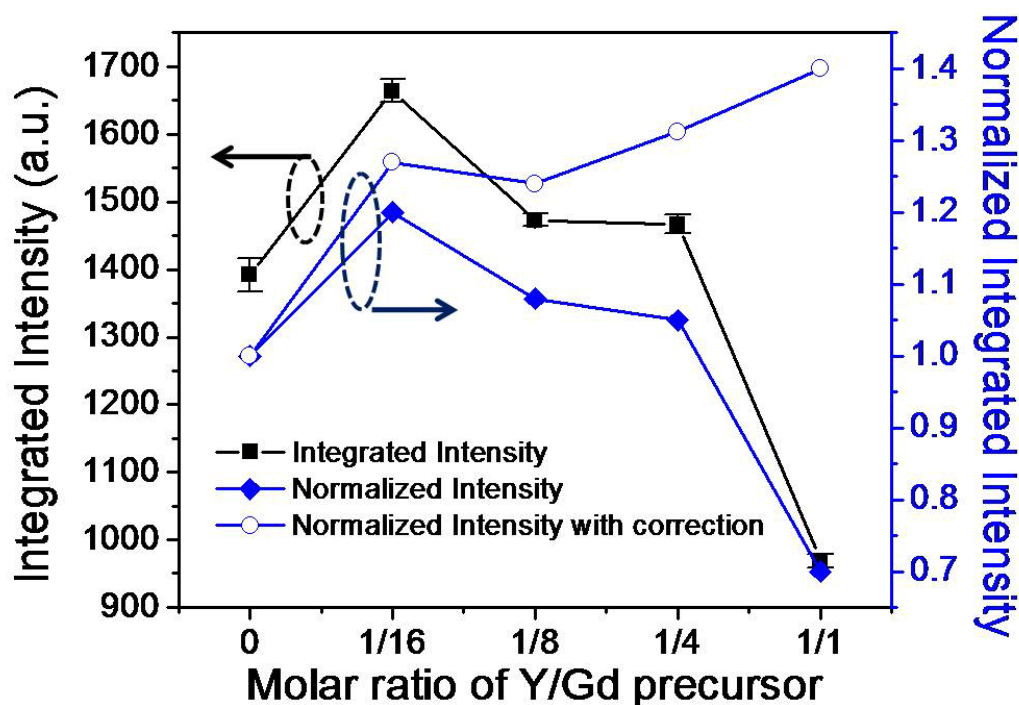


Figure 4-7. Integrated area of PL peak at 612 nm versus R; Solid squares are uncorrected data. Solid diamonds are uncorrected normalized data. Open circles are normalized and corrected for the fraction of non-luminescent  $Y_2O_3$  based on the value of R.

The enhanced PL shown by the corrected data in Figure 4-7 must result from passivation due to formation of the core/shell structure. Figure 4-7 is a plot of integrated area under the PL peak (560~725 nm and normalized to bare  $Gd_2O_3:Eu^{3+}$ ) versus the

$Y_2O_3$  shell thickness from the XPS data in Figure 4-4b. Without correcting for the fraction of non-radiative  $Y_2O_3$ , the normalized PL intensity had an apparent maximum ( $\sim 1.2$ ) at a shell thickness of 0.1 nm, grown with the lowest Y:Gd precursor ratio of  $R=1:16$ . The normalized uncorrected PL intensity gradually decreased for higher values of  $R$  (filled squares in Figure 4-7). However, after correcting for the fraction of non-luminescent  $Y_2O_3$  (open diamonds in Figure 4-7), all core/shell nanoparticles exhibit a larger PL intensity than pure  $Gd_2O_3:Eu^{3+}$  nanoparticles, with the thickest shell of 0.6 nm grown with the highest  $R=1:1$  being  $\sim 40\%$  brighter. This increased PL intensity is attributed to a reduced concentration of non-radiative recombination surface sites due to the  $Y_2O_3$  shell on the  $Gd_2O_3:Eu^{3+}$  core. The larger increase in PL intensity at higher precursor ratios is attributed to better passivation by the  $Y_2O_3$  layer at larger values of  $R$ .

The quantum efficiency (QE) of the present  $Gd_2O_3/Y_2O_3$  core/shell nanoparticles was not measured, However, their QEs are expected to be  $\sim 40\%$  based on our previous results from similar materials [145].

#### 4.3.4 Luminescence Decay Times of Core and Core/Shell Nanoparticles

To evaluate whether the rate of non-radiative decay was reduced by the formation of the  $Y_2O_3$  shell, the luminescence decay times were measured for bare  $Gd_2O_3:Eu^{3+}$  and  $Y_2O_3/Gd_2O_3:Eu^{3+}$  core/shell nanoparticles (Figure 4-8). The PL decay of both unpassivated core (Figure 4-8a) and core/shell (Figure 4-8b with  $R = 1:1$ ) nanoparticles were very well fit by a single exponential function, i.e. by  $I=I_0\exp(-t/\tau)$  where  $\tau$  is the decay time constant. As the thickness of the  $Y_2O_3$  shell increased, the decay time ( $\tau$ ) monotonically increased from 1.30 ms to 1.44 ms, as shown in Figure 4-8 (c). The decay time for the  $^5D_0 \rightarrow ^7F_2$  transition in  $Eu^{3+}$  doped  $Y_2O_3$  or  $Gd_2O_3$  has been reported to be 1~2 ms [146, 147], consistent with our data. Even though the value of  $\tau$  increased

only ~11% upon creation of the  $\text{Y}_2\text{O}_3$  shell, the error bars in Figure 4-8 (c) are small, indicating that the increase in decay time is real.

The longer luminescence decay time for  $\text{Eu}^{3+}$  in  $\text{Gd}_2\text{O}_3$  is consistent with a reduced rate of non-radiative relaxation due to the  $\text{Y}_2\text{O}_3$  shell passivating surface states [87, 148].

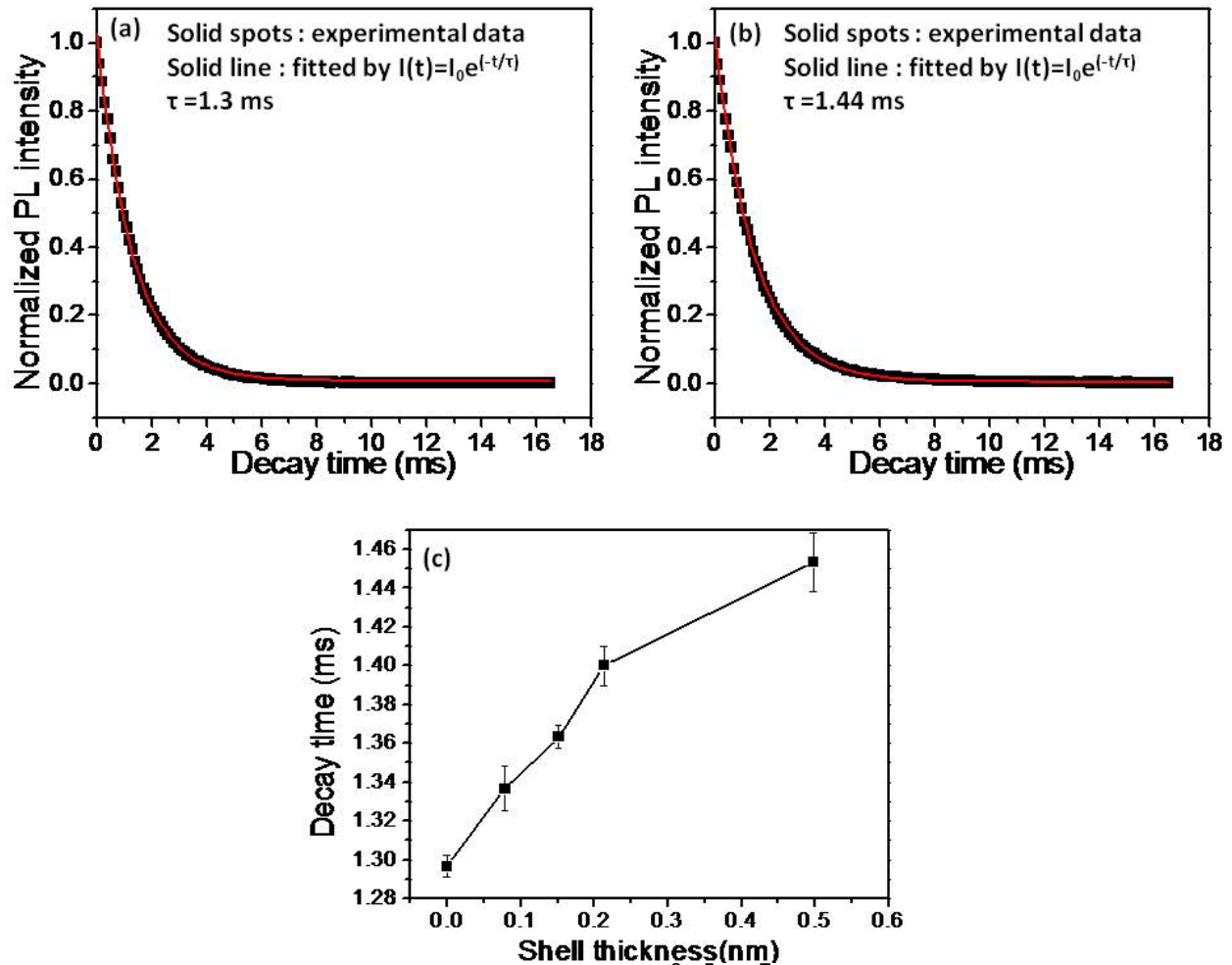


Figure 4-8. Luminescence decay data for the  $\text{Eu}^{3+} {}^5\text{D}_0 \rightarrow {}^7\text{F}_2$  transition (612 nm peak). The data are well fit by the solid line which is a single exponential function with a time constant

Unpassivated surface states are known to trap charge carriers which lead to fast non-radiative recombination and therefore shorter luminescent relaxation time constants.

#### 4.4 Conclusion

Nanocores (~21 nm diameter) of  $\text{Gd}_2\text{O}_3:\text{Eu}^{3+}$  with both a  $\text{Y}_2\text{O}_3$  shell and undoped  $\text{Y}_2\text{O}_3$  co-precipitated nanoparticles were synthesized by a facile two-step high boiling-point alcohol (polyol) method at 180 °C in air for times of a few hours. Data from XRD, TEM, XPS, PL and luminescent decay time measurements from calcined (600 °C, 2 hrs in air) samples showed that crystalline  $\text{Y}_2\text{O}_3$  shells up to 0.6 nm thick were formed on the crystalline  $\text{Gd}_2\text{O}_3:\text{Eu}^{3+}$  core and that the thickest shell resulted in a 40% increase in PL intensity and an 11% longer PL decay time relative to uncoated  $\text{Gd}_2\text{O}_3:\text{Eu}^{3+}$  nanoparticles. These changes were attributed to passivation of surface states that resulted in reduced rates of non-radiative relaxation processes.

CHAPTER 5  
ENHANCED PHOTOLUMINESCENCE FROM EUROPIUM DOPED GADOLINIUM  
OXIDE BASED CORE/DUAL-SHELL NANOPARTICLES

**5.1 Introduction**

Nanophosphors with rare-earth materials are of interest due to their potential applications in lightings, displays, biological diagnosis and scintillators [125, 145, 149, 150]. Among rare-earth materials, gadolinium oxide is a versatile material with potential applications in several fields of technology. When doped with rare-earth ions ( $\text{Eu}^{3+}$  and  $\text{Tb}^{3+}$ ), it exhibits good luminescent properties [47, 151, 152].

For nanophosphors, core/shell hetero-structures have been created in two different configurations, the first of which is a luminescent core and surface passivation shell. Several investigators have reported that the luminescent efficiency of nanophosphors was lower than that of their corresponding bulk counterparts due to the non-radiative recombination at surface defects [87, 131]. They frequently reported increased luminescent efficiency upon addition of the passivating shell [122, 123]. A second configuration of the core/shell hetero-structure is a non-luminescent core and luminescent shell. There are several reports of silica nanocores coated with various phosphor shells [132, 153, 154]. These core/shell structures have several advantages, the first being easy control of the size of mono-dispersed spherical silica cores from nanometers to micrometers [155, 156]. Second, silica is cheap as compared to the more expensive rare earth phosphor materials, therefore the silica core/luminescent shell structures should result in lower costs. However, luminescent shells inherently have very large surface to volume ratio, and frequently exhibit low quantum yields due to surface states. Here we report a silica core/dual-shell with a luminescent  $\text{Gd}_2\text{O}_3:\text{Eu}^{3+}$

shell and passivating  $Y_2O_3$  shell which can reduce cost and double the quantum yield these potential scintillator materials.

## 5.2 Experimental

### 5.2.1 Materials

Gd(III) nitrate hydrate (99.9%), Eu(III) nitrate hexahydrate (99.9%) and Y(III) nitrate (99.9%) were purchased from Aldrich Chemical Co.. Tetraethyl orthosilicate (TEOS, 98%) and ethanol were purchased from Acros Organics. All chemicals were analytical grade and were used without further purification.

### 5.2.2 Synthesis of Silica Cores

Silica nanocores were fabricated via the Stöber method [157], where 5 ml of concentrated ammonium hydroxide ( $NH_4OH$ ) was mixed with 20 ml of deionized (DI) water and 100 ml of ethanol and stirred vigorously. Then 10 ml of tetraethyl orthosilicate (TEOS) was added quickly and stirred for 2 hrs without heating. After a few minutes, the solution became translucent and then cloudy white as the  $SiO_2$  particles grew large enough to scatter visible light. To remove unreacted precursors, the nanoparticles were centrifuged and re-dispersed in ethanol at least three times, followed by drying at 70 °C for 12 hrs in air.

### 5.2.3 Synthesis of $Gd_{2}O_3:Eu^{3+}$ Shell on $SiO_2$ Cores

Growth of  $Gd_{1.6}O_3:Eu_{0.4}^{3+}$  shells was accomplished with a solution precipitation method, in which 500 mg of silica cores were added to 100 ml of DI water and the mixture was sonicated to achieve a homogeneous suspension. This was followed by addition of 4 mmol of gadolinium nitrate and 1 mmol of europium nitrate and 125 mmol of urea which was reacted at 85 °C. After 1.5 hrs synthesis, nanoparticles were

collected and washed as discussed above. Some of the core/shell nanoparticles were calcined at 600 °C for 2 hrs in air.

#### **5.2.4 Synthesis of Y<sub>2</sub>O<sub>3</sub> Outer Shell on SiO<sub>2</sub>/Gd<sub>2</sub>O<sub>3</sub>:Eu<sup>3+</sup> Nanoparticles**

Growth of SiO<sub>2</sub>/Gd<sub>2</sub>O<sub>3</sub>:Eu<sup>3+</sup>/Y<sub>2</sub>O<sub>3</sub> core/dual-shell nanoparticles was accomplished with a two-pot solution precipitation method. In the first flask, 250 mg of as-prepared SiO<sub>2</sub>/Gd<sub>2</sub>O<sub>3</sub>:Eu<sup>3+</sup> nanoparticles and 50 mmol of urea were added at RT to 30 ml of DI water and the mixture was stirred vigorously. In the second flask, 2.5 mmol of yttrium nitrate was added to 20 ml of DI water. After mixing for 30 min, the yttrium precursor-solution was added to the first flask at 85°C. After 1.5 hrs, the nanoparticles were collected and washed as discussed above. A fraction of the core/dual-shell nanoparticles were calcined at 600 °C for 2 hrs in air.

#### **5.2.5 Characterization of Nanoparticles**

Morphology and size of nanoparticles were determined using a JEOL 2010F high resolution transmission electron microscope (HR-TEM) operated at 200 kV. The TEM samples were prepared by drop-casting nanoparticles dispersed in ethanol onto a carbon-coated holey copper grid. The crystal structure of as-synthesized and calcined nanoparticles was characterized by X-ray diffraction (XRD) with a Philips APS 3720 diffractometer using Cu K<sub>α</sub> radiation ( $\lambda = 1.54178\text{\AA}$ ). The XRD patterns were collected from dried powder samples with a 0.02 ° step scan mode over a 2 $\theta$  range of 20-70 °.

X-ray photoelectron spectroscopy (XPS) was used to determine the shell thickness of nanoparticles. Data were collected with a Perkin-Elmer PHI 5100 ESCA system and Al Ka X-rays (E=1.486 keV). All the XPS peaks were referenced to the C 1s peak at 284.6 eV. XPS samples were prepared by drop casting 50  $\mu$ l of a 2 mg/ml solution of nanoparticles dispersed in ethanol onto 1 cm<sup>2</sup> aluminum foil.

Photoluminescence (PL), photoluminescence excitation (PLE) spectra and luminescent relaxation lifetime were measured at room temperature using a JASCO FP-6500/6600 research grade fluorescence spectrometer with a 150 W Xenon lamp. Quantum yields were measured using an integrating sphere. The samples for PL, PLE and quantum yields were films prepared by adding calcined nanoparticles to 500  $\mu\text{L}$  of 4% of poly(methyl methacrylate) (PMMA) dispersed in chlorobenzene and drop-cast onto quartz substrates.

## 5.3 Results and Discussion

### 5.3.1 Morphology and Crystal Structure of Core/Shell Nanoparticles

The morphology and size of as-prepared  $\text{SiO}_2$  nanocores are shown in Figure 5-1(a). Based on TEM images, mono-dispersed  $\text{SiO}_2$  nanocores were spherical and with a diameter of 450 nm. A  $\sim 5$  nm of  $\text{Gd}_2\text{O}_3:\text{Eu}^{3+}$  layer was coated on  $\text{SiO}_2$  nanocores by the urea precipitation method, as shown in Figure 5-1(b and c). A nearly uniform  $\text{SiO}_2/\text{Gd}_2\text{O}_3:\text{Eu}^{3+}$  core/shell nanostructure was obtained, as indicated by the outer darker and inner lighter regions corresponding to the  $\text{Gd}_2\text{O}_3:\text{Eu}^{3+}$  shell and  $\text{SiO}_2$  core, respectively. Figure 5-1(d) shows a  $\text{SiO}_2/\text{Gd}_2\text{O}_3:\text{Eu}^{3+}/\text{Y}_2\text{O}_3$  core/dual-shell nanoparticle. A dark  $\text{Gd}_2\text{O}_3:\text{Eu}^{3+}$  ring between two lighter regions is observed, due to differences in the average atomic number. The outer  $\text{Y}_2\text{O}_3$  shell is  $\sim 45$  nm thick and it uniformly covers the  $\text{SiO}_2/\text{Gd}_2\text{O}_3:\text{Eu}^{3+}$  core/single-shell nanoparticles. According to XRD data, as-grown silica nanocores were amorphous with an amorphous scattering peak at  $\sim 27^\circ$ , as shown in Figure 5-2(a). However, calcined  $\text{SiO}_2/\text{Gd}_2\text{O}_3:\text{Eu}^{3+}$  core/shell nanoparticles showed crystalline peaks that matched JCPDS data from cubic  $\text{Gd}_2\text{O}_3$  (Card 43-1014).

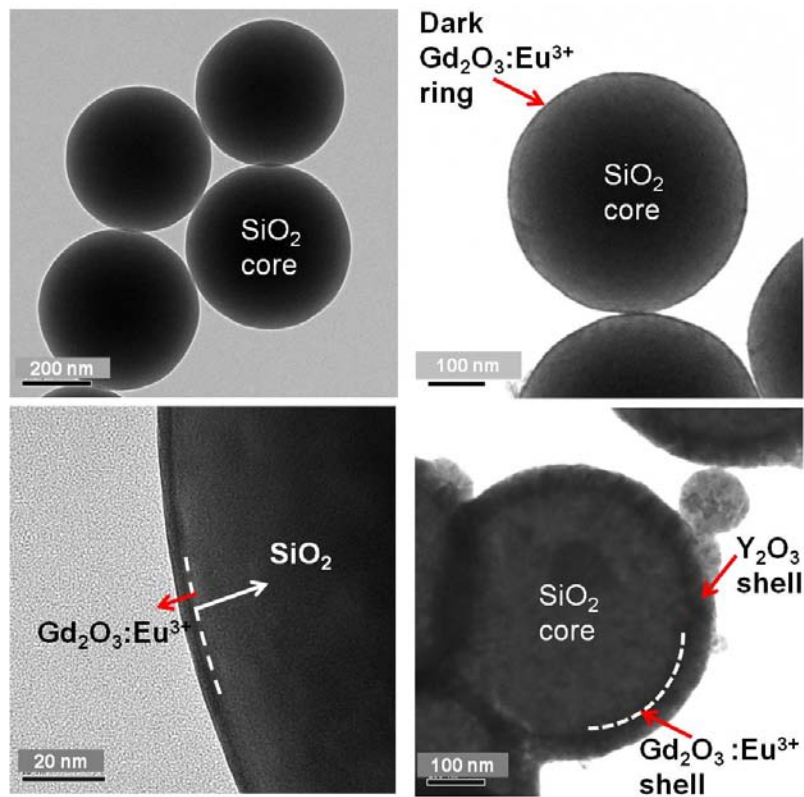


Figure 5-1. TEM photomicrographs of dual-shell.

The broad peaks indicate very small grain size ( $\sim 8$  nm) which is consistent with the TEM thickness of the  $\text{Gd}_2\text{O}_3:\text{Eu}^{3+}$  shell. In Figure 5-2(b), the XRD pattern from calcined core/dual-shell nanoparticles with a  $\text{Y}_2\text{O}_3$  outer shell show two different peaks at large Bragg angles, one is from cubic  $\text{Gd}_2\text{O}_3$  structure and the second is from cubic  $\text{Y}_2\text{O}_3$  structure (Card # 43-1036). Due to the larger volume of the  $\sim 45$  nm thick  $\text{Y}_2\text{O}_3$  shell compared to the  $\sim 5$  nm thick  $\text{Gd}_2\text{O}_3:\text{Eu}^{3+}$  shell, the XRD peak intensities are dominated by the cubic  $\text{Y}_2\text{O}_3$  and therefore two separate peaks cannot be detected in the  $30^\circ$  angle region due to the small intensity of  $\text{Gd}_2\text{O}_3$  peaks. However for  $2\theta$  above  $50^\circ$ , the weak  $\text{Y}_2\text{O}_3$  peaks separated from the  $\text{Gd}_2\text{O}_3$  peaks can be seen.

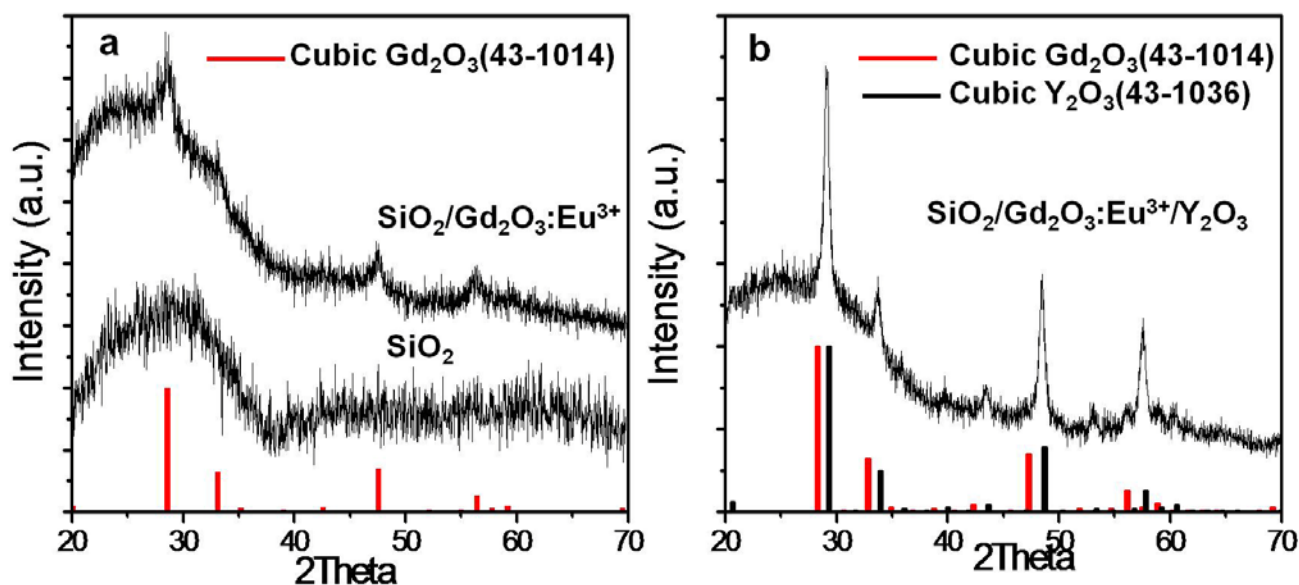


Figure 5-2. X-Ray diffraction spectra obtained from pure amorphous silica nanoparticles or calcined  $\text{SiO}_2/\text{Gd}_2\text{O}_3:\text{Eu}^{3+}$  core/single-shell nanoparticles and calcined  $\text{SiO}_2/\text{Gd}_2\text{O}_3:\text{Eu}^{3+}/\text{Y}_2\text{O}_3$  core/dual-shell nanoparticles.

### 5.3.2 Surface Analysis of Core/Shell Nanoparticles

X-ray photoelectron spectroscopy (XPS) analysis is commonly used to investigate the composition and chemical bonds in surface layers up to depths of a few nm. If  $\text{SiO}_2$  nanocores are coated with  $\text{Gd}_2\text{O}_3:\text{Eu}^{3+}$  and  $\text{Y}_2\text{O}_3$  shells, the XPS signal from the core should be much less than those from the shells. Figure 5-3 shows XPS data for binding energies between 135-170 eV from films of  $\text{SiO}_2$  core,  $\text{SiO}_2/\text{Gd}_2\text{O}_3:\text{Eu}^{3+}$  core/single-shell and  $\text{SiO}_2/\text{Gd}_2\text{O}_3:\text{Eu}^{3+}/\text{Y}_2\text{O}_3$  core/dual-shell nanoparticles. For a  $\text{SiO}_2$  nanocore sample, only the Si 2s peak (binding energy (BE)  $\sim 157$  eV) was detected. A core/dual-shell sample with a thick  $\text{Y}_2\text{O}_3$  outer shell exhibited only the Y 3d peak (BE  $\sim 163$  eV). However, a core/single-shell sample with an  $\sim 5$  nm  $\text{Gd}_2\text{O}_3:\text{Eu}^{3+}$  layers showed a small Si 2s peak at BE  $\sim 157$  eV, as well as a large Gd 4d peaks (BE  $\sim 147$  eV). The small 157 eV Si 2s XPS peak results from an exponential attenuation of the intensity of the silica core photoelectron peak [139].

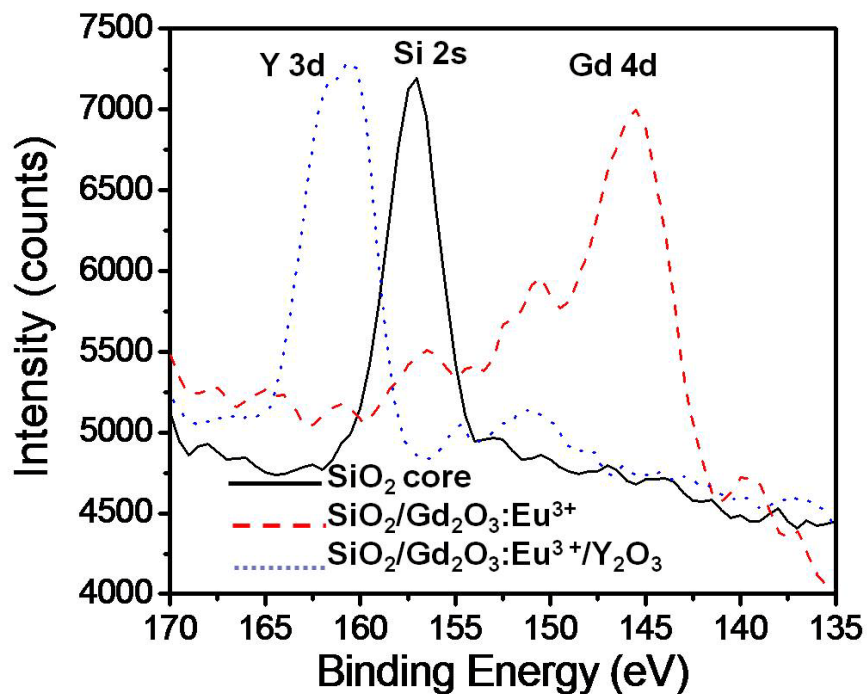


Figure 5-3. X-ray photoelectron peaks from the SiO<sub>2</sub> nanocores (solid line), from SiO<sub>2</sub>/Gd<sub>2</sub>O<sub>3</sub>:Eu<sup>3+</sup> core/single-shell (dashed line) and SiO<sub>2</sub>/Gd<sub>2</sub>O<sub>3</sub>:Eu<sup>3+</sup>/Y<sub>2</sub>O<sub>3</sub> core/dual-shell nanoparticles (dotted line).

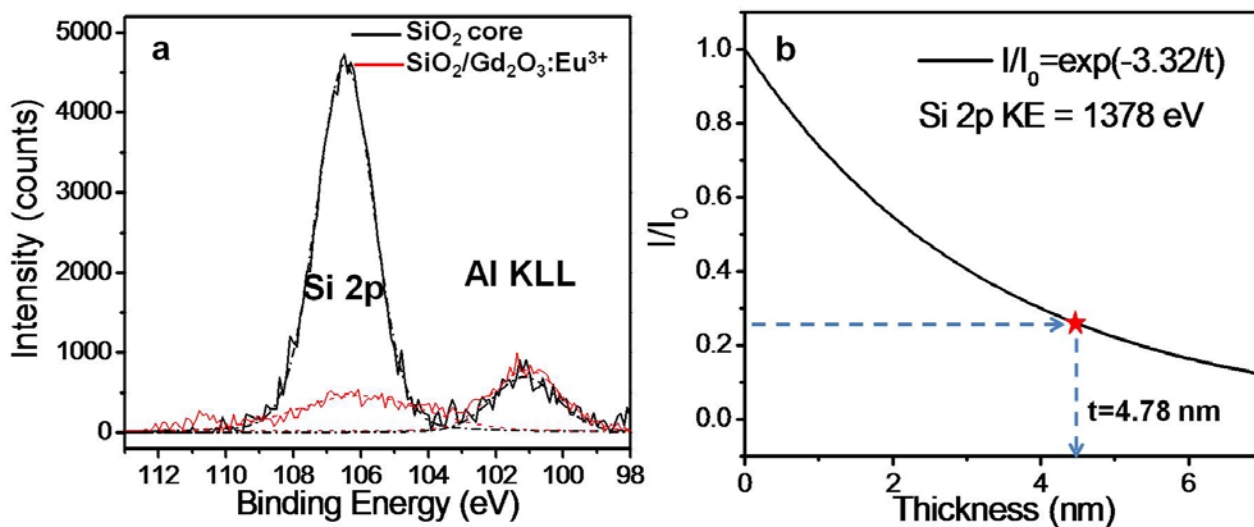


Figure 5-4. The Si 2p XPS peaks from SiO<sub>2</sub>, SiO<sub>2</sub>/Gd<sub>2</sub>O<sub>3</sub>:Eu<sup>3+</sup> core/single-shell nanoparticles and normalized intensity of the Si 2p peak versus Gd<sub>2</sub>O<sub>3</sub>:Eu<sup>3+</sup> shell thickness.

To avoid ambiguity due to overlap with other peaks, attenuation of the Si 2p XPS peak (BE ~ 106 eV) was analyzed, as shown in Figure 5-4(a). Since attenuation of XPS

peak is an exponential function of the overlayer thickness, the thickness of the  $\text{Gd}_2\text{O}_3:\text{Eu}^{3+}$  shell can be determined from  $I/I_0 = \exp(-t/\lambda)$ , where  $I$  is an intensity of an XPS peak from the core,  $I_0$  is the intensity of this peak from a bare core,  $t$  is the thickness of the shell, and  $\lambda$  is the inelastic mean-free-path of the photoelectron [139]. The inelastic mean-free-path of a 106 eV BE photoelectron in  $\text{Gd}_2\text{O}_3$  was determined using the NIST Standard Reference Database 71 to be 3.32 nm for an electron with a Kinetic Energy (KE) = 1378 eV (BE = 106 eV) [158]. The calculated thickness of the  $\text{Gd}_2\text{O}_3:\text{Eu}^{3+}$  thin shell from  $I/I_0 = 0.26$  is 4.78 nm, which is consistent with the TEM value of  $\sim 5$  nm.

### 5.3.3 Luminescence Properties of Core/Shell Nanoparticles

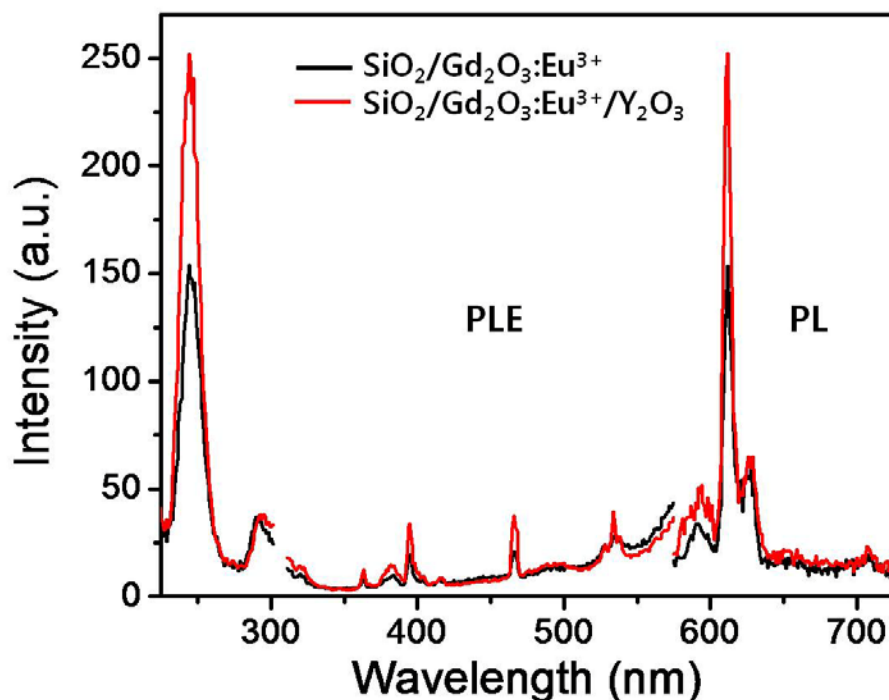


Figure 5-5. Photoluminescence (PL) and photoluminescence excitation (PLE) spectra from  $\text{SiO}_2/\text{Gd}_2\text{O}_3:\text{Eu}^{3+}$  core/single-shell and  $\text{SiO}_2/\text{Gd}_2\text{O}_3:\text{Eu}^{3+}/\text{Y}_2\text{O}_3$  core/dual-shell nanoparticles. The PLE spectra are for emission at 612 nm and the PL spectra are for excitation at 250 nm.

Figure 5-5 shows PL and PLE spectra from  $\text{SiO}_2/\text{Gd}_2\text{O}_3:\text{Eu}^{3+}$  and  $\text{SiO}_2/\text{Gd}_2\text{O}_3:\text{Eu}^{3+}/\text{Y}_2\text{O}_3$  calcined nanoparticles in drop-cast films prepared as described

above. In order to measure the photoluminescent properties with the same amount of luminescent  $\text{Gd}_2\text{O}_3:\text{Eu}^{3+}$ , in other words to keep the number of particles constant, different weights of nanoparticles were dispersed in the PMMA matrix. Assuming that core/dual-shell nanoparticles are spherical and concentric (see Figure 5-6) with theoretical densities, a simple calculation with the dimensions reported above gave the weight ratio between core/single-shell and core/dual-shell to be 2.3.

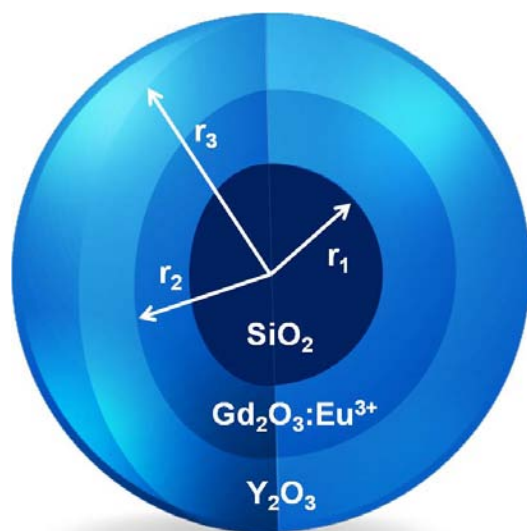


Figure 5-6. Model of a spherical core/concentric dual-shell structure from which the weight of nanoparticles necessary for a constant volume of luminescent  $\text{Gd}_2\text{O}_3:\text{Eu}^{3+}$  can be determined.

As shown in Figure 5-5, the PL spectra were dominated by the  $^5\text{D}_0 - ^7\text{F}_2$  transition of  $\text{Eu}^{3+}$  ions at 612 nm, while the PLE spectra were composed of a broad peak under 300 nm and sharp peaks between 360 and 550 nm. The broad peak is from the oxygen to europium charge transfer band (CTB) and the sharp peaks are associated with direct excitation of the f-f shell transitions of europium, which is the same characteristic PLE features have been reported for a variety of oxide nanoparticle hosts doped with  $\text{Eu}^{3+}$  ions and prepared by various methods [114, 142].

### 5.3.4 Thin Film Quantum Yield Measurement

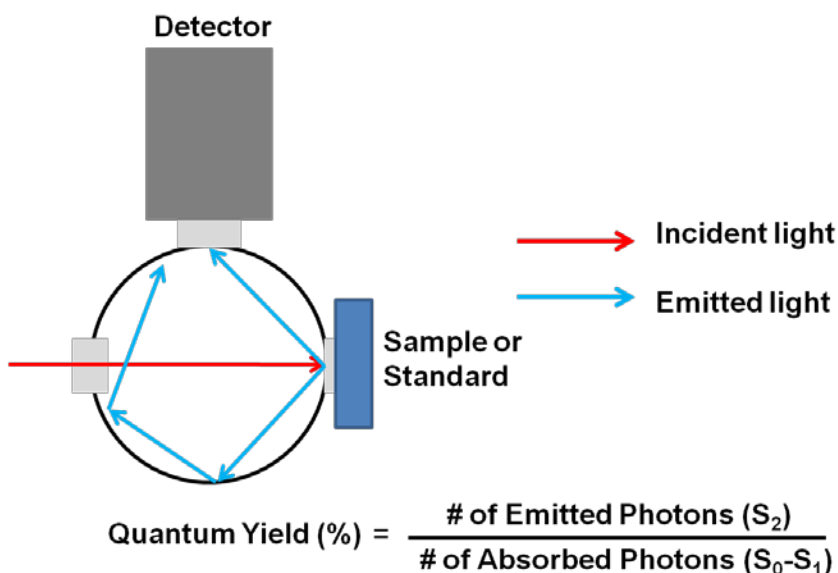


Figure 5-7. Schematic diagram of thin film quantum yield (QY) measurement.

The quantum yield of thin-film photoluminescence was measured with a spectrophotometer (FP-6500, Jasco, Inc.) equipped with a DC-powered 150W Xenon lamp source and a photomultiplier tube (PMT) detector. A quantum yield measurement system for solid thin film samples collects the photons with an integrating sphere (60 mm diameter; BaSO<sub>4</sub> coating; Spectralon reflectance standards). The quantum yield (QY) of luminescent materials is defined to be the fractional or percentage ratio of the number of emitted photons to the number of absorbed photons, i.e. S<sub>2</sub> divided by (S<sub>0</sub>-S<sub>1</sub>) as illustrated in Figure 5-7.

Table 5-1. Quantum yield, radius, volume ratio and weight ratio of SiO<sub>2</sub>, SiO<sub>2</sub>/Gd<sub>2</sub>O<sub>3</sub>:Eu<sup>3+</sup> core/single-shell and SiO<sub>2</sub>/Gd<sub>2</sub>O<sub>3</sub>:Eu<sup>3+</sup>/Y<sub>2</sub>O<sub>3</sub> core/dual-shell nanoparticles with density of each material.

Samples	Density (g/cm <sup>3</sup> )	Radius (nm)	Volume Ratio	Weight Ratio	Quantum Yield (%)
SiO <sub>2</sub>	ρ <sub>SiO2</sub> = 2.648	200	1	1	
SiO <sub>2</sub> /Gd <sub>2</sub> O <sub>3</sub> :Eu <sup>3+</sup>	ρ <sub>Gd2O3</sub> = 7.07	205	1.08	1.21	11.9
SiO <sub>2</sub> /Gd <sub>2</sub> O <sub>3</sub> :Eu <sup>3+</sup> /Y <sub>2</sub> O <sub>3</sub>	ρ <sub>Y2O3</sub> = 5.01	248	1.91	2.78	20.3

Here  $S_0$  is the number of incident photons measured using a reflective standard (Alumina block),  $S_1$  and  $S_2$  are the number of incident photons not absorbed and emitted photons from thin film samples, respectively [159, 160].

As shown in Table 5-1, for excitation at 285 nm, the QY was 11.9% and 20.3% from  $\text{SiO}_2/\text{Gd}_2\text{O}_3:\text{Eu}^{3+}$  and  $\text{SiO}_2/\text{Gd}_2\text{O}_3:\text{Eu}^{3+}/\text{Y}_2\text{O}_3$ , respectively. The increased PL intensity and QY from coating with the non-luminescent  $\text{Y}_2\text{O}_3$  outer shell is attributed to a reduced probability of non-radiative recombination on the surface states due to the  $\text{Y}_2\text{O}_3$  outer shell on the  $\text{SiO}_2/\text{Gd}_2\text{O}_3:\text{Eu}^{3+}$  core/single-shell.

### 5.3.5 Luminescent Decay Time of Core/Shell Nanoparticles

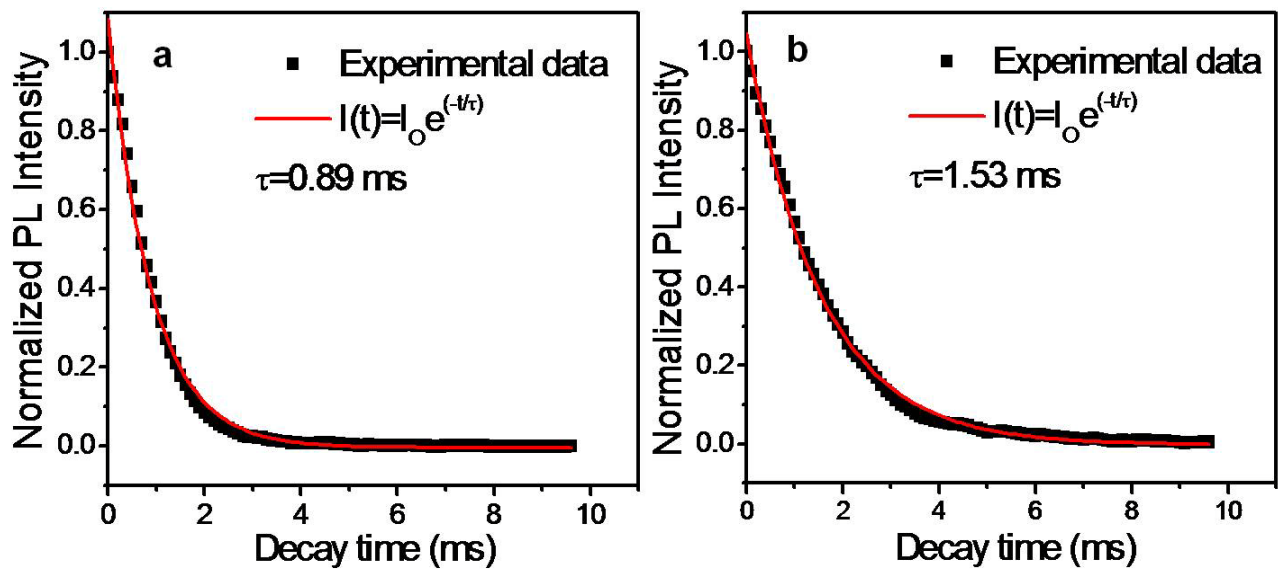


Figure 5-8. Luminescence decay data for the  $\text{Eu}^{3+} 5\text{D}_0 - 7\text{F}_2$  transition (612 nm peak). The data fit very well a single exponential decay (solid line) with a time constant  $\tau$ .

To test the postulate that the  $\text{Y}_2\text{O}_3$  outer shell reduced the rate of non-radiative recombination, the luminescence decay lifetimes were measured for  $\text{SiO}_2/\text{Gd}_2\text{O}_3:\text{Eu}^{3+}$  and  $\text{SiO}_2/\text{Gd}_2\text{O}_3:\text{Eu}^{3+}/\text{Y}_2\text{O}_3$  nanoparticles, as shown in Figure 5-8. The luminescent decay curves from both core/single-shell and core/dual-shell nanoparticles were well fit

by a single exponential curve, i.e. by  $I=I_0\exp(-t/\tau)$ , where  $\tau$  is the decay time constant. The  $Y_2O_3$  outer shell on  $SiO_2/Gd_2O_3:Eu^{3+}$  core/single-shell nanoparticles increased the decay times from 0.89 ms to 1.53 ms, consistent with a sharp reduction in non-radiative transitions, and therefore more radiative relaxation over longer time constants.

The decay time for the  ${}^5D_0 - {}^7F_2$  transition in  $Eu^{3+}$  doped rare-earth oxides has reported to be  $\sim 1-2$  ms [147, 161]. The short decay time of core/single-shell nanoparticles of 0.89 ms can we explain by the fact that the  $SiO_2/Gd_2O_3:Eu^{3+}$  core/shell nanoparticles are spherical and concentric, as described above, therefore the percentage of atoms locating on the outer surface (presumably was unsatisfied bonding) is approximately over 25%. Because of the dangling chemical bonds, there apparently were a large density of surface defects that trapped charge carriers and led to fast non-radiative recombination and therefore shorter luminescent relaxation time constants [87]. The  $Y_2O_3$  outer shell reduced the density of surface states and led to longer relaxation times.

#### 5.4 Conclusion

Nanocores (400 nm diameter) of  $SiO_2$  with a 4.5 nm thick  $Gd_2O_3:Eu^{3+}$  shell, and sometimes with a 43 nm thick  $Y_2O_3$  shell, were synthesized by the Stöber and by solution precipitation methods. The nanostructures were characterized by XRD, TEM, XPS and PL. As-synthesized samples were amorphous, but the shells after calcination (600 °C, 2 h in air) were crystalline, with both  $Gd_2O_3:Eu^{3+}$  and  $Y_2O_3$  shells being cubic while the  $SiO_2$  core remained amorphous. Excitation in the UV led to emission at  $\sim 612$  nm from the  $Eu^{3+}$  dopant in the  $Gd_2O_3$  shell with a quantum yield of 12%. Addition of the  $Y_2O_3$  shell increased the PL intensity by 72%, raising the QY to 20%. The increased QY

was attributed to passivation of surface states that led to reduced surface defect density and lower rate of non-radiative relaxation.

## CHAPTER 6

### X-RAY AND PHOTO-LUMINESCENCE FROM GADOLINIUM SILICATE DOPED WITH CERIUM NANOPARTICLES SYNTHESIZED BY SOLUTION BASED METHODS

#### 6.1 Introduction

Nano-materials are under intensive study because they exhibit novel electrical, optical and magnetic properties compared to their bulk counterparts. The physical properties of materials change when the size is reduced from bulk materials to nanocrystals approaching the size of molecules [76, 126]. For instance, the color of light from semiconductor nanoparticles (e.g. CdSe) can be tuned by changing the size of nanoparticles and these nanoparticles have been incorporated into light emitting devices [162].

Rare-earth oxyorthosilicates ( $R_2SiO_5$ ) doped with  $Eu^{3+}$ ,  $Ce^{3+}$ ,  $Tb^{3+}$  and  $Pr^{3+}$  have been widely used for luminescent materials due to their scintillation, cathodoluminescent and storage phosphor properties [163, 164]. In particular, Ce doped  $Gd_2SiO_5$  ( $GSO:Ce^{3+}$ ) is a promising scintillator material with high absorption coefficients for high energy particles, high luminescent output (20% of  $NaI:Tl^+$ ), excellent irradiation hardness ( $>10^8$ ) and fast decay times ( $<50$  nsec) [165]. The excellent scintillation characteristics enable  $GSO:Ce^{3+}$  to be used in medical imaging, radiation detection and high energy physics applications [101, 102, 150]. Normally  $GSO:Ce^{3+}$  detectors use a Czochralski grown single crystal, which is a difficult, expensive procedure that frequently denotes only small detector crystals [166]. Nano-sized rare-earth silicates have been suggested as an alternative to overcome the disadvantage. Rare-earth silicate nanoparticles doped with rare-earth ions have been synthesized by hydrothermal, sol-gel and solution combustion techniques, which require high reaction temperature or high temperature post-annealing for scintillation [167-169]. Here we

report a non-hydrolytic colloidal hot-solution growth method to produce nanocrystals of GSO. Colloidal growth in non-hydrolytic liquid media can produce a variety of shapes and 1–10 nm sizes of highly crystallized nanocrystals that can be dispersed in organic or aqueous media for numerous potential applications [25]. This chapter describes the synthesis of GSO:Ce<sup>3+</sup> nanoparticles and their structural characteristics and photoluminescence properties by UV and X-ray excitations.

## 6.2 Experimental

### 6.2.1 Hot Solution Synthesis

Gd<sub>2</sub>SiO<sub>5</sub> doped with Ce<sup>3+</sup> (Ce<sup>3+</sup> = 0.1, 0.2, 0.5, 2 and 5 mol %) nanoparticles were prepared by a two-pot hot solution synthesis for 90 min in oleylamine (Figure 6-1). The doping concentration is corresponding to the molar concentration of precursors. In a typical reaction to produce GSO nanoparticles doped with 5 mol % Ce<sup>3+</sup>, 1.9 mmol of Gd acetate was mixed with 5 ml of oleylamine in a three-neck reaction flask and heated to 120 °C. At the same time, 0.1 mmol of Ce acetate was mixed with 2 ml of oleylamine in a vial and heated to 120 °C. After 30 min, the Ce precursor solution was mixed with the Gd precursor solution and 2 mmol of (3-Aminopropyl)triethoxysilane (APTES) was injected into the precursor mixture solution. Finally, the temperature was raised to ~ 320 °C with a heating rate of 5-25 °C/min and maintained at that temperature for 90 min with vigorous stirring. After reflux, the brownish mixture was cooled down to room temperature by removing the heat source. Ethanol was added to the mixture, and GSO:Ce<sup>3+</sup> nanoparticles were precipitated and separated by centrifugations. This procedure was repeated at least three times to remove any residue. The purified GSO:Ce<sup>3+</sup> nanoparticles, capped with organic species, were well dispersed by organic

solvents such as hexane. After drying at 70 °C for 12 h, the nanoparticles were calcined at either 600 or 1000 °C for 2 h in laboratory air.

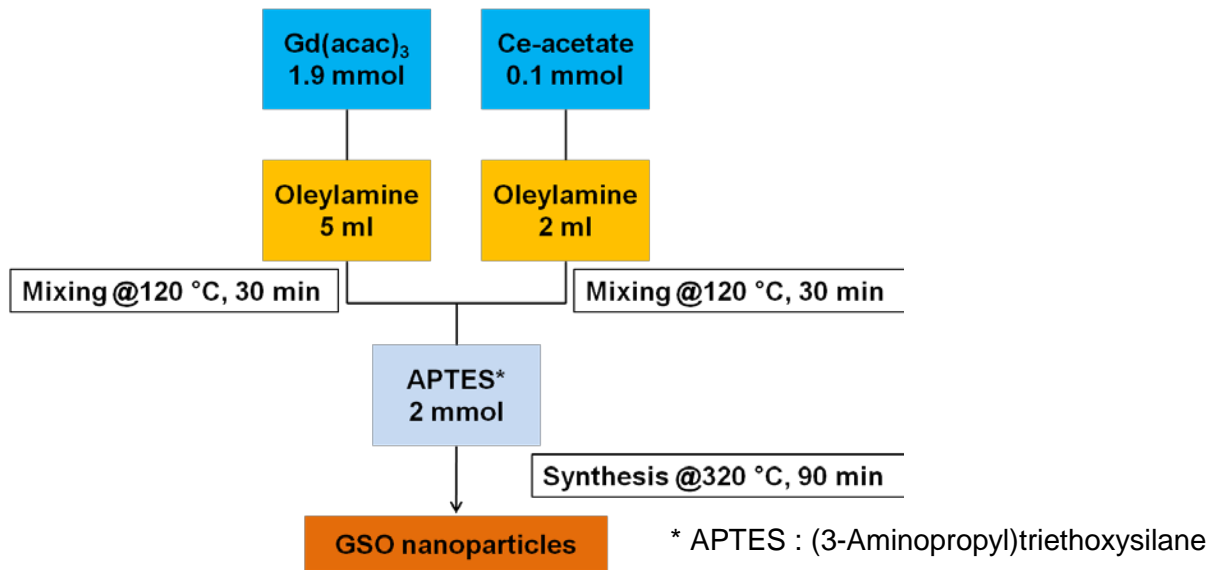


Figure 6-1. Flow chart of two-pot hot-solution growth of GSO nanoparticles

### 6.2.2 Sol-Gel Synthesis

Nanocrystalline  $\text{Gd}_2\text{SiO}_5:\text{Ce}^{3+}$  (0.5 mol%) was also prepared by a sol-gel method. First, high-purity  $\text{Gd}(\text{NO}_3)_3$  and  $\text{Ce}(\text{NO}_3)_3$  were dissolved in DI water to form Gd- $\text{Ce}(\text{NO}_3)_3$  solution. Next, an adequate amount of TEOS and  $\text{NH}_3(\text{OH})$  solution were added into the Gd-Ce solution. This solution was heated at 80 °C, which formed a gel, then was dried at 80 °C for 12 hrs. The resulting white powder was calcined at either 600 or in the 1000 °C for 2 h in air.

### 6.2.2 Characterization

The crystal structure of as-grown and calcined  $\text{GSO}:\text{Ce}^{3+}$  nanoparticles was characterized by X-ray diffraction (XRD) with a Philips APS 3720 diffractometer using  $\text{Cu K}\alpha$  radiation ( $\lambda=1.54178 \text{ \AA}$ ). The XRD patterns were collected from dried powder samples with a  $0.02^\circ$  step scan mode over a  $2\theta$  range of  $20\sim 70^\circ$ . Morphology and size of nanoparticles were determined with a JEOL 2010F high resolution transmission

electron microscope (HR-TEM) operated at an accelerating voltage of 200 kV. Specimens for the TEM were prepared by drop-casting particles dispersed in ethanol onto holey carbon-coated copper grids. Photoluminescence (PL) and photoluminescence excitation (PLE) spectra were measured at room temperature using a JASCO FP-6500/6600 research grade fluorescence spectrometer with a 150 W Xenon lamp. X-ray luminescence was measured with a 40 kV Bullet™ X-ray tube combined with a Ocean Optics USB-2000 miniature fiber optic spectrometer. The distance from the x-ray target to the sample was ~3 cm and the x-ray tube was operated at 100  $\mu$ A. For each measurement, a crucible with 57 mm<sup>2</sup> area was filled with nanopowder such that each sample had the same area exposed to the x-rays. Differential pulse height distribution measurements was obtained by a Hidex Triathler® scintillation counter with a Hamamatsu R850-photomultiplier tube and a 1  $\mu$ Ci <sup>241</sup>Am (E = 60 keV) source. The Triathler® was configured with logarithmic amplification to accentuate the difference in the differential pulse height spectra. In our measurements, the relative positions of the samples, detector and source were kept fixed, with the plated <sup>241</sup>Am source being suspended ~1 cm above power contained in a 3.7 ml glass vial. The electronic noise background was determined by measuring an empty vial in identical conditions as the nanopowder sample.

## **6.3 Results and Discussion**

### **6.3.1 Thermogravimetric Analysis (TGA) of GSO Nanoparticles**

Nanoparticles grown by the hot-solution growth (HSG) method were covered by the organic solvent, which often reduces the photoluminescence brightness. Calcining the GSO:Ce<sup>3+</sup> nanoparticles at a sufficiently high temperature will remove the oleylamine, based on thermogravimetric analysis (TGA).

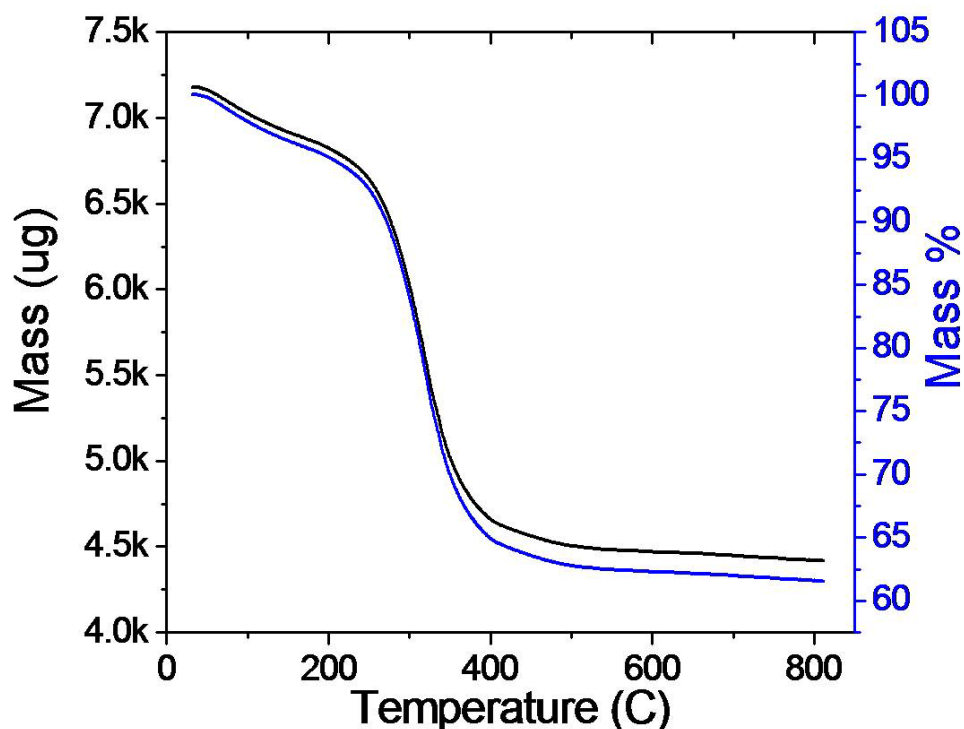


Figure 6-2. Thermogravimetric analysis (TGA) data for HSG  $\text{Gd}_2\text{SiO}_5:\text{Ce}^{3+}$  0.5% nanoparticles. Heating rate is  $10\text{ }^\circ\text{Cmin}^{-1}$ .

As shown in Figure 6-2, 37 % of the total weight was lost by heating up to  $800\text{ }^\circ\text{C}$ , with most of the weight change resulting from elimination of organic compounds by heating to approximately  $400\text{ }^\circ\text{C}$ . On the contrary,  $\text{GSO}:\text{Ce}^{3+}$  nanoparticles prepared by sol-gel (SG) method are not covered with organics, since the sol-gel synthesis did not use any surfactants .

### 6.3.2 Morphology and Structure of GSO Nanoparticles

Rare earth oxyorthosilicates ( $\text{R}_2\text{SiO}_5$ ) are reported to form two monoclinic polymorphs . The first has a  $\text{P}2_1/\text{c}$  space group and is called the  $\text{X}_1$  phase, while the second has a  $\text{C}2/\text{c}$  space group and has called the  $\text{X}_2$  phase. If R is Tb or Y, the  $\text{X}_1$  phase is formed at low temperatures and  $\text{X}_2$  at high temperatures. From La to Gd, in the

order of the periodic table, the  $X_1$  phase is formed, whereas Dy to Lu forms the  $X_2$  phase [170].

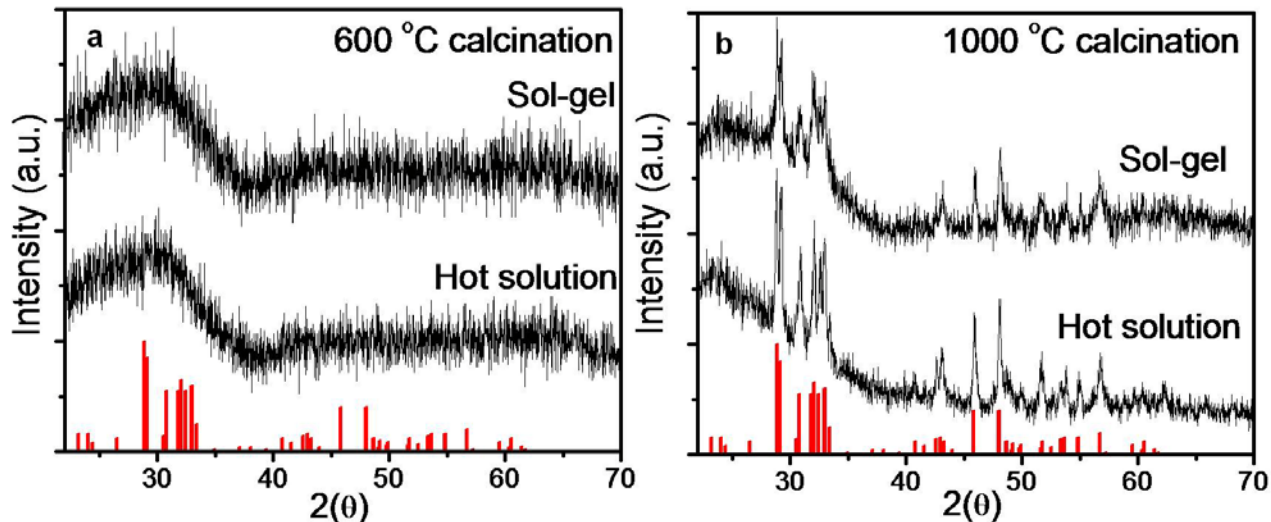


Figure 6-3. XRD patterns from  $Gd_2SiO_5:Ce^{3+}$  nanoparticles compared to the JCPDS pattern for monoclinic  $Gd_2SiO_5$  (JCPDS # : 40-0282) :  $GSO:Ce^{3+}$  nanoparticles after calcination at 600 °C and 1000 °C for 2hr in air.

In the present study, as-synthesized nanoparticles were amorphous with the typical broad XRD amorphous peak at  $\sim 27^\circ$ . Despite of calcination at 600 °C,  $GSO:Ce^{3+}$  nanoparticles from both HSG and SG remained amorphous, as shown by XRD data in Figure 6-3 (a). In contrast, the XRD spectra from both HSG and SG  $GSO:Ce^{3+}$  nanoparticles calcined at 1000 °C for 2hr were crystalline with peaks that match the JCPDS data for  $X_1$  monoclinic  $Gd_2SiO_5$  (Card 40-0287). Using the Scherrer equation, broadening of the (321) peak for both synthesis methods indicated an average nanoparticle diameter of 40-50 nm.

Figure 6-4 shows HR-TEM and Selected Area Diffraction (SAD) images of sol-gel prepared  $GSO:Ce^{3+}$  nanoparticles (a and b) and hot-solution prepared  $GSO:Ce^{3+}$

nanoparticles (c to f). These images show that the particles are slightly agglomerated after drying and calcinations.

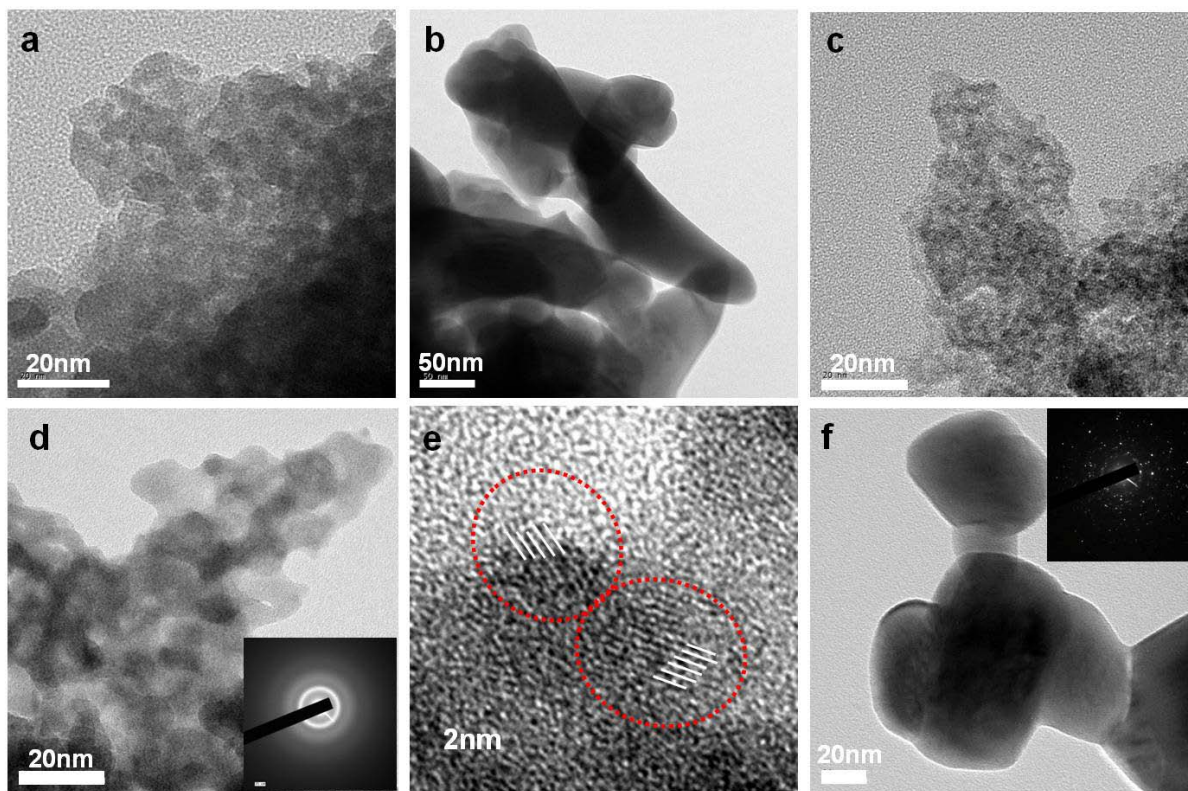


Figure 6-4. TEM images of  $Gd_2SiO_5:Ce^{3+}$  nanoparticles prepared by the sol-gel (SG) method and the hot-solution (HSG) method.

The particle size of as-synthesized  $GSO:Ce^{3+}$  nanoparticles was  $\leq 5$  nm for both synthesis methods based on TEM images (Figure 6-4 (a and b)). Figure 6-4 (c and d) show  $GSO:Ce^{3+}$  HSG nanoparticles after calcination at 600 °C. Despite the observation of only a broad amorphous XRD peak, it is possible to find lattice fringes in the high resolution image of a view of nanoparticles. An SAD image and diffraction pattern shown in Figure 6-4 (d) also suggests a fine grain size ( $< 20$  nm) with faint, broad rings before calcination. The particle size increased to  $\sim 45$  nm after calcination at 1000 °C for 2 hrs, as shown in Figure 6-4 (f), which is in reasonable agreement with sizes of 40-50 nm based on XRD peak broadening. With the SAD micrograph and diffraction pattern

inset of Figure 6-4 (f), incomplete ring patterns indicate larger crystalline grains after calcining at 1000 °C, consistent with the XRD data in Figure 6-3.

### 6.3.3 Luminescent Properties of GSO Nanoparticles

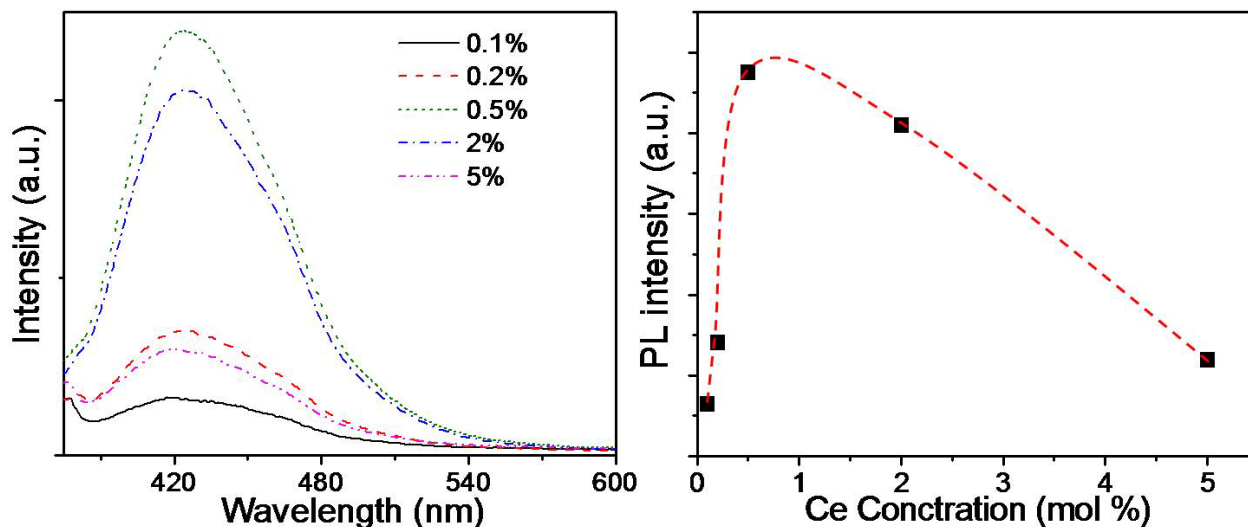


Figure 6-5. PL spectra and intensity for various Ce concentrations showing quenching for Gd<sub>2</sub>SiO<sub>5</sub>:Ce<sup>3+</sup> nanoparticles synthesized by the hot-solution method (excitation wavelength = 344 nm).

It is well known that the optimum dopant concentration in a phosphor depends on both the host and rare-earth dopants. For nanophosphors, concentration quenching behavior of photoluminescence has been reported for YSO:Eu<sup>3+</sup> [171] and Gd<sub>2</sub>O<sub>3</sub>:Eu<sup>3+</sup> [122], and the general trend is that the optimum dopant concentration in nanophosphors is much higher than for the bulk materials.

As shown in Figure 5, GSO:Ce<sup>3+</sup> nanoparticles prepared by HSG exhibited the highest PL intensity for 0.5% Ce, which is higher than that of bulk oxyorthosilicates grown by the CZ method in which the optimum concentration is generally  $\leq 0.05\%$  [172]. Figure 6-6 shows photoluminescence emission (PL) and photoluminescence excitation (PLE) spectra from calcined GSO:Ce<sup>3+</sup> nanoparticles prepared by the (a) hot-solution and (b) sol-gel methods, respectively. PL emission and excitation spectra were

measured at room temperature from nanoparticles suspended in ethanol with a quartz cuvette.

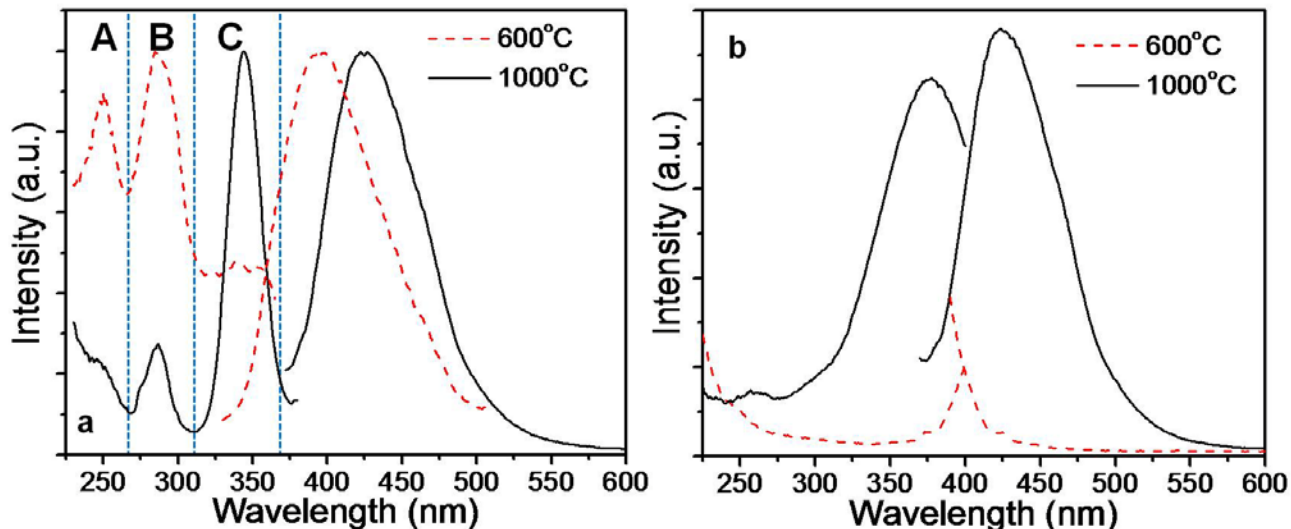


Figure 6-6. PL and PLE spectra from  $\text{Gd}_2\text{SiO}_5:\text{Ce}^{3+}$  nanoparticles calcined at 600 °C (dashed line) and 1000 °C (solid line).

$\text{GSO}:\text{Ce}^{3+}$  nanoparticles calcined at 1000 °C for both HSG and SG showed PL spectra that were very similar to spectrum from bulk single crystal  $\text{GSO}:\text{Ce}^{3+}$  [173]. The PLE spectra consisted of three bands, as shown in Figure 6-6 (a) and 6-7. Band A absorption in the higher energy region at ~240 nm results from a transition between the ground 4f level ( $^2\text{F}_{5/2}$ ) and the continuum of the conduction band.

The bands labeled B and C at ~285 and ~344 nm result from transitions from the ground  $^2\text{F}_{5/2}$  level to excited 5d ( $^2\text{E}$  or  $^2\text{T}_2$ ) levels, respectively. The PL spectrum of  $\text{GSO}:\text{Ce}^{3+}$  nanoparticles calcined at 1000 °C for two synthesis methods consists of two bands corresponding to the transitions from the lower  $^2\text{T}_2$  sublevel (5d) to  $^2\text{F}_{7/2}$  and  $^2\text{F}_{5/2}$  levels (4f), which results in a broad and asymmetric emission peak at 424 nm. The crystal structures of both HSG and SG  $\text{GSO}:\text{Ce}^{3+}$  nanoparticles calcined at 1100° C were reported above to be monoclinic, therefore the match with spectra from bulk

GSO:Ce<sup>3+</sup> is expected. GSO:Ce<sup>3+</sup> nanoparticles calcined at 600 °C, however, show PL and PLE properties different from bulk GSO:Ce<sup>3+</sup> due to lack of crystallinity.

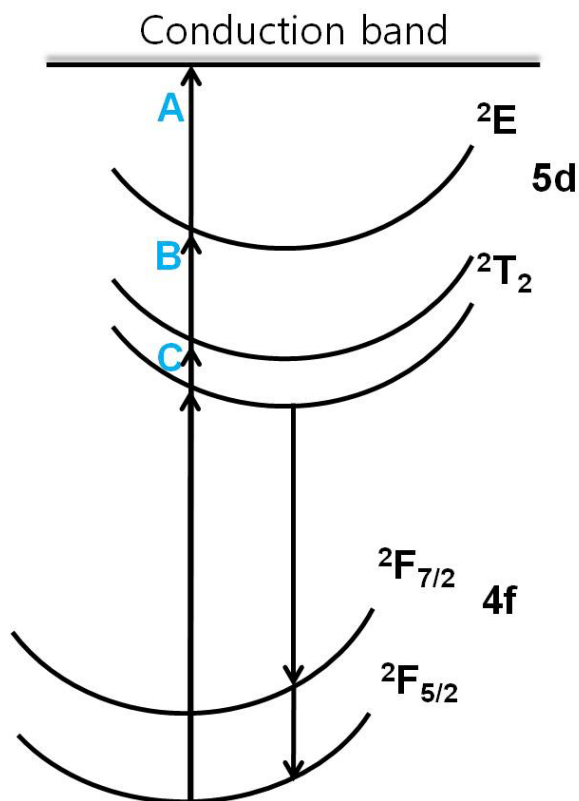


Figure 6-7. Configuration coordinate model energy levels for Ce<sup>3+</sup> ions in a Gd<sub>2</sub>SiO<sub>5</sub> host.

As shown in Figure 6-6, GSO:Ce<sup>3+</sup> nanoparticles prepared by HSG (dashed lines) and calcined at 600 °C versus 1000° C (Figure 6-6(a)) exhibit different normalized excitation band intensities and a blue shifted emission peak. In contrast, GSO:Ce<sup>3+</sup> nanoparticles prepared by SG did not show photoluminescence. The luminescent properties of Ce<sup>3+</sup> ions depend strongly on the structure of the host material through the crystal field splitting of the 5d state. For example, Ce<sup>3+</sup> in YBO<sub>3</sub> host material show a 390 nm emission peak with 254 nm excitation, while Ce<sup>3+</sup> in a GdPO<sub>4</sub> host emits at 350 nm with 280 nm excitation[174]. The difference in the PLE spectra and the live shifted emission

peak of GSO:Ce<sup>3+</sup> nanoparticles synthesized by HSG presumably result from changes in the crystal field of the Ce<sup>3+</sup> ions in the GSO host. On the other hand, the Ce<sup>3+</sup> ions in SG GSO:Ce<sup>3+</sup> nanoparticles did not emit after calcining at 600 °C calcinations due to the amorphous host.

### 6.3.4 X-ray Luminescence of GSO Nanoparticles

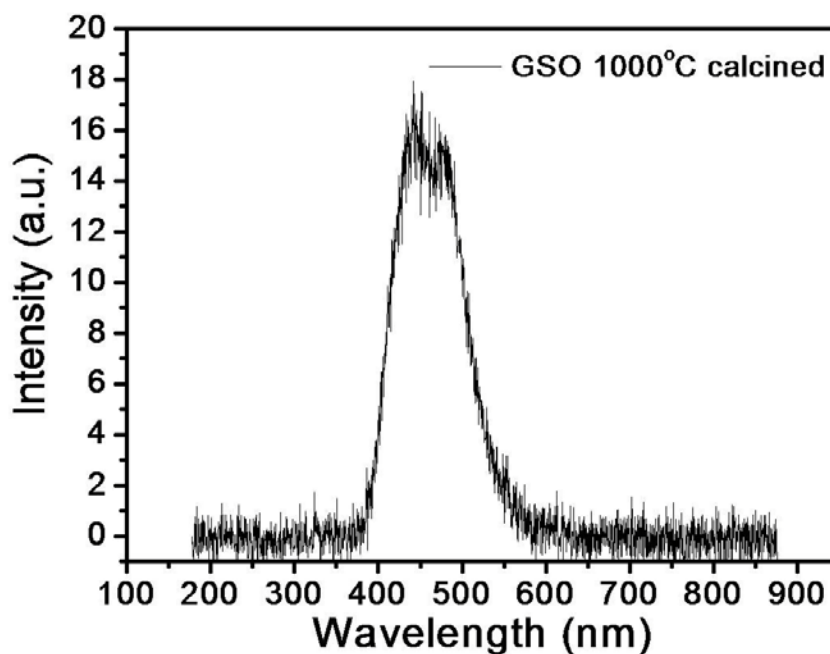


Figure 6-8. X-ray luminescence spectrum of calcined Gd<sub>2</sub>SiO<sub>5</sub>:Ce<sup>3+</sup> nanoparticles.

Figure 6-8 shows the XL spectrum from HSG GSO:Ce<sup>3+</sup> nanoparticles calcined at 1000 °C and irradiated by 40 keV X-rays. The spectrum is dominated by the same 5d-4f peak at 424 nm as for the PL spectrum shown in Figure 5 a. Several X-ray and radioluminescence materials have been already developed, such as NaI, but may have undesirable properties, such as poor high temperature drift effects [175]. In this study, a good X-ray luminance of 2300 Photons/MeV was observed for GSO:Ce<sup>3+</sup> nanoparticles synthesized HSG, which compares favorably to a typical value of 7000 Photons/MeV of single crystal detectors [176].

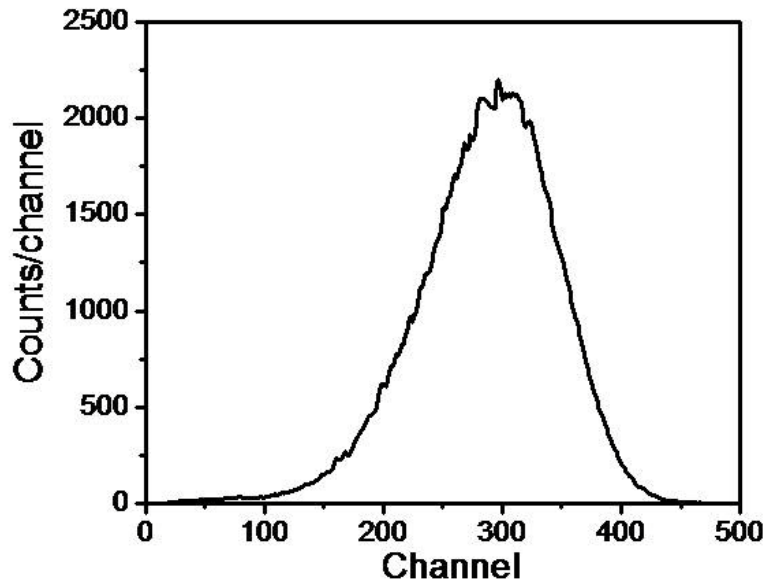


Figure 6-9. Differential pulse height spectrum of calcined GSO:Ce<sup>3+</sup> nanoparticles by an <sup>241</sup>Am source showing a broad scintillation response centered at approximately channel 300.

The scintillation property of GSO:Ce<sup>3+</sup> under  $\gamma$ -ray irradiation was tested using americium (<sup>241</sup>Am) source. Figure 6-9 shows the differential pulse height spectra from calcined GSO:Ce<sup>3+</sup> nanoparticles. The scintillation response of GSO:Ce<sup>3+</sup> nanoparticles under <sup>241</sup>Am irradiation determined by means of differential pulse height distribution measurements is shown in Figure 6-9 after the subtraction of the electronic noise, where a photo-peak centered around channel (average pulse amplitude) 300 can be observed.

#### 6.4 Conclusion

Gd<sub>2</sub>SiO<sub>5</sub>:Ce<sup>3+</sup> nanoparticles were synthesized by a sol-gel and a hot-solution method. As-synthesized nanoparticles did not exhibit photoluminescence. After elimination of residual organic compounds from the growth by calcining at 600 °C, hot-solution grown GSO:Ce<sup>3+</sup> nanoparticles exhibited PL and PLE spectra that were different from nanoparticles calcined at 1000°C and from a bulk GSO:Ce<sup>3+</sup>.

Nanoparticles prepared by the sol-gel method did not crystallize at 600°C, but require calcination at 1000°C before exhibiting PL and PLE spectra. 40 kV X-rays produced at a luminance of 2300 photons/MeV from the same 5d-4f transitions at 424 nm as the PL spectra . These data show the promise of nanoparticles for scintillation detectors.

## CHAPTER 7 CONCLUSIONS

### **7.1 Shape Controlled Two Dimensional Gd<sub>2</sub>O<sub>3</sub>:Eu<sup>3+</sup> Colloidal Nanocrystals Grown by Hot-Solution Method**

In this chapter, Eu<sup>3+</sup> doped Gd<sub>2</sub>O<sub>3</sub> nanoparticles were synthesized by a non-hydrolytic hot-solution method. The shape of Gd<sub>2</sub>O<sub>3</sub>:Eu<sup>3+</sup> nanoparticles were varied from clover to platelet and spherical by adding pre-heating process and by using different reaction times. Potential mechanisms leading to various shapes of Gd<sub>2</sub>O<sub>3</sub>:Eu<sup>3+</sup> nanoparticles were discussed and explained by a Lamer plot. By controlling reaction parameters, the quantum yield of Gd<sub>2</sub>O<sub>3</sub>:Eu<sup>3+</sup> nanoparticles also varied from 9 % to 67 %. The 40 keV X-rays produced an X-ray luminance from the same <sup>5</sup>D<sub>0</sub>-<sup>7</sup>F<sub>2</sub> transitions from Eu<sup>3+</sup> at 612 nm. These data show the promise of nanoparticles for scintillation detectors.

### **7.2 Enhanced Photoluminescence from Gd<sub>2</sub>O<sub>3</sub>:Eu<sup>3+</sup> Nanocores with Y<sub>2</sub>O<sub>3</sub> Thin Shell**

Gd<sub>2</sub>O<sub>3</sub>:Eu<sup>3+</sup> nanocores of 21 nm diameter and Y<sub>2</sub>O<sub>3</sub> thin shell were synthesized by a facile polyol method. The thickness of Y<sub>2</sub>O<sub>3</sub> shell could be controlled by the different ratio of precursors. The thickness of Y<sub>2</sub>O<sub>3</sub> layers was calculated by using the attenuation length of photoelectrons from X-ray photoelectron spectroscopy. Based on XRD and XPS results, Y<sub>2</sub>O<sub>3</sub> co-precipitated nanoparticles also formed with Gd<sub>2</sub>O<sub>3</sub>:Eu<sup>3+</sup>/Y<sub>2</sub>O<sub>3</sub> core/shell structures. After calcinations at 600 °C and 2 hr in air, crystalline Y<sub>2</sub>O<sub>3</sub> shells up to 0.6 nm thick were grown on Gd<sub>2</sub>O<sub>3</sub>:Eu<sup>3+</sup> cores. As the thickness of Y<sub>2</sub>O<sub>3</sub> shell increased, the PL intensity and luminescence decay lifetime were larger by a portion by 40 % and 11 %, respectively. The enhanced PL intensity

was attributed to passivation of surface defect states that reduced the rates of non-radiative relaxation process.

### **7.3 Enhanced Photoluminescence from Eu Doped Gd<sub>2</sub>O<sub>3</sub> Based Core/Dual-Shell Nanoparticles**

Core/dual-shell heterostructures with mono-dispersed 420 nm SiO<sub>2</sub> cores, ~5 nm Gd<sub>2</sub>O<sub>3</sub>:Eu<sup>3+</sup> inner shell and 43 nm Y<sub>2</sub>O<sub>3</sub> outer shell were prepared by solution precipitation method. The uniform coverage of the Gd<sub>2</sub>O<sub>3</sub>:Eu<sup>3+</sup> shell and its thickness were characterized by TEM and XPS. Photoluminescence (PL) of SiO<sub>2</sub>/Gd<sub>2</sub>O<sub>3</sub>:Eu<sup>3+</sup> core/single-shell structures showed the red emission from Eu<sup>3+</sup> by the <sup>5</sup>D<sub>0</sub>-<sup>7</sup>F<sub>2</sub> transition at 612 nm and their quantum yield (QY) was ~12 % after calcination at 600 °C for 2 hr in air. The core/dual-shell nanoparticles with crystalline Y<sub>2</sub>O<sub>3</sub> outer shell increased the QY to 20 %. Since a large fraction of the atoms are located in the surface region of nanoparticles, it is critical to passivate nanoparticles with an outer shell. Passivation increased the PL intensity as indicated by 71 % longer luminescent decay lifetimes.

### **7.4 X-RAY and Photo-Luminescence from Gd<sub>2</sub>SiO<sub>5</sub>:Ce<sup>3+</sup> Nanoparticles Synthesized by Solution Based Methods**

Cerium doped gadolinium silicate Gd<sub>2</sub>SiO<sub>5</sub>:Ce<sup>3+</sup> (GSO:Ce<sup>3+</sup>) nanoparticles were successfully synthesized by solution based methods, such as hot solution growth (HSG) and sol-gel method. As synthesized spherical particles were amorphous and their diameter was ~ 5 nm. HSG GSO:Ce<sup>3+</sup> nanoparticles after calcination at 600 °C exhibited PL and PLE spectra which were different from bulk counterparts. PL spectra of calcined GSO nanocrystals at 1000 °C, synthesized by both methods, showed a broad emission band with the peak at 420 nm associated with the Ce<sup>3+</sup> ions 5d-4f transition, similar to a GSO:Ce<sup>3+</sup> single crystal. Radioluminescence of GSO:Ce<sup>3+</sup> nanocrystals excited by 40 kV X-rays produced 2300 photons/MeV. Excitation by a

$^{241}\text{Am}$  59 keV gamma ray source resulted in a scintillation peak centered at channel number 290 with a FWHM of 180 channels.

## CHAPTER 8 FUTURE WORK

Based on the results of this research, it is evident that highly efficient luminescent nanoparticles for scintillators can be synthesized through controlled growth and/or surface modification of nanoparticles. In terms of light output from scintillation detectors, which is composed of nanocomposites with matrix and nanoparticles, reduction of light scattering by nanoparticles is as important as enhancement of yield of nanocomposites. Therefore, novel ideas for reducing scattering for nanocomposites with nanoparticles and a matrix are required. The mechanisms leading to different light intensities from UV versus radioactive particles should be investigated for better detectors. In addition, to get a better stopping power, it is required to have larger volume of nanoparticles rather than thin layers. Therefore,  $\text{Bi}_2\text{O}_3$  cores, which have high atomic number, should be used as luminescent centers to absorb high energy particles and core/shell structures will be applied for less light scattering.

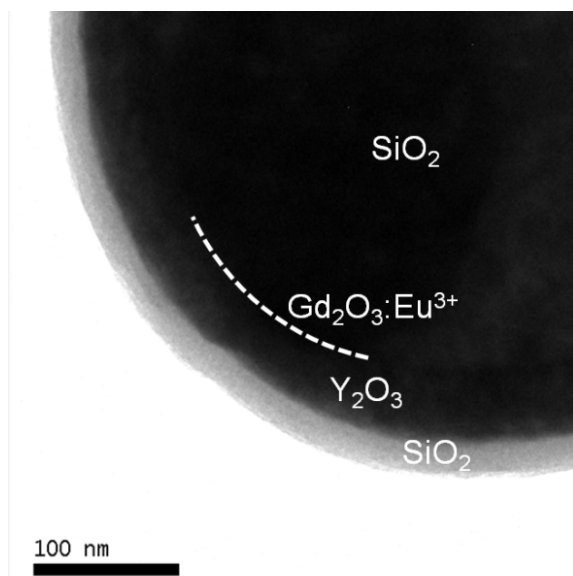


Figure 8-1.  $\text{SiO}_2/\text{Gd}_2\text{O}_3:\text{Eu}^{3+}/\text{Y}_2\text{O}_3/\text{SiO}_2$  core/multi-shell nanoparticles

## LIST OF REFERENCES

1. D.H. Chen and C.H. Hsieh, *J. Mater. Chem.* 12 (2002) 2412.
2. Z. Gui, R. Fan, W. Mo, X. Chen, L. Yang, and Y. Hu, *Mater. Res. Bull.* 38 (2003) 169.
3. T. Yonezawa, M. Sutoh, and T. Kunitake, *Chem. Lett.* 619 (1997)
4. I. Sondi, D.V. Goia, and E.J. Matijevic, *J. Colloid Interface Sci.* 260 (2003) 75.
5. Y. Tan, X. Dai, Y. Li, and D. Zhu, *J. Mater. Chem.* 13 (2003) 1069.
6. Z.L. Liu, Y.J. Liu, K.L. Yao, Z.H. Ding, J. Tao, and X. Wang, *Journal of Materials Synthesis and Processing* 10 (2002) 83.
7. B.L. Cushing, V.L. Kolesnichenko, and C.J. O'Connor, *Chem. Rev.* 104 (2004) 3893.
8. K. Nishiwaki, N. Kakuta, A. Ueno, and H. Nakabayashi, *J. Catal.* 118 (1989) 498.
9. B.L. Bischoff and M.A. Anderson, *Chem. Mater.* 7 (1995) 1772.
10. M. Niederberger, M.H. Bartl, and G.D. Stucky, *Chem. Mater.* 14 (2002) 4364.
11. T.P. Hoar and J.H. Schulman, *Nature* 152 (1943) 102.
12. J.H. Schulman and D.P. Riley, *J. Colloid Sci.* 3 (1948) 383.
13. Y.-X. Pang and X. Bao, *J. Mater. Chem.* 12 (2002) 3699.
14. P.D. Moran, J.R. Bartlett, G.A. Bowmaker, J.L. Woolfrey, and R.P. Cooney, *J. Sol-Gel Sci. Technol.* 15 (1999) 251.
15. Z. Wu, J. Zhang, R.E. Benfield, Y. Ding, D. Grandjean, Z. Zhang, and J. Xin, *J. Phys. Chem. B* 106 (2002) 4569.
16. H.S. Lee, W.C. Lee, and T. Furubayashi, *J. Appl. Phys.* 85 (1999) 5231.
17. N. Moumen, P. Bonville, and M.P. Pileni, *Journal of Physical Chemistry* 100 (1996) 14410.
18. M.L. Steigerwald, A.P. Alivisatos, J.M. Gibson, T.D. Harris, R. Kortan, A.J. Muller, A.M. Thayer, T.M. Duncan, D.C. Douglass, and L.E. Brus, *Journal of the American Chemical Society* 110 (1988) 3046.

19. X. Peng, M.C. Schlamp, A.V. Kadavanich, and A.P. Alivisatos, *J. Am. Chem. Soc.* 119 (1997) 7019.
20. J. Park, E.A. Kang, C.J. Bae, J.G. Park, H.J. Noh, J.Y. Kim, J.H. Park, J.H. Park, and T. Hyeon, *Journal of Physical Chemistry B* 108 (2004) 13594.
21. J.W. Grebinski, K.L. Richter, J. Zhang, T.H. Kosel, and M. Kuno, *Journal of Physical Chemistry B* 108 (2004) 9745.
22. V.F. Puntès, K.M. Krishnan, and A.P. Alivisatos, *Science* 291 (2001) 2115.
23. H. Yu, M. Chen, P.M. Rice, S.X. Wang, R.L. White, and S.H. Sun, *Nano Letters* 5 (2005) 379.
24. C.B. Murray, M. Nirmal, D.J. Norris, and M.G. Bawendi, *Zeitschrift Fur Physik DAtoms Molecules and Clusters* 26 (1993) S231.
25. S. Seo, H. Yang, and P.H. Holloway, *J. Colloid Interface Sci.* 331 (2009) 236.
26. S.-H. Kan, T. Mokari, E. Rothenberg, and U. Banin, *Nature Mater.* 2 (2003) 155.
27. W.E. Buhro and V.L. Colvin, *Nature Mater.* 2 (2003) 138.
28. W.H. Qi and M.P. Wang, *Journal of Nanoparticle Research* 7 (2005) 51.
29. O. Song and Z.J. Zhang, *Journal of the American Chemical Society* 126 (2004) 6164.
30. M. Yin, Y. Gu, I.L. Kuskovsky, T. Andelman, Y. Zhu, G.F. Neumark, and S. O'Brien, *Journal of the American Chemical Society* 126 (2004) 6206.
31. P.D. Cozzoli, M.L. Curri, A. Agostiano, G. Leo, and M. Lomascolo, *Journal of Physical Chemistry B* 107 (2003) 4756.
32. T.-K. Tseng, J. Choi, L.G. Jacobsohn, E. Yukihara, M. Davidson, and P.H. Holloway, *Applied Physics A: Materials Science & Processing* 100 (2010) 1137.
33. S. Ramanathan, S. Patibandla, S. Bandyopadhyay, J.D. Edwards, and J. Anderson, *J. Mater. Sci.: Mater. Electron* 17 (2006) 651.
34. X.G. Peng, L. Manna, W.D. Yang, J. Wickham, E. Scher, A. Kadavanich, and A.P. Alivisatos, *Nature* 404 (2000) 59.
35. R. Si, Y.-W. Zhang, L.-P. You, and C.-H. Yan, *Angew. Chem. Int. Ed.* 44 (2005) 3256.

36. T.A. Ring, *Fundamentals of Ceramic Powder Processing and Synthesis*; Academic Press: San Diego, CA (1996)
37. A.E. Nielsen, *Kinetics of Precipitation*; Pergamon Press: Oxford (1964)
38. H. Furedi-Milhofer, *Pure Appl. Chem.* 53 (1981) 2041.
39. D.A. Porter and K.E. Easterling, *Phase Transformations in Metals and Alloys*, Second Edition, Chapman & Hall (1992)
40. G. Madras and B.J. McCoy, *J. Chem. Phys.* 117 (2002) 8042.
41. G. Oskam, Z. Hu, R.L. Penn, N. Pesika, and P.C. Searson, *Phys. Rev. E* 66 (2002) 011403.
42. V.K. LaMer and R.H. Dinegar, *J. Am. Chem. Soc.* 72 (1950) 4847.
43. J. Park, *Angew. Chem. Int. Ed.* 46 (2007) 4630.
44. J.W. Mullin, *Crystallization*, Butterworth-Heinemann, Woburn, MA (1997)
45. A. Tao, P. Sinsermsuksakul, and P. Yang, *Angew. Chem. Int. Ed.* 45 (2006) 4597.
46. X. Peng, *Adv. Mater.* 15 (2003) 459.
47. G. Blasse and B.C. Grabmaier, *Luminescent Materials* Springer-Verlag, Berlin (1994)
48. H. Yang, C. Li, Y. Tao, J. Xu, G. Zhang, and Q. Su, *Journal of Luminescence* 126 (2007) 196.
49. T. Kano, *Phosphor Handbook*, ed. S. Shionoya and W. M. Yen, CRC Press, Boca Raton, Florida, (1998) p. 191.
50. S.Y. Seo, K.S. Sohn, H.D. Park, and S. Lee, *Journal of the Electrochemical Society* 149 (2002) H12.
51. H. Meyssamy, K. Riwozki, A. Kornowski, S. Naused, and M. Haase, *Advanced Materials* 11 (1999) 840.
52. F. Vetrone, J.C. Boyer, J.A. Capobianco, A. Speghini, and M. Bettinelli, *Chemistry of Materials* 15 (2003) 2737.
53. J. Hu, L.-s. Li, W. Yang, L. Manna, L.-w. Wang, and A.P. Alivisatos, *Science* 292 (2001) 2060.
54. S. Shionoya, *Phosphor Handbook*, ed. S. Shionoya and W. M. Yen, CRC Press, Boca Raton, Florida, (1998) p. 7.

55. C. Feldmann, T. Jtel, C.R. Ronda, and P.J. Schmidt, *Adv. Funct. Mater.* 13 (2003) 511.
56. H. Henning, *Angew. Chem. Int. Ed.* 48 (2009) 3572.
57. H. Chander, *Materials Science and Engineering: R: Reports* 49 (2005) 113.
58. U. Kaufmann, M. Kunzer, K. Kohler, H. Obloh, W. Pleschen, P. Schlotter, J. Wagner, A. Ellens, W. Rossner, and M. Kobuschi, *Phys. Status Solidi A* 192 (2002) 246.
59. S. Nakamura and G. Fasol, *The Blue Laser Diode*, Springer, Berlin (1997)
60. D. Bera, S. Maslov, L. Qian, J.S. Yoo, and P.H. Holloway, *Journal of Display Technology* 6 (2010) 645.
61. A. Henning and D. Höpfe, *Angewandte Chemie International Edition* 48 (2009) 3572.
62. K. Kohmoto, *Phosphor Handbook*, ed. S. Shionoya and W. M. Yen, CRC Press, Boca Raton, Florida, (1998) p. 361.
63. A.n. Sigma Aldrich - *Detectors in Nuclear Medical Imaging - High Purity Crystals for Scintillation*,
64. P. Lecoq, A. Annenkov, A. Gektin, M. Korzhik, and C. Pedrini, *Inorganic Scintillators for Detector Systems*, Springer (2006)
65. A. Lushchik, M. Kirm, C. Lushchik, I. Martinson, and G. Zimmerer, *J. Lumin.* 87-89 (2000) 232.
66. P.A. Rodnyi, P. Dorenbos, and C.W.E.v. Eijk, *Phys. Status Solidi B* 187 (1995) 29.
67. A.N. Vasil'ev, *Nucl. Instr. Meth. Phys. Res. B* 107 (1996) 165.
68. R.H. Bertram and A. Lempicki, *J. Lumin.* 68 (1996) 225.
69. C.V. Eijk, *Inorganic-scintillator requirements*, in record of the Int. Workshop Physical Processes in Fast Scintillator, Stratech Report TUD, Delft, The Netherlands (1994)
70. P. Lecomte, D. Luckey, F. Nessi-Tedaldi, F. Pauss, and D. Renker, *Nuclear Instruments & Methods in Physics Research, Section A: Accelerators, Spectrometers, Detectors, and Associated Equipment* 587 (2008) 266.
71. P.J. Shlichta, in *Nuclear Science Symposium Conference Record*, IEEE p.367. (2001)

72. T.M. Blodgett, C.C. Meltzer, and D. W. Townsend, *Radiology* 242 (2007) 360.
73. C.M.L. West, T. Jones, and P. Price, *Nature Reviews Cancer* 4 (2004) 457.
74. C.L. Melcher and J.S. Schweitzer, *Nucl. Instr. Meth. Phys. Res.* 314 (1992) 212.
75. Y. Masumoto, *Phosphor Handbook*, ed. S. Shionoya and W. M. Yen, CRC Press, Boca Raton, Florida (1998) p. 72.
76. A.P. Alivisatos, *Science* 271 (1996) 933.
77. J. Lefebvre, P.J. Poole, J. Fraser, G.C. Aers, D. Chithrani, and R.L. Williams, *Journal of Crystal Growth* 234 (2002) 391.
78. Q. Pang, L. Zhao, Y. Cai, D.P. Nguyen, N. Regnault, N. Wang, S. Yang, W. Ge, R. Ferreira, G. Bastard, and J. Wang, *Chemistry of Materials* 17 (2005) 5263.
79. A.G. Rolo, M.I. Vasilevskiy, N.P. Gaponik, A.L. Rogach, and M.J.M. Gomes, *Physica Status Solidi B: Basic Research* 229 (2002) 433.
80. C.B. Murray, D.J. Norris, and M.G. Bawendi, *J. Am. Chem. Soc.* 115 (1993) 8706.
81. I. Yu, T. Isobe, and M. Senna, *Journal of Physics and Chemistry of Solids* 57 (1996) 373.
82. D.R. Vij, *Luminescence of Solids* (Plenum Press, New York) (1988)
83. R.N. Bhargava, D. Gallagher, X. Hong, and A. Nurmikko, *Phys. Rev. Lett.* 72 (1994) 416.
84. M. Ihara, T. Igarashi, T. Kusunoki, and K. Ohno, *J. Electrochem. Soc.* 149 (2002) H72.
85. U. Kolitsch, H.J. Seifert, and F. Aldinger, *J of Alloys and Compounds* 257 (1997) 104.
86. A.M. Pires, M.F. Santos, M.R. Davolos, and E.B. Stucchi, *J of Alloys and Compounds* 344 (2002) 276.
87. B.L. Abrams and P.H. Holloway, *Chem. Rev* 104 (2004) 5783.
88. H. Yang and P.H. Holloway, *Appl. Phys. Lett.* 82 (2003) 1965.
89. M.A. Hines and P. GnyotSionnest, *J. Phys. Chem.* 100 (1996) 468.

90. B.O. Dabbousi, J. RodriguezViejo, F.V. Mikulec, J.R. Heine, H. Mattoussi, R. Ober, K.F. Jensen, and M.G. Bawendi, *J. Phys. Chem. B* 101 (1997) 9463.
91. K. Song and S. Lee, *Curr. Appl. Phys.* 1 (2001) 169.
92. C.F. Hoener, K.A. Allan, A.J. Bard, A. Campion, M.A. Fox, T.E. Mallouk, S.E. Webber, and J.M. White, *J. Phys. Chem.* 96 (1992) 3812.
93. A.R. Kortan, R. Hull, R.L. Opila, M.G. Bawendi, M.L. Steigerwald, P.J. Carroll, and L.E. Brus, *J. Am. Chem. Soc.* 112 (1990) 1327.
94. P. Reiss, J. Bleuse, and A. Pron, *Nano Lett.* 2 (2002) 781.
95. M. Chang and S. Tie, *Nanotechnology* 19 (2008) 075711.
96. M. Darbandi, W. Hoheisel, and T. Nann, *Nanotechnology* 17 (2006) 4168.
97. G. Pan, H. Song, X. Bai, L. Fan, H. Yu, Q. Dai, B. Dong, R. Qin, S. Li, S. Lu, X. Ren, and H. Zhao, *J. Phys. Chem. C* 111 (2007) 12472.
98. G.H. Pan, H.W. Song, X. Bai, Z.X. Liu, and H.Q. Yu, *Chem. Mater.* 18 (2006) 4526.
99. M. Yu, J. Lin, and J. Fang, *Chem. Mater.* 17 (2005) 1783.
100. H. Zhu and D. Zuo, *The Journal of Physical Chemistry C* 113 (2009) 10402-10406.
101. F. Wang, Y. Zhang, X. Fan, and M. Wang, *Nanotechnology* 17 (2006) 1527.
102. K.W. Kramer, P. Dorenbos, H.U. Gudel, and C.W.E.v. Eijk, *J. Mater. Chem.* 16 (2006) 2773.
103. S. Srivastava and N.A. Kotov, *Soft Matter* 5 (2009) 1146.
104. E.V. Shevchenko, D.V. Talapin, A.L. Rogach, A. Kornowski, M. Haase, and H. Weller, *J. Am. Chem. Soc.* 124 (2002) 11480.
105. B. Pietrobon, M. McEachran, and V. Kitaev, *ACS Nano* 3 (2009) 21.
106. C. Burda, X. Chen, R. Narayanan, and M.A. El-Sayed, *Chem. Rev.* 105 (2005) 1025.
107. Z.W. Pan, Z.R. Dai, and Z.L. Wang, *Science* 291 (2001) 1947.
108. Y. Zhang, G. Li, and L. Zhang, *Chem. Lett.* 33 (2004) 334.

109. M.-P. Pileni, *Nat. Mater.* 2 (2003) 145.
110. V. Polshettiwar, B. Baruwati, and R.S. Varma, *ACS Nano* 3 (2009) 728.
111. A.K. H. Meyssamy K. Riwozki, S. Naused and M. Haase, *Advanced Materials* 11 (1999) 840.
112. H.S. Yang, H. Lee, and P.H. Holloway, *Nanotechnology* 16 (2005) 2794.
113. M. Yada, M. Mihara, S. Mouri, M. Kuroki, and T. Kijima, *Advanced Materials* 14 (2002) 30971.
114. T.-K. Tseng, J. Choi, L.G. Jacobsohn, E.D. Yukihiro, Mark, and P.H. Holloway, *Applied Physics A: Materials Science & Processing* 100 (2010) 1137.
115. M. Bruchez, M. Moronne, P. Gin, S. Weiss, and A.P. Alivisatos, *Science* 281 (1998) 2013.
116. W.C.W. Chan and S.M. Nie, *Science* 281 (1998) 2016.
117. Z. Huang, P. Thomson, and S. Di, *Journal of Physics and Chemistry of Solids* 68 (2007) 530.
118. G. Brauer, *Handbook of Preparative Inorganic Chemistry*, second ed., Academic Press, New York, (1963)
119. H. Chen, J. Zhang, X. Wang, S. Gao, M. Zhang, Y. Ma, Q. Dai, D. Li, S. Kan, and Guangtian Zou, *Journal of Colloid and Interface Science* 297 (2006) 130.
120. H.E. Hoefdraad, *J. Solid State Chem.* 15 (1975) 175.
121. J. Heber, K.H. Hellwege, U. Kobler, and H. Murmann, *Z. Phys.* 237 (1970) 189.
122. J. Choi, T.-K. Tseng, M. Davidson, and P.H. Holloway, *J. Mater. Chem.* 21 (2011) 3113.
123. H. Zhu and D. Zuo, *J. phys. Chem. C* 113 (2009) 10402.
124. J. Dexpertghys, M. Faucher, and P. Caro, *Phys. Rev. B* 23 (1981) 607.
125. S.C. Erwin, L. Zu, M.I. Haftel, A.L. Efros, T.A. Kennedy, and D.J. Norris, *Nature* 436 (2005) 91.
126. A.P. Alivisatos, K.P. Johnson, X. Peng, T. Wilson, C.J. Loweth, M.P.B. Jr, and P.G. Schultz, *Nature (London)* 382 (1996) 609.

127. G.C. Kim, S.I. Mho, and H.L. Park, *J. Mater. Sci. Lett* 51 (1995) 107.
128. L. Ozawa, *Mater. Chem. Phys.* 51 (1997) 107.
129. M.H. Lee, S.G. Oh, S.C. Yi, D.S. Seo, and J.S. Yoo, *J. Electrochem. Soc.* 147 (2000) 3139.
130. A.G. Macedo, D. Ananias, P.S. Andre, R.A.S. Ferreira, A.L. Kholkin, L.D. Carlos, and J. Rocha, *Nanotechnology* 19 (2008) 295702.
131. W. Bu, Z. Hua, H. Chen, and J. Shi, *J. Phys. Chem. B* 109 (2005) 14461.
132. G. Liu, G. Hong, and D. Sun, *J. Colloid Interface Sci.* 278 (2004) 133.
133. D.V. Talapin, A.L. Rogach, A. Kornowski, M. Haase, and H. Weller, *Nano Lett.* 1 (2001)
134. L. Manna, E.C. Scher, L.S. Li, and A.P. Alivisatos, *J. Am. Chem. Soc.* 124 (2002) 7136.
135. F. Fievet, *Surfactant Sci. Ser.* 92 (2000) 460.
136. H. Yang and Y. Kim, *J. Lumin.* 128 (2008) 1570.
137. Z.L. Wang, Z.W. Quan, P.Y. Jia, C.K. Lin, Y. Luo, Y. Chen, J. Fang, W. Zhou, C.J. O'Conner, and J. Lin, *Chem. Mater.* 18 (2006) 2030.
138. Y.W. Cao and U.J. Banin, *J. Am. Chem. Soc.* 122 (2000) 9692.
139. P.H. Holloway, *J. Vac. Sci. Technol. (N. Y., NY, U. S.),* (1975) 392.
140. C.J. Powell, *Surf. Sci.* 44 (1974) 29.
141. W.W. Zhang, W.P. Zhang, P.B. Xie, M. Yin, H.T. Chen, L. Jing, Y.S. Zhang, L.R. Lou, and S.D. Xia, *J. Colloid Interface Sci.* 262 (2003) 588.
142. G. Wakefield, H.A. Keron, P.J. Dobson, and J.L. Hutchison, *J. Colloid Interface Sci.* 215 (1999) 179.
143. C. Louis, R. Bazzi, M.A. Flores, W. Zhang, K. Lebbou, O. Tillement, B. Mercier, C. Dujardin, and P. Perriat, *J. Solid State Chem.* 173 (2003) 335.
144. J. Li, X. Li, X. Sun, and T.J. Ishigaki, *J. Phys. Chem. C* 112 (2008) 11707.
145. T. Tseng, J. Choi, M. Davidson, and P.H. Holloway, *J. Mater. Chem.* 20 (2010) 6111.
146. D.K. Williams, H. Yuan, and B.M. Tissue, *J. Lumin.* 83 (1999) 297.

147. J.K. Park, K.N. Kim, P.K. Bae, J.H. Lee, C.H. Han, and C.H. Kim, *Electrochem. Solid-State Lett.* 10 (2007) J97.
148. E. Nakazawa, *Phosphor Handbook*, ed. S. Shionoya and W. M. Yen, CRC Press, Boca Raton, Florida, (1998) p. 85.
149. D.R.G.J.D. Bryan, *Prog. Inorg. Chem.* pp. 47-126 (2005)
150. L. Qian, D. Bera, T.-K. Tseng, and P.H. Holloway, *Appl. Phys. Lett.* 94 (2009) 073112.
151. G. Bonnet, M. Lachkar, J.P. Larpin, and J.C. Colson, *Solid States Ionics* 72 (1994) 344.
152. G. Bonnet, M. Lachkar, J.P. Larpin, and J.C. Colson, *Thin Solid Film* 261 (1995) 31.
153. M. Yu, J. Lin, and J. Fang, *Chem. Mater.* 17 (2005) 1783.
154. D.Y. Kong, M. Yu, C.K. Lin, X.M. Liu, J. Lin, and J. Fang, *J. Electrochem. Soc.* 152 (2005) H146.
155. W. Stöber, A. Fink, and E. Bohn, *J. Colloid Interface Sci.* 26 (1968) 62.
156. Y. Huang and J.E. Pemberton, *colloids and surfaces A* 360 (2010) 175.
157. A.K.V. Helden, J.W. Jansen, and A. Vrij, *J. Colloid Interface Sci.* 81 (1981) 354.
158. C.J. Powell, Surface and Microanalysis Science Division, National Institute of Standards and Technology, Gaithersburg, MD 20899, USA
159. L. Porres, A. Holland, L.-O. Palsson, A. Monkman, C. Kemp, and A. Beeby, *J. Fluoresc.* 16 (2006) 267.
160. L.-O. Pålsson and A. Monkman, *Adv. Mater.* 14 (2002) 757.
161. S. Li, H. Song, H. Yu, S. Lu, X. Bai, G. Pan, Y. Lei, L. Fan, and T. Wang, *Journal of Luminescence* 122 (2007) 876.
162. Z. Deng, L. Cao, F. Tang, and B. Zou, *J. Phys. Chem. B* 109 (2005) 16671.
163. C. Li, C. Wyon, and R. Moncorge, *IEEE J. Quant. Electron.* 28 (1992) 1209.
164. T.E. Peters, *J. Electrochem. Soc.* (1969) 985.
165. M. Kobayashi and M. Ishii, *Nucl. Instr. Meth. B* 61 (1994) 591.

166. H. Ishibashi and Y.K.e. al., Crystal 2000 Proc. Int. Workshop (1993) p. 389.
167. T. Ye, G.W. Zhao, and W.P. Zhang, Mter. Res. Bull. 32 (1997) 501.
168. M.D. Dramicanin, V. Jokanovic, B. Vian, E. Antic-Fidancev, M. Mitric, and Z. Andric, J of Alloys and Compounds 424 (2006) 213.
169. R.E. Muenchausen, E.A. McKigney, L.G. Jacobsohn, M.W. Blair, B.L. Bennett, and D.W. Cooke, IEEE Transactions on Nuclear Science 55 (2008) 1532.
170. M.D. Dramicanin, B. Vian, Z. Andric, V. Djokovic, and A.S. Luyt, J of Alloys and Compounds 464 (2008) 357.
171. W. Zhang, P. Xie, C. Duan, K. Yan, M. Yin, L. Lou, S. Xia, and J.C. Krupa, Chem. Phys. Lett. 292 (1998) 133.
172. D.W. Cooke, K.J. McClellan, B.L. Bennett, J. M. Roper, M.T. Whittaker, R.E. Muenchausen, and R.C. Sze, J. Appl. Phys. 88 (2000) 7360.
173. M. Sekita, Y. Miyazawa, T. Akahane, and T. Chiba, J. Appl. Phys. 66 (1989) 373.
174. S. Tanimizu, Phosphor Handbook, ed. S. Shionoya and W. M. Yen, CRC Press, Boca Raton, Florida (1998) p. 186.
175. M.S. Zucker, Nuclear Instruments and Methods in Physics Research Section A: Accelerators, Spectrometers, Detectors and Associated Equipment 242 (1986) 306.
176. G.M. Onyshchenko, L.L. Nagornaya, V.G. Bondar, Y. Borodenko, O.V. Zelenskaya, E.N. Pirogov, and V.D. Ryzhikov, Nuclear Instruments and Methods in Physics Research A 537 (2005) 394.

## BIOGRAPHICAL SKETCH

Jihun Choi was born in Chungcheong-do, South Korea in 1977. His family moved to Seoul at an early age where he grew up and was educated. His access to the laboratory environment began at Chungdong high school when he was a chief of the Chemistry Club. He entered the Department of Material Science and Engineering at Seoul National University in 1997 and obtained his bachelor's degree in 2002. He continued his study and obtained his Master of Science degree in 2004. His research topic for the M.S. was "Enhanced electrical properties of HfAlO high-k dielectric thin films for a gate oxide of Si MOSFET devices". After graduation with the M.S., he was hired by LG Electronics Institute of Technology (R&D campus in Seoul) as a research engineer. His research field at LG Electronics was the development of flexible displays with organic transistors. In 2007, he was admitted to the Department of Materials Science and Engineering at the University of Florida to pursue his Ph.D. degree with a specialty in electronic materials. His research interests at Dr. Holloway's group were synthesis and characterization of highly efficient luminescent nanoparticles for an application of scintillator radiation detectors. He received his Ph.D. degree in August of 2011 in Materials Science and Engineering.